12-2017

Engineering Novel 3D Tumor-Stroma Models to Bridge the Gap Between Preclinical Drug Development and Human Clinical Outcomes

Theodore J. Puls
Purdue University

ENGINEERING NOVEL 3D TUMOR-STROMA MODELS TO BRIDGE THE GAP BETWEEN PRECLINICAL DRUG DEVELOPMENT AND HUMAN CLINICAL OUTCOMES
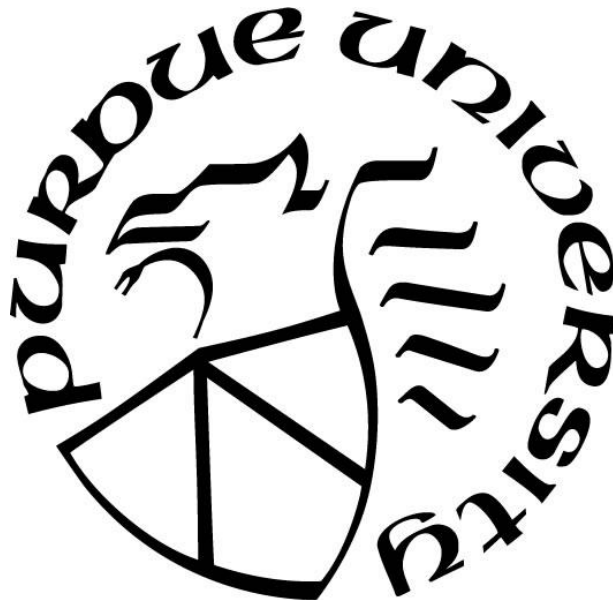
by

Theodore J. Puls

A Dissertation

Submitted to the Faculty of Purdue University

In Partial Fulfillment of the Requirements for the degree of

Doctor of Philosophy

Weldon School of Biomedical Engineering

West Lafayette, Indiana

December 2017

THE PURDUE UNIVERSITY GRADUATE SCHOOL
STATEMENT OF COMMITTEE APPROVAL

Dr. Sherry Voytik-Harbin, Chair

Weldon School of Biomedical Engineering, Purdue University

Dr. Cagri Savran

School of Mechanical Engineering, Purdue University

Dr. Pavlos Vlachos

School of Mechanical Engineering, Purdue University

Dr. Mervin Yoder

Herman B. Wells Center for Pediatric Research, Indiana University School of
Medicine

Approved by:

Dr. George R. Wodicka

Head of the Graduate Program

Dedicated to my Grandpa, Gerald Puls
who was and is one of my heroes
I would not be who I am or where I am today
without his support and inspiration

ACKNOWLEDGMENTS

I would first like to thank my thesis advisor, Sherry Harbin. Thank you for being an incredible mentor, teacher and supporter over these last four years. Thank you for always encouraging me to ask questions, to critically analyze my own work, and to think about the big picture. Thank you for always striving to make time for your students and care for us as individuals in the midst of everything else that you have pulling at your time and attention. I could not have gotten to this point without your mentorship and guidance—Thank you!

To my committee, Drs. Cagri Savran, Pavlos Vlachos, and Merv Yoder, thank you for your support, feedback and input throughout this process. To Dr. Melissa Fishel, thank you for graciously providing your support, both in terms of research supplies and input on my project. Catherine, thank you for all of the input, feedback and editing assistance you have provided over the last few years; thank you as well for providing some industry perspective to my thesis work and for testing several of my design iterations. Asem, thank you for all your help with the 3D printer and the rapid prototyping of my designs. To Lan and Lilly at the Chemical Genomics Facility, thank you for all your assistance with the Opera Phenix. To all the members of the Harbin lab, past and present, thank you for your support, encouragement and help, as well as for being an awesome group of people to work with on a daily basis; graduate school has been an amazing experience because of you guys. Specifically, thank you to Xiaohong and Mahera for all the hard work you guys have put in helping me to achieve my research goals. Additionally, I would like to thank Tammy Siemers and Sandy May for all of the behind the scenes work that you both do and for all the support, professional advice, and administrative help that you provide. I would also like to thank the BME family here at Purdue; everyone from the business office to the custodial staff make the Weldon School truly feel like family—for that I thank you.

Finally, I would like to thank all of my family and friends who have supported me along the way. To my parents, thank you for your support, encouragement and love that have allowed to me get to where I am today. Grandma, thank you as well for your encouragement and support; Kristen and I cannot thank you enough for all of your financial support in helping us both get through grad school. And last but far from least, to my wonderful wife, Kristen. Thank you for being my best friend and #1 supporter, as well as an ever-present listening ear and encourager. I am thankful beyond words to have walked through this season with you by my side.

TABLE OF CONTENTS

LIST OF TABLES

LIST OF FIGURES

ABSTRACT

Author: Puls, Theodore J. PhD
Institution: Purdue University
Degree Received: December 2017
Title: Engineering Novel 3D Tumor-stroma Models to Bridge the Gap Between Preclinical Drug
      Development and Human Clinical Outcomes
Major Professor: Sherry Voytik-Harbin

While much progress has been made in the war on cancer, shortcomings in the drug development process have kept anti-cancer clinical trial success rates low. One of the many factors implicated in this is the lack of pathophysiologically relevant and predictive preclinical models. Specifically, traditional preclinical tumor models do not capture tumor microenvironment complexity and heterogeneity, while advanced three-dimensional (3D) models suffer from poor reproducibility, lack of relevant and standardized extracellular matrix (ECM), and inability to interface with automated, high-throughput systems. Because of this, it has been suggested that developing novel phenotypic tumor models which balance the need for complexity and relevance with the ability to scale-up and translate, may help reduce the high attrition rates of clinical trials. Toward this end, this work describes the development and validation of a novel preclinical tumor model striving to achieve this balance. Model development was specifically focused on metastasis, as it remains the main cause of cancer deaths and has few good preclinical models. Since one major shortcoming of 3D in-vitro models is a lack of standardized, relevant ECM, initial work focused on defining the role of ECM composition and biophysical properties in guiding invasive phenotypes. Using a customizable and standardized oligomeric type I collagen, we demonstrated that 3D collagen fibril architecture and model geometry were key determinants of phenotypic trends and important design considerations for future model development. This work was followed by the design and validation of a custom fabrication platform to enable the rapid, reproducible embedment of tunable tumor-tissue spheres within a customizable 3D ECM. It was validated that this model can distinguish various metastatic phenotypes, is compatible with low-passage, patient-derived cells, and is able to interface with automated imaging systems. Overall, this work represents the first steps of design, verification, and validation of a novel 3D metastasis model which can serve as a relevant and predictive tool for high-throughput, high-content preclinical drug development.

1. INTRODUCTION

1.1 Motivation

While much progress has been made in the war on cancer since President Nixon "declared war" in 1971 by signing the National Cancer Act, victory in this war still remains elusive. In 2016, in the US alone, nearly 600,000 people died from cancer and over 1.5 million people were newly diagnosed with some form of the disease [1]. In addition to the immeasurable emotional toll this takes, caring for cancer patients also costs more than $120 billion a year [2], and the research and development costs of developing a single anticancer drug are estimated to be over $1 billion [3]. While these numbers are quite staggering, a more astonishing figure, that is less well known, is that the success rate of anticancer drugs going from a phase I trial to full FDA approval has been estimated to be 13.4% [4]. In other words, nearly 90% of drugs that show promise in preclinical testing fail when they are tested in humans. Additionally, 70% of drugs fail during phase II trials, which is the first time the efficacy in humans is truly examined [5]. Again, although some progress has been made in treating certain types of cancer and there have been several breakthrough therapies, it is clear that there is still a vast amount of work that needs to be done to make progress in the war on cancer.

As the above statistics suggest, one specific area that needs attention is the inefficient drug development process. Clearly, a 90% failure rate in clinical trials suggests a lack of predictive power in the preclinical phases of anticancer drug development. While this is a multifaceted problem, two of the core issues lie in pharmaceutical companies' drug development strategy and in the preclinical models used to screen potential drugs [6–8]. Thus, it has been suggested that shifting from a molecular target-based approach to a phenotypic screening approach, as well as developing better preclinical models are two ways in which we can potentially improve the abysmal success rate of anti-cancer drug development [9,10]. This perspective serves as the primary motivation for the work of this thesis and is described in more detail in the following sections.

1.2   Drug Development Strategies and Preclinical Models

It is becoming apparent that traditional drug development strategies are not very efficient or successful, and thus are in need of improvement [6,9]. Pharmaceutical companies, in general, rely on two main drug development strategies, specifically molecular target-based screening and phenotypic screening [9]. Molecular target-based screening, which has been industry standard for nearly 30 years, involves an identified molecular target (e.g., signaling protein) and associated biochemical screens focused on protein-protein interactions or enzyme activity. This process is extremely time and resource intensive because, by definition, one must know the mechanism of action of both the disease-related molecular target and the candidate drugs at the forefront of development. Phenotypic screening, on the other hand, begins with developing a disease model and associated assays focused on specific disease characteristics. One advantage of this approach is that phenotypic models are more physiologically relevant than those used early in target-based screening since they are cell- or tissue-based rather than protein- or enzyme-based. Further, this method is attractive because it does not require complete mechanistic understanding at the onset of development and is conducive to drug repurposing screens [9]. Additionally, between 1999 and 2008, the majority of newly approved drugs were developed using phenotypic screening despite molecular-target based screening being far more widely used in industry [7]. For these reasons, it has been suggested that increased use of phenotypic screening may help reduce the high attrition rate of clinical trials [7,9,10].

Another main shortcoming of anticancer drug development lies in the preclinical models used, which primarily consist of high-throughput two-dimensional (2D) cell culture and subcutaneous xenograft mice [11]. 2D cell culture does not replicate critical features of the *in-vivo* tumor microenvironment, including extracellular matrix (ECM) interactions, tumor heterogeneity, and stromal cell populations, and thus are not predictive of human tumor drug sensitivity [12,13]. Preclinical animal models are used in an attempt to reduce the high false positive rate of 2D models, however, it is questionable how much is really gained in terms of predictive power from the most common *in-vivo* models—immunodeficient subcutaneous xenograft mice. Expense, inefficiency, lack of relevant stroma, and species specific pathways are a few shortcomings of these traditional murine models [14]. Further, 2D culture and xenograft mice are oversimplified models of a very complex disease since they do not include relevant or reproducible stromal interactions and are unable to measure some phenotypic outcomes [9].

Since these traditional models do not accurately recreate important features of the tumor microenvironment, the field of "tumor engineering" has arisen as researchers attempt to fill this gap by developing novel three-dimensional (3D) cell culture models [15]. Current 3D tumor models include tumor cells embedded within various 3D matrices, multi-cellular tumor spheroids, and microfluidic models that work to incorporate numerous components of the tumor microenvironment [12,15,16]. While these models do recapitulate certain aspects of human tumors better than their 2D counterparts, there are still many shortcomings which hinder their widespread adoption and preclinical application [17]. Reproducibility and lack of user control are two of the most commonly problems for traditional naturally derived 3D culture materials (e.g. Matrigel, monomeric type I collagen), as well as for tumor spheroids [18–21]. On the other hand, complex microfluidic systems that incorporate stromal cells, vascular networks, and dynamic perfusion are often limited in their 1) ability to provide quantifiable outcome measures relevant to drug development or 2) capacity to be used for high-throughput screening [22,23]. Finally, while it is often assumed that advanced 3D models will be more predictive than 2D cell culture this assumption is rarely validated for new developed models [22–24]. In summary, while much progress has been made in 3D culture techniques, current 3D tumor models do not provide readily translatable solutions that balances physiologic relevance needed for phenotypic assays with ease of use and reproducibility required for high throughput screening [17].

1.3   Metastasis and Pancreatic Cancer

Since phenotypic screening appears to be an attractive strategy for making progress in the war on cancer, and novel models of disease phenotypes are necessary for this strategy, the next question that arises is: What phenotype should be the focus model development? Traditional phenotypic screens usually target relatively simple phenotypes or cell behaviors such as survival (live/dead) or relative metabolic activity, but clearly these types of assays can only go so far in predicting a drug's effect on a tumor. Since metastasis, the main cause of cancer deaths, has few treatment options, it seems to be good candidate for the focus of new model development [25]. Metastasis is the process by which tumor cells invade into the surrounding tissue and spread throughout the rest of the body. While all of the mechanisms at play in metastasis are not fully elucidated, the general steps of this process include 1) epithelial to mesenchymal transition (EMT) and invasion, 2) intravasation and dissemination, and 3) extravasation and colonization

[26]. Because the metastatic process is not completely understood, molecular-target based strategies, such as those targeting invasion and ECM degradation have been largely disappointing [27,28]. Finally, there are few preclinical models that accurately recreate metastatic phenotypes and can be used in high-throughput drug screens [25,29]. To this end, the goal of this work is to develop a 3D *in-vitro* metastasis model which is focused on recreating the initial steps of metastasis, EMT and invasion, while maintaining the ability to translate to high-throughput systems.

While the ultimate goal is to develop a model which can be customized and standardized for many cancer types, for the sake of initial model development pancreatic cancer was specifically chosen for this work. Pancreatic cancer, of which pancreatic ductal adenocarcinoma (PDAC) is the most common type, is only the 12th most common cancer in the US, but it is the 3rd leading cause of cancer death with a 5-year survival rate of just 8.2% [30]. The reason for this high mortality rate, is due to its late-stage diagnosis, difficulty of surgical intervention, and high rates of drug resistance and metastasis [31]. The latter of these problems is thought to be largely mediated by intense desmoplasia—another hallmark of pancreatic cancer. Desmoplasia is characterized by over-active cancer-associated fibroblasts (CAFs) and increased deposition of ECM components, especially type I collagen [32–34]. These features—the high rate of metastasis and desmoplasia—will serve as the focal point for model development in this work.

1.4   Defining User Needs: The Ideal Preclinical Tumor Model

A recent perspective article from pharma-industry researchers provided a helpful "rule of 3" to aid in the development of predictive phenotypic models [10]. These authors suggest that one must consider (1) the relevance of the model to the human disease of interest, (2) the relevance of stimuli that yield the desired phenotype, and (3) the proximity of assay readouts to clinical endpoints or outcomes. With regard to the first criteria, in-vitro models of solid tumors must consider factors such as the source of tumor cells, inclusion of stromal cell populations, ECM composition and biophysical properties, and culture format (geometry) [22,23,35]. For PDAC specifically, since desmoplasia is such a prominent feature of this disease, including a relevant type I collagen matrix and CAFs would be logical design criteria. Additionally, the stimuli which recreates the invasive phenotype in these models should occur as naturally as possible rather than being artificially induced, such as by genetic manipulation. Finally, the

readouts of ideal metastasis models will be able to measure outcomes such as invasiveness, metabolic activity and proliferation which would correlate to clinical outcomes of metastatic spread, tumor dormancy, and tumor growth. Additional criteria for designing models which can readily translate to the pharmaceutical industry include low-cost, rapid, reproducible, and simple experimental set up, ability to interface with automated equipment (e.g. automated imaging platforms, liquid handling robots), and validation of predictive power [22,23,36]. Taken together, this can be summarized as a need to find a "balance between complexity and physiologic relevance of culture method with its ease of use and potential for high throughput analyses [23]."

1.5   Note About Content and Organization of Thesis

Since this thesis is focused on model design and development, it has been framed with regard to the medical device development process. The first part of this process is clearly defining user needs and design requirements. The second stage of development is establishing a set of design inputs followed by iterative design and testing to verify that the design outputs match the design inputs. Finally, the capstone of the development process is validating that user's needs are met by the final design.. The above introductory material serves to define the problem and needs that this thesis is addressing; much of the content here was drawn from my Qualifying Literature Assessment (QLA) and Preliminary Exam document. Chapter 2 represents a manuscript that is accepted for publication in PlosOne. This chapter details efforts to 1) define how ECM composition and biophysical properties modulate EMT phenotype and 2) establish the unique type I collagen formulation developed in the Harbin lab as a powerful tool for tumor model development. Another key takeaway from Chapter 2 is that the collagen fibril architecture and 3D model geometry are critical regulators of tumor invasive phenotypes and serve as important design parameters for *in-vitro* tumor models. Chapter 3 represents a second manuscript planned for submission that targets development, verification and progressive validation of a high-throughput, high-content phenotypic model of PDAC metastasis. This chapter documents that this model meets important user needs, including 1) rapid, reproducible experimental set up, 2) recapitulating various invasive phenotypes, and 3) the ability to interface with automated imaging equipment. Finally, Chapter 4 outlines proposed next steps of model validation, showcases some preliminary data for this validation work, and discusses overall conclusions and perspectives from this thesis.

2. 3D COLLAGEN FIBRILLAR MICROSTRUCTURE GUIDES PANCREATIC CANCER CELL PHENOTYPE AND SERVES AS A CRITICAL DESIGN PARAMETER FOR PHENOTYPIC MODELS OF EMT

2.1 Introduction

Pancreatic ductal adenocarcinoma (PDAC) is one of the deadliest cancers with an estimated 5-year survival rate of around 5% [37]. PDAC is characterized by an intense stromal reaction, known as desmoplasia, where overactive cancer associated fibroblasts deposit excessive extracellular matrix (ECM), the bulk of which is fibrillar type I collagen [32,38]. It is widely thought that this stromal remodeling and dysregulation of cell-ECM homeostasis serves to promote cancer progression, including metastasis and drug resistance [38,39]. However, recent evidence suggests that desmoplasia may paradoxically play an important protective role, where resulting changes in ECM composition and architecture restrict rather than promote tumor growth and invasion [40]. Clearly, tumor-stromal ECM interactions play a critical role in PDAC pathophysiology; however, advanced *in-vitro* and *in-vivo* models are needed to achieve a more complete mechanistic understanding [40–42]. This knowledge gap, which exists for not only PDAC, but most solid tumors, precludes development of novel targeted therapies as well as identification of better predictors of patient therapeutic response. Since patients generally die from metastatic disease and PDAC has such a high metastasis rate, better understanding of how stromal ECM guides tumor phenotype and behavior is paramount to improving clinical outcomes [43–45].

ECM associated with PDAC, as well as normal tissues, is represented by two distinct types, namely basement membrane (BM) and interstitial matrix (IM). BM, composed primarily of laminin, non-fibrillar type IV collagen, and heparan sulfate proteoglycan, forms a thin sheet-like structure which supports and polarizes epithelial cell layers, separating them from the underlying interstitial tissue compartment. In contrast, the predominant component of IM is fibrillar type I collagen, within which individual mesenchymal cells (e.g., fibroblasts) reside. It is noteworthy that a hallmark of tumor metastasis is epithelial to mesenchymal transition (EMT), where epithelial cancer cells lose polarity and cell-cell associations while gaining a more mesenchymal and invasive phenotype. Figure 2-1 highlights salient features of tumor EMT,
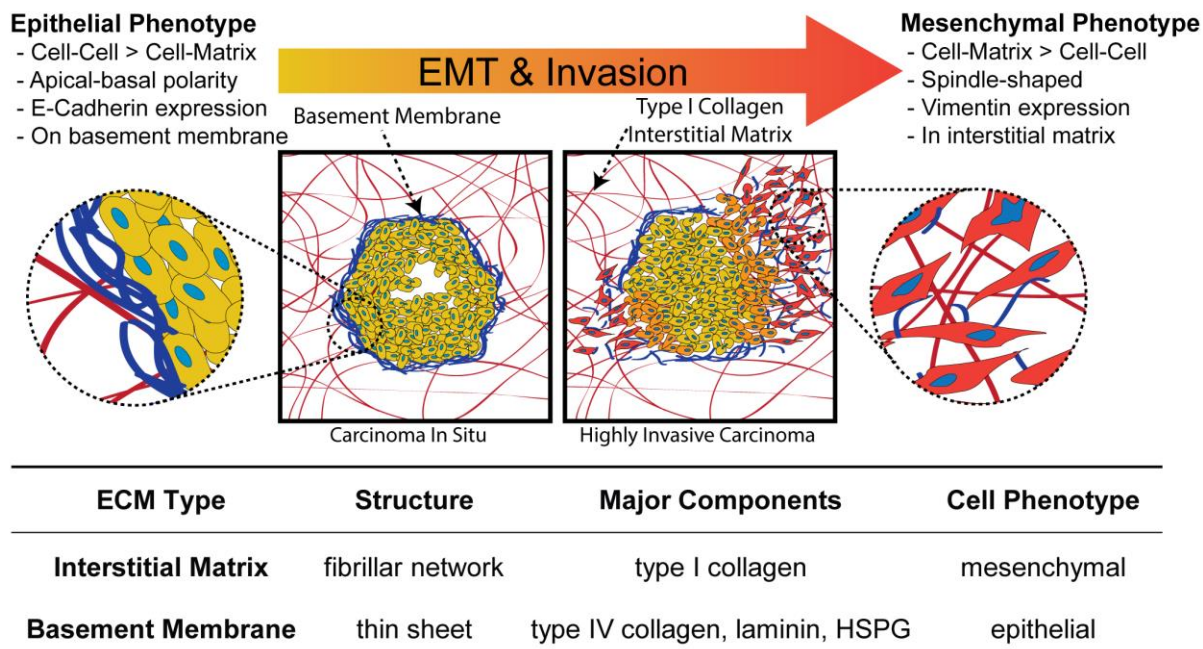
Figure 2-1 Overview of EMT and associated tumor stromal ECM interactions.
Schematic shows key characteristics and progression of EMT, as epithelial cancer cells lose contact with basement membrane and interface with the surrounding interstitial matrix which is composed primarily of fibrillar type I collagen. Association with the stromal interstitial matrix correlates with transition from an epithelial to a mesenchymal phenotype. HSPG = heparan sulfate proteoglycan.

drawing attention to the altered stromal ECM context encountered by tumor cells as they increasingly interact with surrounding IM [44]. This marked difference in ECM context is often overlooked in conventional EMT schematics where IM is often excluded and intracellular events are emphasized [44,46].

Although it is evident that EMT is marked by dynamic tumor cell-ECM interactions, where cells may engage both BM and IM components, many experimental *in-vitro* models lack rigorous definition of relevant ECM molecular and physical properties [47,48]. In fact, tumor EMT research has traditionally focused on soluble factor (e.g., TGF-β1) induction and intercellular signaling cascades [49,50]. However, since recent work suggest that matrix composition and physical properties (e.g. microstructure and viscoelastic properties) are involved in driving EMT, ideal tumor models should recreate the 3D fibrillar IM microstructure and geometry of cell-cell and cell-matrix associations to support physiologically relevant cell phenotypes, as well as enable mechanistic study through matrix tunability [12,13,38]. Unfortunately, many models fail to replicate these critical features of 3D tumor-ECM

interactions and give rise to contradictory results. For example, breast cancer cells cultured on-top of Matrigel- or type I collagen-coated polyacrylamide (PA) gels showed that increased PA concentration (stiffness) enhanced EMT [51,52], while breast cancer and glioblastoma spheroids embedded within 3D fibrillar type I collagen matrices showed decreased mesenchymal behavior and invasiveness with increased collagen concentration (stiffness) [53–55]. These examples showcase how different geometries of cell-matrix interactions and ECM microstructures can yield conflicting results. Clearly, the ability to recreate ECM architecture and physical properties experienced by cancer cells *in vivo* will contribute to a more complete understanding of EMT and invasion.

Over the last several years, our laboratory has worked to develop new tools and methods for mechanistic study of fibrillar type I collagen self-assembly and the impact of resultant matrix physical properties on cell phenotype, function, and tissue morphogenesis. As part of this effort, we identified and standardized (ASTM F3089-14) a new soluble collagen subdomain (Oligomer) that retains natural, mature intermolecular crosslinks as well as the uncommon capacity for suprafibrillar self-assembly [18,56]. Oligomer displays rapid self-assembly (polymerization) *in vitro* and *in vivo*, forming highly-interconnected, D-banded collagen-fibril networks, which are similar to those found in tissues *in vivo*. This collagen formulation supports systematic modulation of the physical and biological properties of 3D IM microenvironments beyond what can be achieved with conventional collagen monomer formulations [18]. The tunable and robust matrices formed with Oligomer have proven useful in a variety of *in-vitro* applications including mesenchymal stem cell differentiation, vascular network formation, glioblastoma migration, and tissue engineering [55,57–59]. Type I oligomeric collagen (Oligomer) offers a promising alternative to materials traditionally used to mimic the IM in 3D cancer models.

The goal of the present work was to develop and apply an *in-vitro* 3D tumor-ECM model relevant to PDAC to further define the importance of ECM composition and physical properties in guiding EMT. Three well-characterized PDAC lines representing points along the EMT phenotypic spectrum were embedded within 3D self-assembled ECM microenvironments of defined composition and physical properties and changes in their phenotype evaluated. For this work, Oligomer was used to recreate the IM, and Matrigel, a reconstituted BM isolated from Engelbreth-Holm-Swarm (EHS) mouse sarcomas (a tumor rich in basement membrane) [19] was used to mimic the BM. Matrigel is routinely used to approximate a BM-like environment since

it provides a complex mixture of macromolecules including laminin, type IV collagen, and enactin. However, limitations associated with Matrigel include: 1) poorly defined molecular composition, 2) lot-to-lot variability (protein concentration and molecular composition), and 3) inability to recapitulate the specific nature of the biochemical and biophysical environment associated with all tumors (lacks type I collagen and *in-vivo* cross-linking) [19,60]. Overall, our results revealed a spectrum of matrix-driven phenotypes that were dependent on ECM composition, fibril architecture, and initial cell phenotype. In general, non-fibrillar BM (Matrigel) promoted epithelial behaviors such as clustered cell growth and E-cadherin expression. In low density Oligomer, the exposure to fibrillar IM promoted EMT of a subpopulation of epithelial BxPC-3 cells, while mesenchymal MiaPaca-2 cells more uniformly displayed mesenchymal characteristics. Interestingly, for all PDAC lines, increasing IM fibril density, which represents increasing desmoplasia, resulted in confined clustered growth due to the increased spatial constraints and matrix stiffness. Comparison of ours results to those from other *in-vitro* models highlight the importance of ECM composition, microstructure, and mechanical properties in 3D *in-vitro* cancer models and establish Oligomer as a powerful tool in cancer research for mechanistic study of tumor-ECM interactions.

2.2   Materials and Methods

2.2.1   Cell culture

BxPC-3, Panc-1, and MiaPaCa-2 cell lines were all obtained from American Type Culture Collection (ATCC, Manassas, VA) and maintained per manufacturer guidelines. BxPC-3 cells were grown in RPMI-1640 (Life Technologies, Grand Island, NY) and Panc-1 and MiaPaCa-2 cells were grown in high glucose DMEM (Hyclone, Logan, UT), all supplemented with 10% heat inactivated fetal bovine serum (HI FBS; Life Technologies), 100 U/mL penicillin, and 100 μg/mL streptomycin (Sigma Aldrich, St. Louis, MO). Growth medium of MiaPaCa-2 cells was additionally supplemented with 2.5% horse serum (Sigma Aldrich). Cells were maintained in a humidified environment of 5% CO2 in air at 37°C, passaged at 70-80% confluency, and used in experiments at passage numbers between 6 and 14.

2.2.2   Creating in-vitro 3D tumor-ECM models

Type I oligomeric collagen was extracted from the dermis of market weight pigs (Beutler Meat Processing, Lafayette, IN) using acid solubilization as previously described [23]. Pig hides for this extraction process were obtained from a commercial meat-processing source according to Purdue University Animal Care and Use Committee (PACUC) guidelines, though specific approval was not needed. Extracted collagen was lyophilized for storage, dissolved in 0.01 N hydrochloric acid (HCl) for use, and standardized according to ASTM International Standard F3089-14 [30]. Briefly, Oligomer formulations were standardized based on molecular composition and polymerization capacity which is defined by the relationship between shear storage modulus (G', Pa) of the polymerized matrix as a function of Oligomer concentration. Growth Factor Reduced Matrigel (Corning Life Sciences, Tewksbury, MA) was stored at -20°C and thawed at 4°C or on ice before use. Since Matrigel is known to have high batch-to-batch variability [28,31], all drug dosing experiments were performed with the same lot.

In-vitro 3D tumor-ECM models were created by encapsulating tumor cells within various reconstituted matrix compositions at $2x10^5$ cells/mL. Matrigel was used undiluted, while Oligomer was diluted with 0.01 N HCl to desired concentrations and neutralized (pH=7.4) with 10X phosphate-buffered saline (PBS) and 0.1 N sodium hydroxide as previously described [25]. To create matrices with different Oligomer:Matrigel ratios, neutralized Oligomer solution (0.9 mg/mL) and Matrigel solutions were admixed at the following ratios—100:0, 75:25, 50:50, 25:75, 0:100 (volume:volume). To determine the effect of IM physical properties on EMT, Oligomer-only matrices were prepared at concentrations of 0.9, 1.5, 2.1 mg/mL which corresponded to shear storage modulus (matrix stiffness) values of approximately 100-, 500- and 1000 Pa. We have previously established that a positive correlation exists between Oligomer concentration, fibril density, and matrix stiffness [23,25,32]. 3D constructs were created by aliquoting matrix-cell suspensions (100 μL, $2x10^5$ cells/mL) into a 96 well plate followed by incubation at 37°C for 20-30 minutes to induce matrix polymerization or self-assembly. Immediately following self-assembly, the appropriate cell culture medium was added and constructs were cultured for four days with medium changes every other day.

2.2.3   Viscoelastic testing

Viscoelastic properties of matrices were determined using oscillatory shear mode on an AR2000 rheometer (TA Instruments, New Castle, DE) as previously described [23]. Samples were polymerized on the rheometer stage for 30 min followed by a shear-strain sweep from 0.1% to 4% strain at 1 Hz. The shear storage modulus (G') at 1% strain was used as a measure of matrix stiffness. Each sample was tested in triplicate (n=3).

2.2.4   Staining and imaging

Tumor-ECM constructs were fixed in 3% paraformaldehyde (Mallinckrodt, Derbyshire, UK) and permeabilized using 0.1% Triton X-100 (Sigma Aldrich). To visualize cell morphology, F-actin was stained with Alexa Fluor 488 phalloidin (Life Technologies). For immunostaining, constructs were blocked with 1% bovine serum albumin (Jackson ImmunoResearch, West Grove, PA), followed by overnight incubation at 4°C with goat anti-rabbit primary antibodies for vimentin and E-cadherin (D21H3 and 24E10, Cell Signaling Technologies, Danvers, MA). After rinsing with 1X PBS, constructs were incubated overnight at 4°C with anti-rabbit conjugated Alexa Fluor 488 secondary antibody (A12379, Life Technologies) followed by nuclear counterstaining with Draq5 (Life Technologies).

Images were collected using laser scanning confocal microscopy on an Olympus IX81 inverted microscope with an Olympus Fluoview FV1000 system (Olympus, Tokyo, Japan). Image stacks of 150-200 µm thickness with a 5 µm step size were obtained using a 20X air or 60X water objective, and z-projections were created using Imaris software (Bitplane, Concord, MA). Confocal reflection microscopy was used to visualize the collagen-fibril microstructure [33].

2.2.5   Western blotting

Western blots were used to determine EMT protein expression on a population level for BxPC-3 and MiaPaca-2 in 2D and within constructs of varied Oligomer stiffness and Oligomer:Matrigel ratios. Cell lysates from 2D culture were obtained directly from cell culture flasks at 70-80% confluency using chilled 1X RIPA buffer (Millipore, Bedford, Massachusetts) containing 0.2% halt phosphatase and protease inhibitor cocktail (Thermo Fisher Scientific, Waltham, MA), and 2% phenylmethanesulfonyl fluoride solution (Sigma-Aldrich; 2%). Lysates

from 3D culture were obtained by snap freezing constructs after four days of culture, grinding them into a powder, and dissolving in lysis buffer. All samples were kept on ice with periodic vortexing for one hour for 2D samples and three hours for 3D samples. Total protein concentration for all samples was determined using a BCA protein analysis kit (Pierce, Rockford, Illinois). Samples containing 30 µg of protein were loaded onto a 4-20% Tris-HCl pre-cast gels (Bio-Rad, Hercules, CA) and transferred onto Trans-Blot Turbo Midi Nitrocellulose membranes (Bio-Rad). After blocking in SEA BLOCK Blocking Buffer (Thermo Fisher Scientific) overnight at 4° C, the membranes were incubated with mouse antibodies against E-cadherin (Cell Signaling Technology, 1:1000), fibronectin (BD Biosciences, San Jose, CA; 1:1000), and vimentin (BD Biosciences; 1:1000) overnight at 4° C. Mouse antibody against glyceraldehyde 3-phosphate dehydrogenase (GAPDH; Meridian Life Science, Memphis, TN; 1:1000) was used as a loading control. Membranes were then washed in 1X PBS with 0.05% Tween-20 (Sigma-Aldrich) and incubated for two hours at room temperature with horseradish-peroxidase–conjugated IRDye 800CW anti-mouse secondary antibody (LI-COR Biosciences, Lincoln, NE; 1:10000). After multiple washes with the PBS/Tween solution, bands were visualized using Odyssey CLx Infrared Imaging System (LI-COR).

2.2.6 Determining gemcitabine sensitivity

PDAC cell sensitivity to gemcitabine (Santa Cruz Biotechnology, Dallas, TX) was determined by dosing with a 10-point drug dilution (1:5 dilution starting at 200 µM) and calculating IC50 values from data obtained with Alamar Blue metabolic indicator (Invitrogen, Frederick, MD). Cells were seeded in 96-well plates either on 2D tissue culture plastic at $4x10^3$ cells/well or within different 3D matrix formulations at $2x10^5$ cells/mL (100 µL or $2x10^4$ cells/well). After 24 hours, culture medium was replaced with medium containing gemcitabine dilutions, 20 µM staurosporine (positive kill control; Santa Cruz Biotechnology), or 1% DMSO (negative control; Sigma Aldrich). Treatments were replenished after 48 hours. Each treatment was performed in triplicate, and all experiments were repeated at least 3 times (N≥ 3; n=3).

After 72 hours of treatment, fresh medium containing 10% Alamar Blue solution and 1% FBS was added to each well, and well-plates were incubated for an additional 8 hours. Fluorescence intensity of medium was measured spectrofluorometrically using 530 nm/590 nm excitation/emission on a SpectraMax M5 Microplate Reader (Molecular Devices, Sunnyvale,

CA). Raw intensity values were normalized to the positive and negative controls with the following equation: $\% \text{ } Cell \text{ } Viablity = (I_n - I_{STS})/(I_{DMSO} - I_{STS}) \times 100\%$. I_n represents the intensity value of the *nth* dilution. I_{STS} and I_{DMSO} represent intensities recorded from positive kill control and negative control, respectively. GraphPad Prism (GraphPad Software Inc., San Diego, CA) was used to fit a four-parameter logistic curve. The automatic robust outlier detection algorithm within Prism was used to detect and exclude outliers from the final fit. Reported values represent relative IC50, defined as the halfway point between the bottom and top plateaus of each curve.

2.2.7 S-phase fraction determination

Total cell number and the fraction of cells undergoing S-phase were determined using Click-iT Edu (Life Technologies) followed by quantitative image analysis using Imaris (Bitplane). Briefly, after 3 days of culture, tumor-ECM construct medium was refreshed with medium containing 10 µM 5-ethynyl-2'-deoxyuridine (Edu) and cultured for another 24 hours. Constructs were then fixed with 3% paraformaldehyde (Mallinckrodt), permeabilized using 0.1% Triton X-100 (Sigma Aldrich), and incubated with Click-iT reaction cocktail prepared following manufacturer's instructions. Constructs were subsequently counterstained with Draq5 and z-stack images of 50 µm thickness were collected using laser scanning confocal microscopy on an Olympus IX81 inverted microscope with an Olympus Fluoview FV1000 system (Olympus) and a 20X air objective. The Imaris spot detection algorithm was used to independently detect nuclei stained with Click-iT Edu and Draq5 for quantification of the number of cells undergoing S-phase and total cell number, respectively. S-phase fraction was then calculated by dividing the number of S-phase cells by the total number of cells. Images (2 per well) from two separate experiments (N=2) performed in triplicate (n=3) for each matrix stiffness were used for final calculations and statistics.

2.2.8 Statistical analysis

Statistical analyses were performed using SAS (Statistical Analysis System; SAS Institute Inc., Cary, NC). For gemcitabine sensitivity, a two-factor ANOVA was used to compare stromal ECM microenvironment and cell type. Main effects were compared using Tukey-corrected pairwise comparisons for one factor while holding the other factor constant. A one-

factor ANOVA with Tukey-corrected pairwise comparisons was used to analyze viscoelastic testing data. S-phase fraction data was analyzed with a three-factor ANOVA which included experiment number and replicate as factors in order to test their significance and not falsely inflate the degrees of freedom in the model. In all cases, differences were considered statistically significant when $p < 0.05$.

2.3   Results

2.3.1   Established PDAC lines cultured in 2D represent phenotypes along the EMT spectrum

Throughout this work, three established PDAC lines with distinct EMT phenotypes were used (BxPC-3 – epithelial, Panc-1 – intermediate, and MiaPaCa-2 – mesenchymal) to evaluate ECM-guided EMT. Literature based characteristics of these PDAC lines are summarized in Figure 2-2A. To validate each cell line's initial phenotype, cell morphology and expression patterns of EMT marker proteins, E-cadherin and vimentin [8,34], were determined following 2D culture. Here, we defined epithelial phenotype as cells growing in tight clusters with prominent E-cadherin expression, high cell-cell interactions, and primarily cortical actin [35]. On the other hand, mesenchymal phenotype was characterized by individual cells with spindle-shaped morphology, prominent actin projections, high cell-ECM interactions, and pronounced vimentin expression [35].

Consistent with previously published work [61,62], BxPC-3 cells displayed an epithelial phenotype in 2D culture, growing as cell clusters with prominent E-cadherin expression, while MiaPaCa-2 cells were mesenchymal, displaying the typical spindle-morphology with vimentin expression (Figure 2-2B). Panc-1 cells exhibited an intermediate phenotype, growing as clusters with some actin projections and expressing vimentin but not E-cadherin (Figure 2-2B). In addition to phenotype, gemcitabine sensitivity was measured with relative IC50 values calculated from 10-point dose response curves, showing that in 2D, Panc-1 cells were the most resistant to gemcitabine, followed by BxPC-3, and then MiaPaCa-2 (Figure 2-2C). These results were consistent with previously published studies where similar experimental conditions and assay methods were employed (Appendix Table S 1).
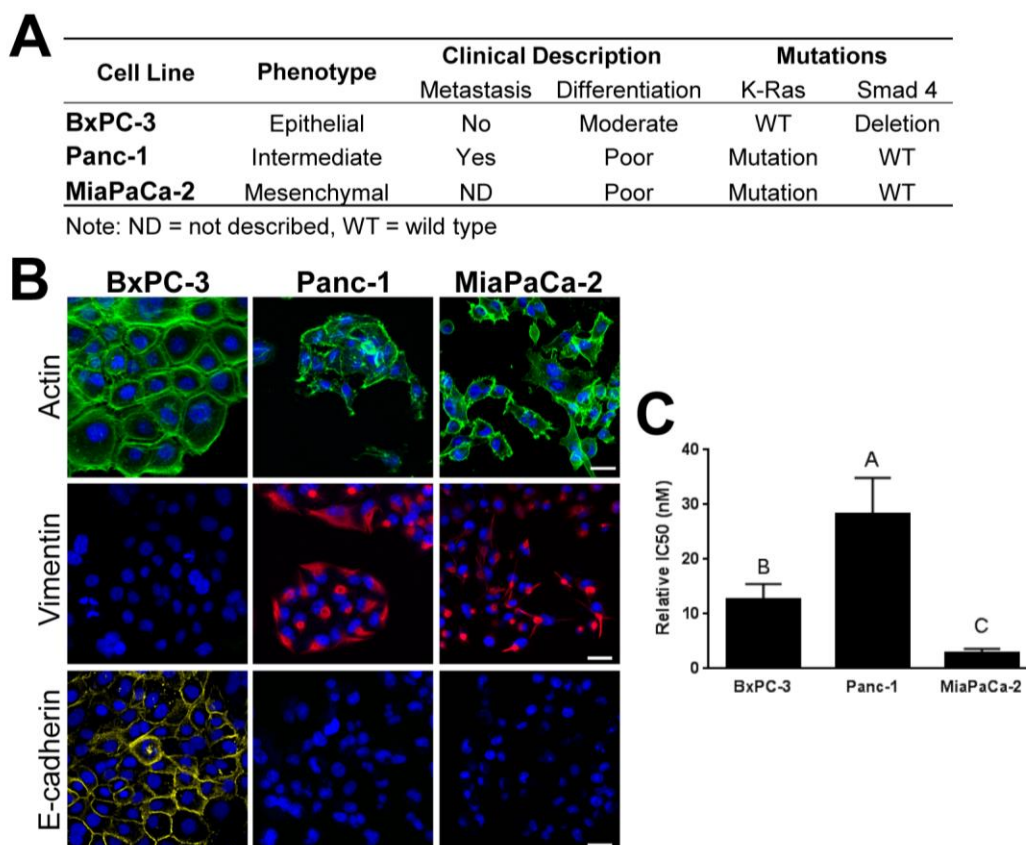
Figure 2-2 PDAC lines differ in EMT phenotype and gemcitabine resistance when cultured on 2D plastic.
(A) Table summarizing pancreatic cell line phenotype, patient derivation, and relevant mutations [122]. (B) BxPC-3, Panc-1,and MiaPaCa-2 cells were cultured on 2D plastic ($4x10^3$ cells/well) for 4 days, stained for actin (green), vimentin (red), E-cadherin (yellow), and nuclei (blue), and imaged using confocal microscopy. Images represent z-stack projections (20 µm thickness; scale bar = 30 µm). (C) Gemcitabine IC50 values (mean ± SD) were determined from 10-point dose response curves for cell lines cultured on 2D plastic. Letters indicate statistically different groups ($p < 0.05$, n=5).

2.3.2   At matched stiffness, Oligomer induces EMT and Matrigel induces MET

The effect of various ECM ligands and soluble factors on tumor cell plasticity and EMT phenotype is routinely studied for cells cultured on 2D surfaces [63–66]. However, less is known regarding how cells sense and respond to 3D IM and BM environments with defined biochemical and biophysical attributes [54,67,68]. Here, PDAC lines were cultured within 3D type I collagen-fibril matrices prepared with Oligomer and tumor BM-like microenvironments prepared with Matrigel. Since Oligomer and Matrigel represent different ECM compositions and microstructures, an Oligomer concentration was chosen to yield matrix stiffness values that matched undiluted Matrigel (G'=100 Pa), avoiding stiffness as a possible confounding variable.

As summarized in Figure 2-3, the fibrillar type I collagen matrices formed by Oligomer (100 Pa) promoted various degrees of EMT and mesenchymal behavior, while Matrigel induced more MET and epithelial behavior. More specifically, when grown within Oligomer (100 Pa), all PDAC lines showed decreased cell-cell associations and more pronounced spindle-shaped morphology with prominent actin projections. A subset of BxPC-3 cells shifted to expressing both vimentin and E-cadherin in Oligomer as detected by immunostaining, while both Panc-1 and MiaPaCa-2 cells only expressed vimentin. In contrast, all PDAC lines cultured within

Cell type	Characteristic	2D Plastic	3D Matrigel	3D Oligomer
	E-cadherin	++	++	+
BxPC-3	Vimentin	-	-	+
	Morphology	round, clustered	round, clustered	spindle, single-celled
	E-cadherin	-	+	-
Panc-1	Vimentin	++	+	++
	Morphology	round, clustered	round, clustered	spindle, single-celled
	E-cadherin	-	-	-
MiaPaCa-2	Vimentin	++	+	++
	Morphology	spindle, single-celled	round, clustered	spindle, single-celled
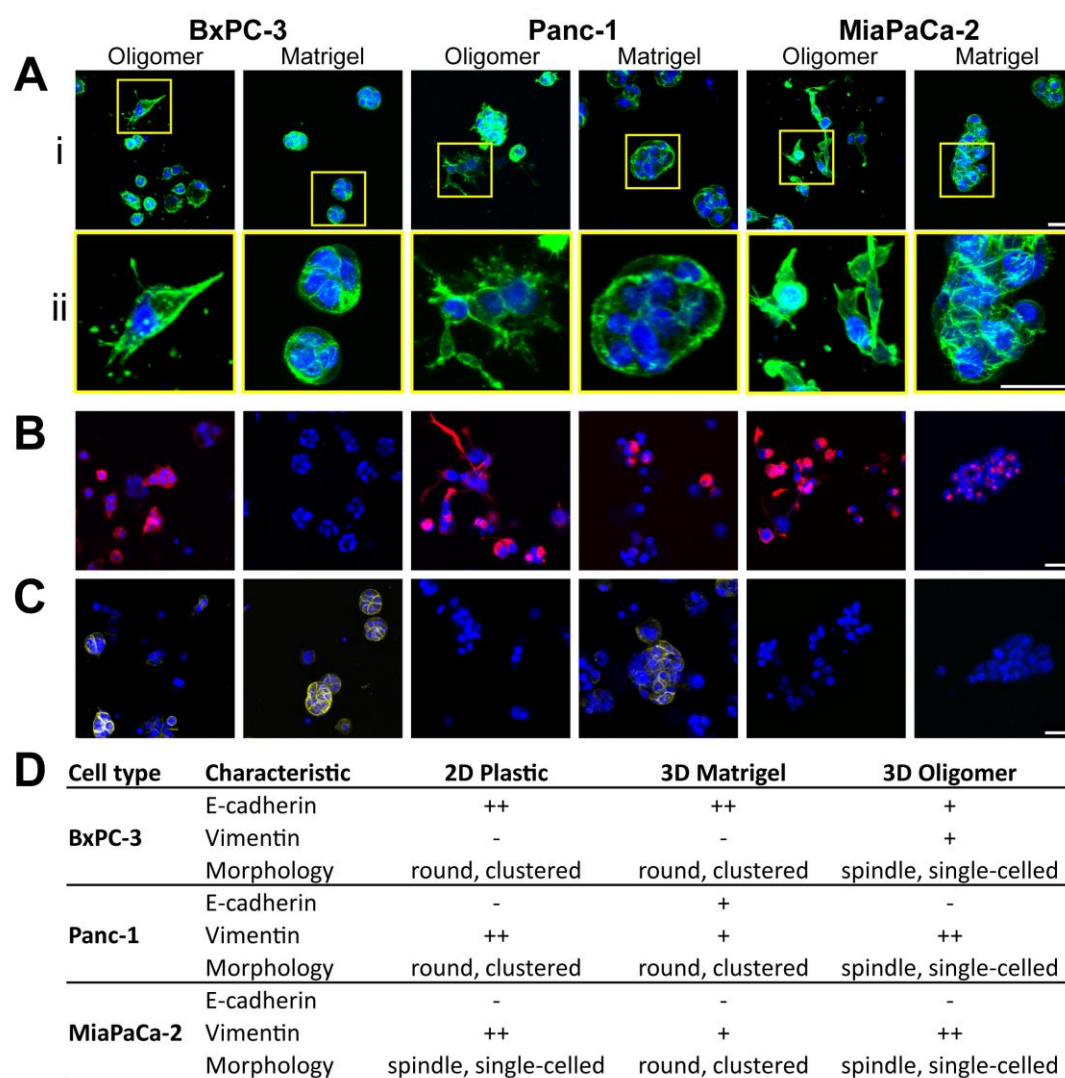
Figure 2-3 Stromal ECM drives pancreatic cancer cell morphology and phenotype.
BxPC-3, Panc-1, and MiaPaCa-2 cells were cultured (2×10^5 cells/mL) for 4 days within Oligomer (0.9 mg/mL; 100 Pa) and Matrigel (100 Pa). Constructs were stained for actin (A; green), vimentin (B; red), E-cadherin (C; yellow), and nuclei (blue) and imaged using confocal microscopy. Images represent z-stack projections (100 µm thickness; scale bar = 30 µm). Yellow boxes represent 3X digitally zoomed sections (ii) and arrowheads note prominent actin protrusions. (D) Table summarizing protein expression and morphological observations from panels A-C.

Matrigel grew as tight clusters with high nuclear to cytoplasmic ratios and cortical actin (Figure 2-3A). Additionally, within Matrigel, Panc-1 cells shifted to expressing both E-cadherin and vimentin, while BxPC-3 and MiaPaCa-2 cells expressed E-cadherin only and vimentin only, respectively (Figure 2-3B,C). Collectively, these results document that specific ECM ligands, and their associated microstructures, are critical determinants of PDAC phenotype and behavior, especially as it relates to EMT and MET.

2.3.3 Dose response analysis reveals matrix-dependent gemcitabine sensitivity of PDAC lines

In high throughput 2D drug screening, IC50 is commonly used as a measure of drug sensitivity. However, fewer studies report IC50 values for 3D culture models because adapting drug dosing protocols and analyses to 3D formats tends to be more difficult, time consuming, and resource intensive [11,69]. To demonstrate that our 3D tumor-ECM model is amenable to medium and high throughput drug screening, the relative IC50 values of gemcitabine were determined for each PDAC line within 3D Oligomer and Matrigel, prepared with matched matrix stiffness. As shown in Figure 2-4, gemcitabine sensitivity of PDAC lines was matrix dependent. When cultured within Oligomer (100 Pa), PDAC lines showed statistically similar (p>0.05) IC50 values, ranging from about 6 to 23 nM. In contrast, when cultured within Matrigel, Panc-1 cells

A Relative IC50 (mean ± SD, nM)

	BxPC-3	Panc-1	MiaPaCa-2
Oligomer	22.5 ± 9.1	13.8 ± 6.3	5.79 ± 4.66
Matrigel	18.3 ± 12.9	72.8 ± 41.3	15.4 ± 2.8

Figure 2-4 Sensitivity of PDAC lines to gemcitabine depends on 3D matrix type.
(A) Table and (B) graph summarizing gemcitabine IC50 values (mean ± SD) for PDAC lines cultured ($2x10^5$ cells/mL) for 4 days within Oligomer (0.9 mg/mL, 100 Pa) or Matrigel (100 Pa). Asterisk (*) indicates statistically different groups (p<0.05, N=3-4, n=3).

displayed a significantly (p<0.05) higher IC50 value of 72.8±41.3 nM compared to BxPC-3 and MiaPaCa-2 cells which measured 18.3±12.9 nM and 15.4±2.8 nM, respectively. Further, IC50 values for BxPC-3 and MiaPaCa-2 cells in Matrigel wer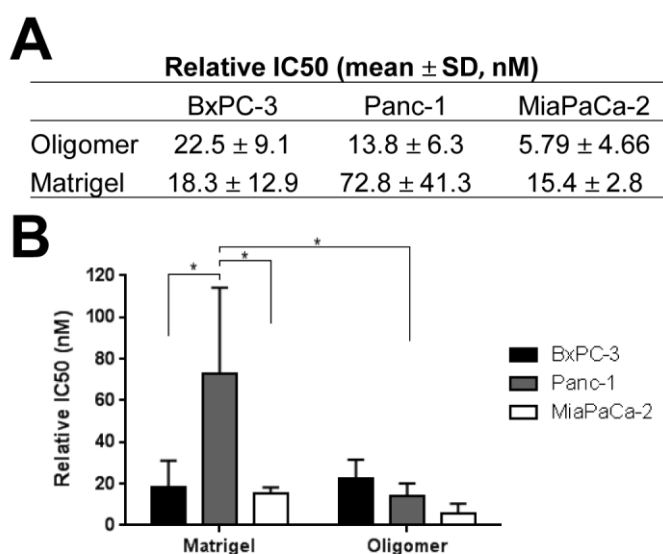e statistically similar (p>0.05) to those obtained for Oligomer (100 Pa), while Panc-1 cells' IC50 was significantly lower (p<0.05) in Oligomer compared to Matrigel. It is worth noting that Panc-1 cells showed greater resistance to gemcitabine compared to the other PDAC lines when cultured within Matrigel (Figure 2-4) and on plastic (Figure 2-2C), but not within Oligomer. Collectively, these results emphasize that the tumor microenvironment, including ECM composition and microstructure, is a critical determinant of PDAC drug sensitivity.

2.3.4   Varying stromal IM to BM ratio guides PDAC phenotype and EMT

As tumor cells become exposed to fibrillar type I collagen, whether deposited by stromal cells or encountered at the tumor-tissue interface, cells may simultaneously interact with both IM and BM components, thus engaging different integrin receptors [70,71]. To define how such dynamic cell-ECM signaling affects PDAC phenotype and EMT, PDAC cells were cultured within matrices prepared with different ratios of Oligomer and Matrigel, representing IM and BM, respectively. These experiments were conducted with only two PDAC lines, BxPC-3 and MiaPaCa-2, representing epithelial and mesenchymal phenotypes.

Matrix microstructure and stiffness were defined to determine how varying Oligomer:Matrigel (IM:BM) ratio altered matrix self-assembly and physical properties (Figure 2-5). As visualized by confocal reflectance microscopy, matrix architecture varied from the highly- branched fibrillar network for Oligomer (100:0) to no visible fibril microstructure in Matrigel (0:100), emphasizing differences in self-assembly capacity and matrix physical properties. Fibril density and length appeared to decrease with decreasing Oligomer:Matrigel ratio with 100:0 and 75:25 displaying dense branched fibril networks and 50:50 and 25:75 exhibiting fewer and shorter fibrils. Observed differences in microstructure were consistent with measured alterations in matrix mechanical properties. More specifically, matrix stiffness (G') values for 100:0 and 75:25 were statistically similar (p>0.05) while 50:50 and 25:75 were significantly softer (p< 0.05). As expected for this experiment, 0:100 (Matrigel) and 100:0 (Oligomer) stiffness values were statistically similar (p>0.05), since Oligomer concentration was chosen to match the stiffness of undiluted Matrigel.
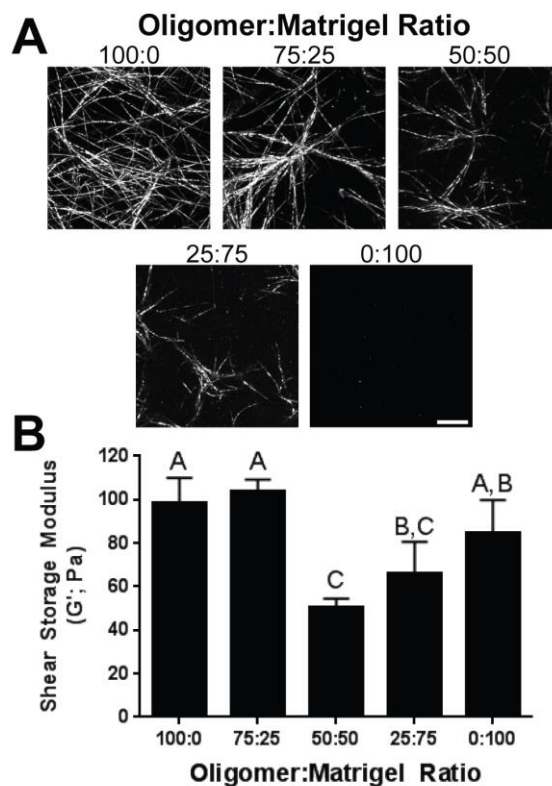
Figure 2-5 Oligomer:Matrigel ratio affects matrix microstructure and stiffness.
(A) Images represent z-stack projections (10 μm thickness; scale bar = 10 μm) from confocal reflection microscopy of matrices prepared with varying Oligomer:Matrigel ratios. (B) Matrix stiffness values are given as shear storage modulus (G'; mean ± SD). Letters indicate statistically different groups (p < 0.05, n=3).

Analysis of PDAC cell morphology and protein expression as a function of Oligomer:Matrigel ratio further supported the supposition that Oligomer induced EMT and Matrigel induced MET to an extent that was dependent upon initial PDAC cell phenotype. As the Oligomer:Matrigel ratio increased, an increased number of BxPC-3 cells transitioned from an epithelial morphology to smaller cell clusters or individual cells displaying prominent cytoplasmic projections (Figure 2-6A). In addition, these subpopulations showed an apparent increase in vimentin expression and decreased E-cadherin expression as the Oligomer:Matrigel ratio increased. Interesting these differences in maker protein expression were not observed when measured at a population level via western blots which showed no change in E-cadherin expression and no detectable vimentin expression with changing ratios (Figure 2-7). Modest fibronectin expression was observed in BxPC-3 cells cultured in 100:0, but expression decreased to undetectable levels once Matrigel was introduced into the construct.
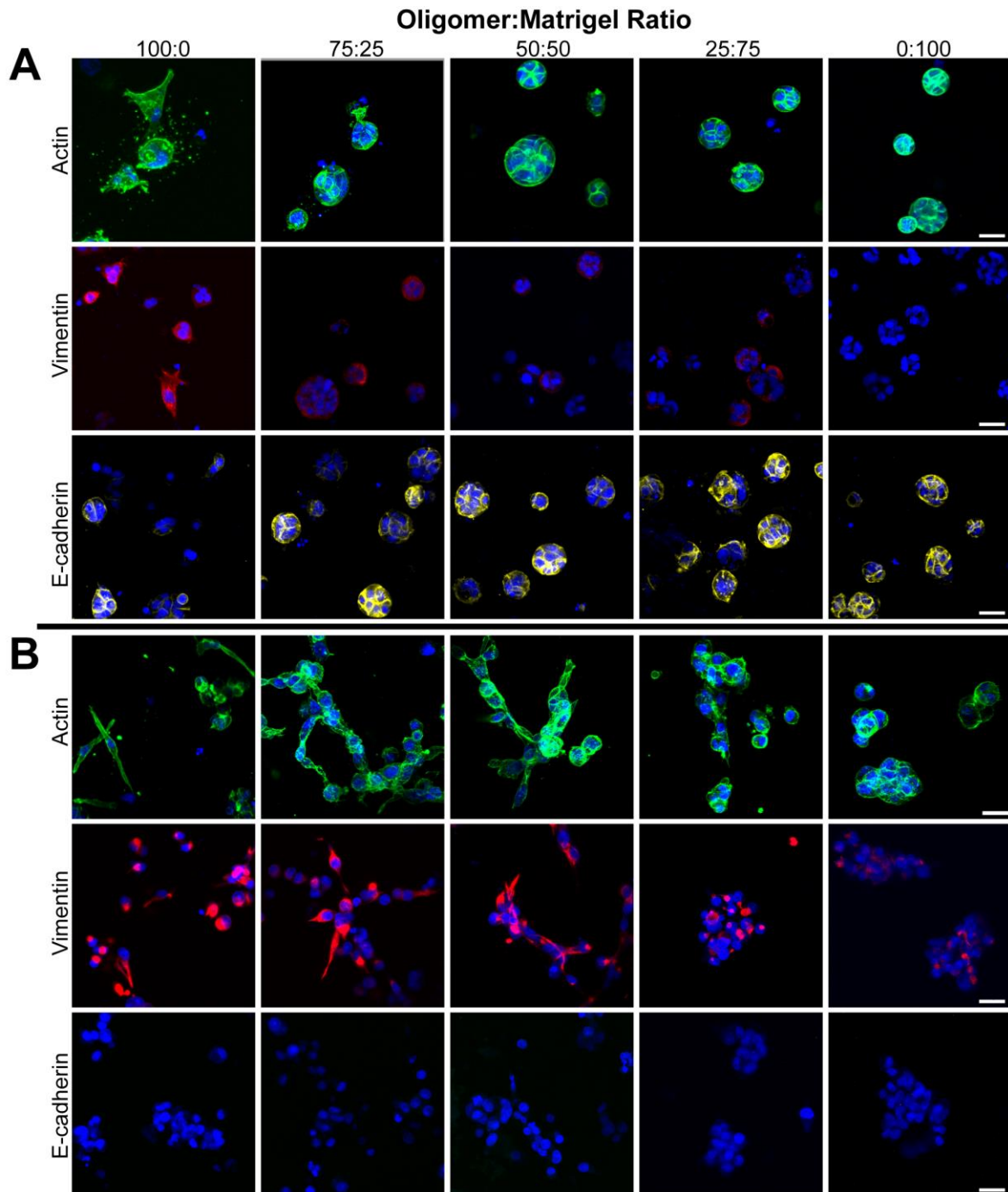
Figure 2-6 Oligomer:Matrigel ratio modulates EMT phenotype.
 (A) BxPC-3 and (B) MiaPaCa-2 cells were cultured ($2x10^5$ cells/mL) within 3D matrices prepared with various Oligomer:Matrigel ratios for 4 days. Constructs were stained for actin (green), vimentin (red), E-cadherin (yellow), and nuclei (blue) and imaged using confocal microscopy. Images represent z-stack projections (100 µm thickness; scale bar = 30 µm).
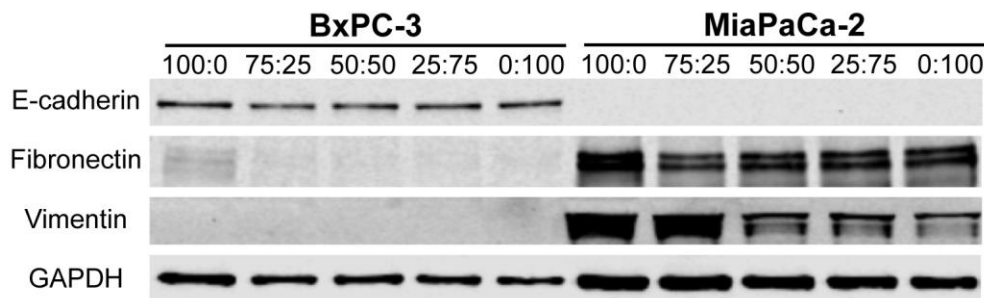
Figure 2-7 Oligomer:Matrigel ratio has phenotype-dependent effect on population-level protein expression. Western blots showing EMT protein expression for BxPC-3 and MiaPaCa-2 ($2x10^5$ cells/mL) cultured for 4 days within 3D matrices prepared at various Oligomer:Matrigel ratios.

MiaPaCa-2 cells, on the other hand, showed more drastic changes in morphology (Figure 2-6B) and population-level protein expression (Figure 2-7) with varying Oligomer:Matrigel ratio, while immunostaining revealed only modest changes in EMT protein expression patterns (Figure 2-6B). Within the lowest Oligomer:Matrigel ratios (0:100 and 25:75), MiaPaCa-2 cells were tightly packed with little to no actin projections. As Oligomer content increased, cells became progressively more singular and spindle-shaped, with cells in 75:25 aligning into networks resembling the invasive front of a tumor. Immunostained MiaPaCa-2 cells did not express detectable E-cadherin in any matrix composition. While vimentin expression was observed in all matrices, it appeared to be reduced within 0:100 and 25:75 and shifted from uniformly distributed throughout the cytoplasm to localized around cell nuclei. Analysis by western blot confirmed immunostaining results with Oligomer:Matrigel ratio showing having no effect on MiaPaCa-2 E-cadherin expression and vimentin expression decreasing with Matrigel content (Figure 2-7). A similar decreasing expression trend was observed for fibronectin with highest expression levels occurring in MiaPaCa-2 cells cultured within 100:0. Altogether, these results suggest that i) a combination of IM and BM interactions plays an important role in guiding tumor cell plasticity and EMT, and ii) ECM type and microstructure differentially regulate cell phenotype depending on the cells' initial EMT status.

2.3.5 Increasing collagen-fibril density (matrix stiffness) controls mesenchymal behavior and suggests matrix dependent correlation between S-phase fraction and drug sensitivity

Pancreatic cancer is known for significant desmoplasia, characterized by over-active stellate cells and fibroblasts which increase fibrillar type I collagen deposition [32,33]. However,

the precise role played by desmoplasia and type I collagen in tumor-stromal ECM interactions and tumor progression remains uncertain [40,72,73]. In order to better define the role of IM physical properties in regulating EMT and drug sensitivity, matrix stiffness was varied by altering the Oligomer concentration or fibril density as seen in Figure 2-8A and B. The positive
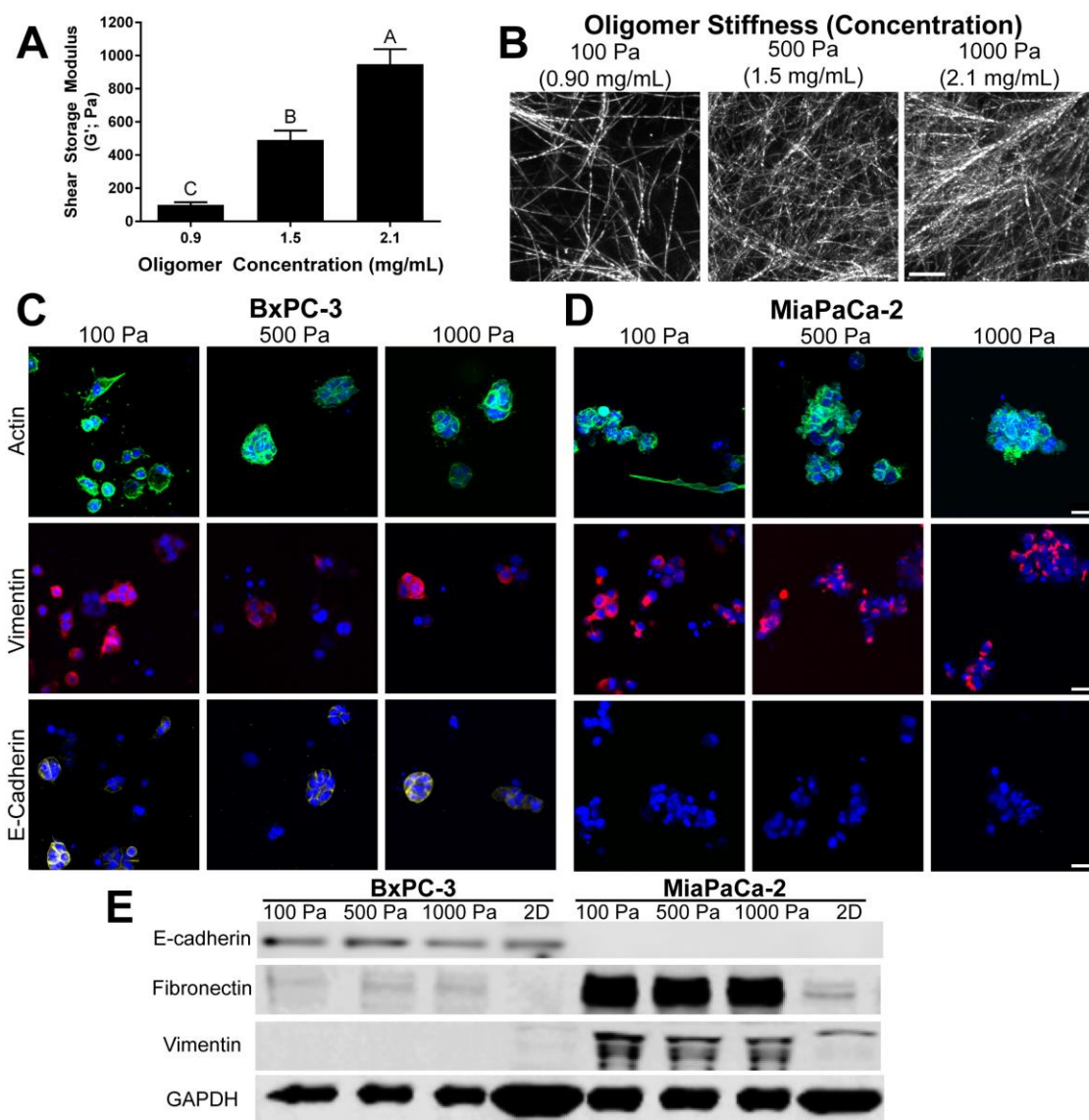
Figure 2-8 Stromal interstitial matrix stiffness alters PDAC cell phenotype.
(A) Matrix stiffness values of matrices prepared at Oligomer concentrations of 0.9, 1.5, 2.1 mg/mL are given as shear storage modulus (G'; mean $\pm$ SD) with letters indicating statistically different groups ($p < 0.05$, n=3). (B) Images represent z-stack projections of confocal reflection microscopy (10 μm thickness, scale bar = 10 μm) of matrices (C) BxPC-3 and (D) MiaPaCa-2 cells were cultured (2×10^5 cells/mL) within these three matrices for 4 days. Constructs were stained for actin (green), vimentin (red), E-Cadherin (yellow), and nuclei (blue) and imaged using confocal microscopy. Images represent z-stack projections (100 μm thickness; scale bar = 30 μm). (E) Western blot measurement of EMT protein expression for BxPC-3 and MiaPaCa-2 cultured for 4 days within various Oligomer matrices and on 2D tissue culture plastic

correlation between oligomer concentration, fibril density, and matrix stiffness has been established previously [18,57,74]. PDAC lines were cultured within Oligomer matrices prepared with stiffness values of 100, 500, and 1000 Pa and analyzed for changes in phenotype, S-phase fraction, and gemcitabine sensitivity. The S-phase fraction was quantified since gemcitabine causes checkpoint arrest and cell death by incorporating into DNA during S-phase [75].

When cultured in low stiffness (100 Pa) Oligomer, a significant subpopulation of BxPC-3 and nearly all MiaPaCa-2 cells took on a spindle-shaped, mesenchymal morphology. However, as Oligomer density and stiffness increased, both cell types grew as clustered aggregates, displaying more epithelial-like behavior (Figure 2-8C,D). Western blot data showed no appreciable changes in EMT marker protein expression as a function of Oligomer stiffness (Figure 2-8E). BxPC-3 expressed E-cadherin in the majority of cells in immunostained samples and also showed prominent bands for E-cadherin. On the other hand, while immunostaining showed vimentin expression in some BxPC-3 cells, expression was not detectable in western blots. Conversely, MiaPaCa-2 showed vimentin expression with no E-cadherin expression in all conditions in both immunostaining and western blots. Both lines showed fibronectin expression under each condition, though bands for BxPC-3 were very faint. Compared to cells cultured on 2D, Oligomer appeared to promote fibronectin expression in BxPC-3 and both fibronectin and vimentin expression in MiaPaCa-2 (Figure 2-8E). It is noteworthy that this upregulation was observed even though GAPDH (loading control) for 2D samples appeared heavier, despite efforts to load equal protein amounts for all samples. The heavier banding for 2D samples is likely due to some residual matrix protein in 3D samples, which would effectively decrease the ratio of cellular protein to total protein for 3D samples compared to 2D samples.

Finally, gemcitabine sensitivity and S-phase fraction were measured for BxPC-3 and MiaPaCa-2 cells within Oligomer of varied stiffness. Only IC50 values for BxPC-3 in 100 Pa were statistically ($p<0.05$) different from 500 Pa and 1000 Pa; however, both lines showed apparent inverted bell-shaped relationships with minima at 500 Pa (Figure 2-9A). Interestingly, these minima in gemcitabine sensitivity appeared to correlate with maxima in S-phase fraction, also at 500 Pa, albeit with no statistical significance (Figure 2-9B). Overall, these results show that matrix stiffness, altered through changing fibril density, can be a regulating factor in not only EMT, but also cell cycle progression and drug sensitivity.
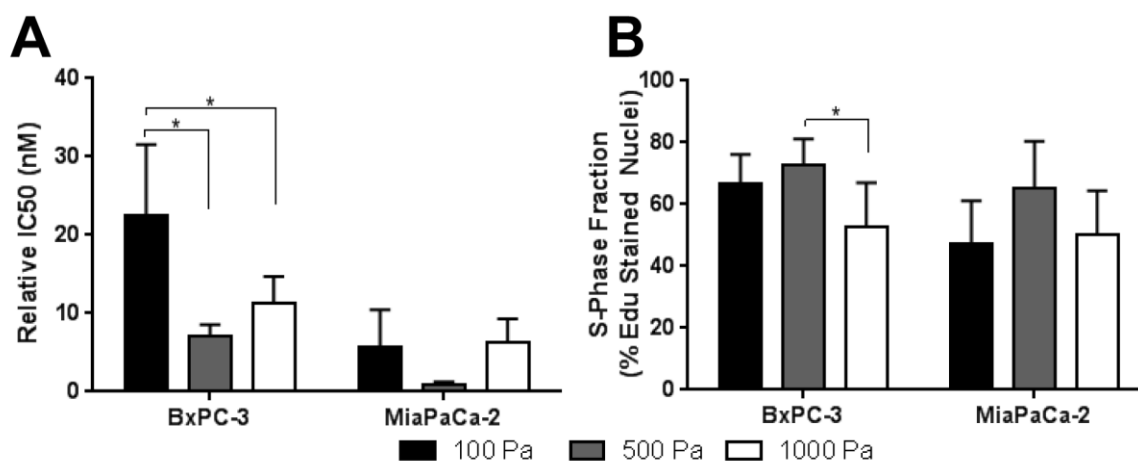
Figure 2-9 Stromal interstitial matrix stiffness alters PDAC gemcitabine sensitivity and proliferative capacity.
(A) Gemcitabine IC50 values (mean ± SD; n=3) and (B) S-phase fraction (mean ± SD; N=2, n=3) for BxPC-3 and MiaPaCa-2 cells cultured for 4 days within 3D Oligomer (2×10^5 cells/mL) prepared at stiffness values of 100 Pa (0.9 mg/mL), 500 Pa (2 mg/mL), and 1000 Pa (3 mg/mL). Asterisk (*) indicates statistically different groups (p<0.05); note that values between different cell types were not compared.

2.4   Discussion

In-vitro tumor models provide important basic research and drug screening tools; however, few adequately recreate metastasis and associated EMT, which remains the major cause of PDAC and other cancer-related deaths. The present work focused on 3D tumor-ECM model development, emphasizing the need for more accurate recapitulation of the PDAC desmoplastic ECM composition and microstructure, which is typically characterized by high levels of fibrillar type I collagen [76]. This fibrous, stiff ECM microenvironment is generally thought to compromise drug transport, decrease tumor chemosensitivity, and enhance EMT and tumor invasion [39,41,77]. However, our 3D tumor-ECM model revealed that PDAC phenotype and behavior vary significantly with initial tumor cell phenotype and depend largely on both the biochemical and biophysical properties of the surrounding stromal ECM. Although fibrillar type I collagen was found to generally promote enhanced expression of specific mesenchymal marker proteins, PDAC morphology as well as the extent of cell-ECM interactions and phenotypic heterogeneity were largely determined by matrix biophysical properties, namely fibril density and associated matrix stiffness. Such results are consistent with recent *in-vivo* preclinical studies that have shown dense type I collagen-fibril architectures restrain rather than promote PDAC EMT and metastasis [78,79].

The PDAC stromal ECM is comprised of BM and IM–two ECM types that differ substantially in their molecular composition, microstructure, and viscoelastic properties [80,81]. BM provides a thin, mechanically weak barrier that separates epithelium (e.g., glands, ducts) and endothelium (e.g., blood vessels, lymph vessels) from underlying interstitial tissues. It is primarily composed of type IV collagen which forms highly intertwined supramolecular networks with laminin, entactin, nidogen, and other molecules [82]. In contrast, IM is primarily composed of type I collagen which exhibits hierarchical self-assembly to form the D-banded fibrillar architecture of interstitial connective tissues. During IM synthesis and fibril self-assembly, intermolecular cross-links form between collagen molecules by an enzyme-mediated process, imparting significant stability and strength to the fibrillar matrix [83]. These two ECM types are of particular interest to PDAC because poor patient prognosis has been correlated with a decrease in BM proteins and a corresponding increase in IM content [76,84].
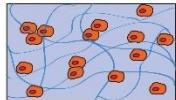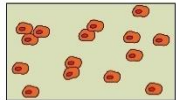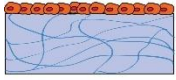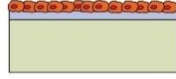
In the present work, Matrigel was used to approximate the BM, and Oligomer was used to recreate and tune the fibrillar IM microenvironment. While no research tools exist today that allow accurate BM recreation *in vitro*, Matrigel, a murine tumor BM extract, has been used extensively to mimic the BM in 3D cancer models. Although Matrigel as a natural hydrogel formulation contains many BM components, it does not exhibit the molecular cross-linking or architecture found in BM *in vivo* and shows significant lot-to-lot variability and low mechanical properties [80,85]. Oligomer, on the other hand, is a soluble type I collagen subdomain that, unlike conventional monomer formulations (atelocollagen and telocollagen), retains mature intermolecular cross-links formed *in vivo* [57]. As a result, this formulation exhibits high-order supramolecular assembly, giving rise to highly branched fibril networks with significantly improved physiological relevance, mechanical integrity, and resistance to proteolytic degradation [18,56,74,86]. Because Oligomer is standardized based upon its self-assembly or fibril-forming capacity, it supports tunability over a broad range of fibril microstructures and matrix stiffness values and shows excellent reproducibility within and between laboratories [18,74]. The distinct self-assembly capacity of Oligomer has been documented in previous published work, where polymerization of Oligomer over the concentration range of 0.5-4 mg/mL yields matrices with G' values of 40-1500 Pa while matrices prepared with telocollagen and atelocollagen, formulations commonly used in other studies, cover G' ranges of 2-300Pa and 2-50Pa, respectively [18]. The use of Oligomer in the present work allowed PDAC cells to engage type I

collagen IM in a natural fibrillar context with systematic control of fibril density and associated matrix stiffness.
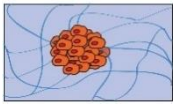
Table 2-1 summarizes various *in-vitro* tumor models used for EMT and invasion studies, highlighting culture format, ECM scaffold material, and ECM biophysical properties as critical design parameters for recreating pathophysiologically relevant cell-matrix interactions *in vitro* [13,87]. Based on this review, the majority of EMT and invasion studies performed to date have focused on breast cancer, underscoring a need for more pancreatic cancer investigations. Most work targeting ECM-guided EMT has been performed using cell monolayers grown on either 2D plastic surfaces with adsorbed matrix proteins or on-top of 3D substrates (also known as semi-3D). On the other hand, studies focused on tumor invasion, a hallmark of metastasis, involve embedding multi-cellular spheroids or organoids within 3D matrices prepared from monomeric type I collagen. Although not addressed specifically in the table, this review also revealed that culture format often dictates whether cellular or population level analyses are used and that 3D embedment experiments often lack population level evaluations [68–70]. Finally, only one other tumor EMT study was identified that involved 3D embedment of single cells within a fibrillar type I collagen matrix, which is more representative of the tumor IM than Matrigel or bioengineered hydrogels, such as those prepared from polyethylene glycol (PEG) or alginate. These gaps are addressed, in part, by the present work.

Since modulation of the tumor ECM context and associated EMT are likely more of a continuum rather than a binary change [88], the influence of ECM composition and microstructure on tumor cell phenotypic transition was documented by varying IM:BM (Oligomer: Matrigel) ratio while maintaining a constant matrix stiffness. Interestingly, when three different PDAC lines were exposed separately to low-density Oligomer (100 Pa), they maintained their mesenchymal phenotype or showed evidence of EMT, with resultant morphology and protein expression profiles dependent upon initial cell line phenotype. On the other hand, Matrigel (100 Pa) inhibited EMT, promoted a clustered morphology for all cell types, and decreased mesenchymal protein expression. Such observations are consistent with the general expectation that IM is associated with mesenchymal behavior, and BM is involved in maintaining epithelial phenotype [89–91]. However, few *in-vitro* studies have demonstrated how simultaneous interaction of tumor cells with IM and BM contributes to EMT and phenotypic

Table 2-1 Models used to study role of ECM on EMT and invasion

Model	Schematic and Description	Cancer Type	Outcomes	Ref.
2D coatings (molecular)	• Non-fibrillar • Type I collagen	pancreatic	• Molecular type I collagen increases EMT via α2β1 integrin mediated E-cadherin downregulation and vimentin upregulation	[63,64,66]
3D single cell embedment	• Fibrillar • Type I collagen	pancreatic	• Type I collagen Oligomer promotes EMT of cells with Smad4 deletion • Matrigel promotes MET and hinders EMT • Interaction with collagen fibrils and BM components in Matrigel Increases invasive phenotype of transitioned cells • Increasing fibril density decrease mesenchymal nature of cells	Present work
		breast	• Type I collagen monomer matrices promote invasive phenotype • Matrices with small amount of Matrigel promote acinar morphology	[91]
	• Non-fibrillar • PEG or alginate hydrogels	pancreatic	• Exposure to TGF- β1 and EGF is necessary for EMT of cells grown in PEG hydrogels admixed with molecular type I collagen	[92]
		pancreatic	• Exposure to TGF-β1 Is necessary for EMT of cells grown in RGD-alginate • TGF- β1 removal results in EMT reversion (MET)	[93]
		breast, prostate, lung	• Incorporating GFOGER peptide (α2β1 integrin binding sequence) into PEG hydrogels increases invasive phenotype	[68]
Semi-3D (3D on top)	• Fibrillar • Type I collagen	breast	• Larger fibril diameter leads to more spread, less clustered phenotype • Increasing fibril diameter and decreasing pore size increase invasiveness	[67]
		breast	• Increasing fibril density of underlying collagen produces more proliferative, invasive phenotype	[52]
		breast	• Type I collagen monomer matrices promotes mesenchymal phenotype • Matrices with laminin and collagen combined promote "invasive networks" of cells	[89]
	• Non-fibrillar • ECM-coated Polyacrylamide	breast	• Increasing stiffness of type I collagen monomer- or Matrigel-coated polyacrylamide induces EMT	[51]
		breast	• Increasing stiffness of Matrigel-coated polyacrylamide promotes a more invasive phenotype and loss of regular epithelial organization	[52]
		lung	• Increasing stiffness of fibronectin-coated substrates increases EMT • Inhibiting cell contractility abrogates this relationship suggesting contractile machinery is necessary for EMT	[94]

(Table 2-1 continued)

Model	Schematic and Description	Cancer Type	Outcomes	Ref.
3D spheroid or organoid embedment	• Fibrillar • Type I collagen	breast	• Increasing fibril density of type I collagen monomer matrices decreases spheroid invasiveness	[53]
		breast	• Maximum invasiveness and loss of epithelial organization occurs at intermediate density (stiffness) of type I collagen monomer matrices	[95]
		breast	• Maximum invasiveness occurs within mixture of Matrigel and type I collagen	[96]
		glioblastoma	• Maximum invasiveness occurs at intermediate stiffness of type I collagen Oligomer matrices	[55]
		breast	• Cells were most invasive and most sensitive to drugs going into low fibril density matrix (type I collagen monomer)	[54]
		breast	• Compared to Matrigel, type I collagen monomer increased invasiveness and mesenchymal phenotype of organoids	[90]

Note: EMT – Epithelial to Mesenchymal transition; MET – mesenchymal to epithelial transition; TGF-β1 – transforming growth factor β1; EGF – epidermal growth factor; PEG – Polyethylene glycol; RGD – Arginine Glycine-Aspartic acid

heterogeneity. Those studies that have done so, did not examine matrix microstructure and mechanics or compare different cell lines across the EMT spectrum [89,91,96].

In the present work, Matrigel induced epithelial BxPC-3 cells to grow as tight clusters, even when it was present in small amounts together with fibrillar type I collagen. Only in the 100:0 ratio, which had no Matrigel, did a subset of BxPC-3 undergo EMT, as indicated by a subpopulation of cells demonstrating spindle-shaped morphology, prominent vimentin staining, and some loss of E-cadherin staining. Population analysis by western blots supported the notion of matrix-induced EMT heterogeneity with little change in vimentin or E-cadherin expression and faint upregulation of fibronectin, another common marker for the mesenchymal phenotype. These findings for the epithelial PDAC line are consistent with a recent study where embedded normal mammary epithelial cells, MCF-10, only appeared invasive in monomeric type I collagen matrices [91]. When even small amounts of Matrigel were added to type I collagen matrices, MCF-10 displayed a more epithelial acinar phenotype.

On the other side of the EMT spectrum, MiaPaCa-2, which are classified as mesenchymal, showed more drastic morphological changes, as well as a decrease in

mesenchymal protein expression as IM:BM ratio increased. An interesting observation was that combined IM and BM interactions in the 75:25 ratio appeared to promote a more invasive, elongated morphology than IM alone. Benton and colleagues reported similar findings with mesenchymal breast cancer cells, MDA-MB-231, which displayed the most invasive, migratory phenotypes when cultured on-top or embedded as spheroids within matrices prepared from monomeric type I collagen and Matrigel [89,96]. Although the above-mentioned studies did not evaluate the matrix physical properties of IM-BM combinations, we noted that the 75:25 ratio was the only mixture of IM and BM that maintained the branched fibrillar architecture of type I collagen and the associated matrix stiffness (100 Pa). In summary, these observations suggest that for epithelial cells, Matrigel promotes epithelial morphogenesis regardless of the presence of an interconnected collagen fibrillar matrix, but for mesenchymal tumor cells, a stable, interconnected collagen fibrillar matrix with sufficient mechanical integrity is a primary factor in driving invasive phenotypes. These results also point to the need for further work to define how complex cell-ECM interactions such as those found at the tumor-stroma interface contribute to phenotypic heterogeneity and the continuum of EMT phenotypes observed *in vivo* [97].

Comparisons between our results and those in Fig 10 also revealed that the manner in which cells sense and respond to changes in substrate stiffness is highly dependent on the *in-vitro* model format (e.g., coated 2D, semi-3D, 3D embedded). Our results showed promotion of EMT and mesenchymal characteristics (e.g. spindle-shaped morphologies, vimentin and fibronectin expression) in PDAC cells embedded within relatively low-density collagen fibril matrices formed from Oligomer. When fibril density was increased, the resulting increased matrix stiffness and spatial constraints hindered mesenchymal-like cell spreading and resulted in confined, clustered growth. These results contradict observations from semi-3D models which have shown cells on-top of soft substrates maintained epithelial characteristics (clustered growth, E-cadherin expression, BM deposition) while increased substrate stiffness increased EMT-like behaviors including cell spreading, migration, and vimentin or fibronectin expression [51,52,94,98]. This trend was observed whether the underlying substrate on which cells were cultured was fibrillar type I collagen or non-fibrillar coatings of molecular type I collagen, Matrigel, or fibronectin on-top of PA gels. Therefore, the observed discrepancy between our results and those of semi-3D models is likely due to differences in geometric constraints. Specifically, the forced apical-basal polarization of cells imposed by semi-3D model geometry

has been shown to alter the composition of cell-matrix adhesions and downstream signaling pathways in a manner different than 3D embedment models [99,100]. Assuming that EMT correlates with invasiveness, our results align more closely with those from 3D spheroid embedment models in which the most invasive phenotypes were observed in either the lowest or an intermediate stiffness type I collagen matrix while remaining more clustered at higher stiffness [53–55,95]. These 3D embedment models, including the present work, demonstrate that physical constraints experienced by cells within dense 3D matrices dominate over any increased signaling that may occur from increased ligand density or increased substrate stiffness as observed with semi-3D models. While some *in-vitro* studies aim to decouple matrix density and stiffness through non-natural matrix crosslinking [91,101], the relevance of these methods remains unclear since these two variables are naturally coupled with desmoplasia *in vivo* [79,101]. Taken together, these comparisons highlight that when developing accurate *in-vitro* tumor-ECM models, it is not just the presence of specific ECM ligands or "going 3D" that is important, but one must consider culture geometry, ligand presentation, and fibrillar architecture since all these features dictate EMT mechanobiology *in vivo*.

Our results also highlight two important, often overlooked aspects of 3D *in-vitro* models – the cell-matrix tension balance and the collagen fibril architecture [99,102]. In cancer, loss of cell-matrix tensional homeostasis and cell-induced alignment of type I collagen fibrils have been implicated in tumor progression and invasion [38,52]. Specifically, researchers have shown that increasing matrix tension by applying passive strain to monomeric type I collagen matrices increased invasiveness of embedded mammary organoids [95]. On the other hand, relieving intra-matrix tension by detaching similar collagen matrices from a culture dish caused mammary epithelial cells to grow as tight acinar-like structures rather than the invasive, spindle-shaped morphologies observed in attached matrices [91]. In the present work, the high levels of Matrigel in low IM:BM ratios (50:50, 25:75) disrupted collagen fibril interconnectivity, which likely hindered cells ability to generate force and create tensional strain within the matrix. These mechanical changes, along with the BM signaling from Matrigel, are likely what caused clustered cell growth of both cell lines in these matrices. On the other hand, the type I collagen composition and interconnected fibril matrix of Oligomer (100:0) were sufficient to induce EMT of BxPC-3. Contrary to this result, non-fibrillar hydrogels such as collagen-PEG or RGD-alginate have been shown to not promote EMT in embedded pancreatic or breast cancer cells

unless exogenous growth factors, such as TGF-β1, were added [92,93]. It is important to note here that bioengineered materials such as those fashioned from alginate or PEG have no inherent bioactivity and lack physiologically relevant architecture. Even when molecular collagen (non-fibrillar) or RGD ligands are added to promote cell adhesion the architecture, mechanical properties, and resultant cell-substrate interactions that occur within these artificial microenvironments are dramatically different from those experienced by cells *in vivo*. From these observations, it is clear that in-vitro models of tumor EMT and invasion should be designed to accurately recreate ECM architectural features and cell-matrix mechanics for improved correlation between *in-vitro* and *in-vivo* behavior [38,99].

In addition to highlighting the importance of collagen fibril architecture in mechanistic study of tumor EMT and mechanobiology, observations from this work demonstrate the translational potential of Oligomer-based tumor-ECM models. Oligomer is unique among type I collagen formulations because of its purity, standardization, and ability for user customization, making it a powerful tool for creating standardized 3D models [18,57,103]. Additionally, its molecular make-up and its ability to form tissue-like collagen matrices with mature intermolecular crosslinks make Oligomer an ideal material for predicting *in-vivo* outcomes through recreating the ECM environment of desmoplastic tumors such as PDAC which are rich in type I collagen [32,56,57,76]. In fact, the observed trend in increased EMT behavior with decreased matrix density in the present work, has been recently noted in genetically engineered mouse models of PDAC [78,79]. In these studies, reduced stromal cell activity led to decreased desmoplasia and tumor stiffness which led to increased EMT, invasion and metastasis, as well as lower overall survival rates. The matrix-induced EMT heterogeneity in low-density Oligomer matrices is also reminiscent of observations from human clinical tumor samples in which only a subpopulation of cells undergoes EMT [97,104]. Finally, although only minor significant differences in drug sensitivity were found, this study demonstrates our ability to perform drug dosing experiments and generate IC50 values for these 3D tumor-ECM models. Collectively, these observations showcase the potential of Oligomer to serve as a robust platform for mechanistic study of metastasis and creation of predictive 3D drug screening models.

2.5   Conclusion

   This work serves as a first step in the development of novel *in-vitro* 3D tumor-ECM models where Oligomer is used as a standardized type I collagen formulation to recreate and customize the IM component. From the foundational understanding of PDAC desmoplasia and EMT gained from these experiments, we can now develop more complex models of pancreatic and other cancers to systematically define the role of other prominent components of the tumor stromal microenvironment and study tumor invasion in more detail. Additionally, the model of matrix-driven EMT created by embedding PDAC cells within Oligomer-based fibril matrices provides a useful tool that can be applied to further mechanistic study. Finally, by developing and applying standardized *in-vitro* models with defined ECM microenvironments, we are moving closer to accurately recreating tumor-stroma interactions and desmoplasia to provide pathophysiologically relevant PDAC models which can be used for phenotypic drug screening to ultimately predict therapeutic response and improve patient outcomes.

3. DEVELOPMENT OF A NOVEL HIGH-THROUGHPUT, HIGH-CONTENT PHENOTYPIC SCREENING MODEL FOR METASTASIS

3.1 Introduction

Despite progress in treating some cancers, metastatic tumors remain nearly impossible to treat, thus metastasis continues to be the predominant cause of cancer-related deaths [25]. This problem is especially apparent for highly metastatic cancers like pancreatic ductal adenocarcinoma (PDAC), where approximately 90% of patients present with invasive or metastatic disease [30]. While the lack of treatment options for patients with metastases represents a multi-facetted problem, one of the biggest shortcomings is the lack of predictive preclinical metastasis models that can be used for mechanistic studies and drug screening [25,29]. Since metastasis involves tumor cell engagement, invasion, and remodeling of the surrounding tissue extracellular matrix (ECM), it is becoming increasingly clear that accurate recreation of such three-dimensional (3D) cell-ECM interactions and associated mechanobiology is critical to the development of more predictive *in-vitro* models [35,105]. For PDAC, in particular, fibrous connective tissue deposition mediated by cancer associated fibroblasts (CAFs), known as desmoplasia, represents another tumor-associated change in ECM composition and biophysical properties that has been associated with metastasis and implicated as a negative prognostic indicator [76]. Altogether, this points to a need for preclinical metastasis models that effectively recreate key features of tumor-stroma interactions such as those in PDAC desmoplasia.

With this need in mind, it is also important to consider how the overall drug development process informs preclinical model development. Pharmaceutical companies, in general, rely on two main drug development strategies, specifically molecular target-based screening and phenotypic screening [9]. Molecular target-based screening, which has been industry standard for nearly 30 years, involves an identified molecular target (e.g., signaling protein) and associated biochemical screens focused on protein-protein interactions or enzyme activity. This process is extremely time and resource intensive because, by definition, one must know the mechanism of action of both the disease-related molecular target and the candidate drugs at the forefront of development. Phenotypic screening, on the other hand, begins with developing a

disease model and associated assays focused on specific disease characteristics. One advantage of this approach is that these phenotypic models are more physiologically relevant than models used early in target-based screening since they are cell- or tissue-based rather than protein- or enzyme-based. Further, phenotypic screening is an attractive strategy because it does not require complete understanding of molecular mechanisms at the onset of drug development and is conducive to drug repurposing screens [9]. Additionally, between 1999 and 2008, the majority of newly approved drugs were developed using phenotypic screening despite target-based screening being far more widely used in industry [7]. For these reasons, it has been suggested that increased use of phenotypic screening may help reduce the high attrition rate of clinical trials and should be the focus of preclinical model development [7,9,10].

When developing next-generation *in-vitro* phenotypic models of tumor metastasis, a number of design criteria must be considered. Specifically, while there is advocacy that added model complexity (inclusion of vasculature, various stromal and immune cells) may increase pathophysiologic relevance and predictive power, such approaches fall short with respect to practical logistics [22,23,106]. For such models to gain traction and widespread use within both pharmaceutical and academic environments, they must also be user-friendly, time-efficient, reproducible, standardizable, scalable, and ideally, amenable to high-throughput automation (e.g. automated imaging systems, liquid handling robots) [23,36]. Additionally, to achieve their full potential, phenotypic models should be combined with high-content multiplex optical analyses rather than traditional population-level spectrophotometric measures of cell viability [36,107]. Finally, phenotypic model readouts should be correlated with *in-vivo* or clinical outcomes to effectively support validation and translation of their predictive power [10,24]. While some models meet a few of these criteria, there remains a paucity of model standardization and validation in the published literature. Finally, few, if any, 3D *in-vitro* models achieve an appropriate balance between pathophysiologic relevance and practical considerations to enable translation to high-throughput, high-content (HT-HC) drug screening [22,23].

Conventional in-vitro metastasis models focus tumor cell migration and invasion [108]. Transwell (Boyden chambers), wound healing, and cell exclusion-zone assays represent the most commonly used migration models, however the geometry and artificial constraints of these models limit their physiologic relevance [108]. To better recreate tumor invasion, 3D spheroid invasion models, where multicellular tumor spheroids are embedded within various 3D matrices,

are becoming increasingly common [108–110]. However, adoption of these models as HT-HC screening models is hampered by their lack of standardization and challenges associated with scaling for high-throughput screening analyses. Specifically, these shortcomings include the following: i) the time consuming nature of spheroid creation [36,108]; ii) the lack of user control of spheroid size, shape, and cell density [21,111]; iii) the widespread use of Matrigel and conventional monomeric type I collagen formulations giving rise to reproducibility issues and questionable relevance of the ECM biophysical properties [112,113]; and iv) the inability to reproducibly embed spheroid within 3D matrices [111]. To the best of our knowledge, there is no phenotypic metastasis model which addresses the above-mentioned shortcomings by supporting reproducible creation and embedment of customizable tumor spheres within a standardized and customizable tissue ECM compartment (96-well format) for HT-HC phenotypic screening.

To address the above-mentioned gap, the goal of this work was to develop a standardized HT-HC phenotypic screening model of PDAC metastasis that is both pathophysiologically relevant and practical to implement. The model was inspired, in part, by a "multi-tissue interface" model that was originally developed for vasculogenesis/angiogenesis studies [114]. This model provides a high-degree of user customization and standardization, as it applies standardized self-assembling type I oligomers for creation of two adjacent, independently-tunable tissue compartments (Figure 3-1A). To adapt and translate this model for HT-HC drug screening, a custom-designed 96-well fabrication platform was created. This low-cost, 3D-printed platform consists of an array of posts that supports rapid (within minutes) tumor sphere formation and embedment (Figure 3-1B). The platform readily integrates with standard 96-well culture plates making tumor sphere embedment within the surrounding tissue compartment user friendly and highly reproducible (Figure 3-1C). Finally, this platform enables precision placement of the sphere within the 3D tissue compartment, which is essential for integration with automated 3D image collection via confocal microscopy. The present work represents the first steps in verification and validation of this custom fabrication platform and the associated HT-HC PDAC metastasis model for anti-cancer drug screening.
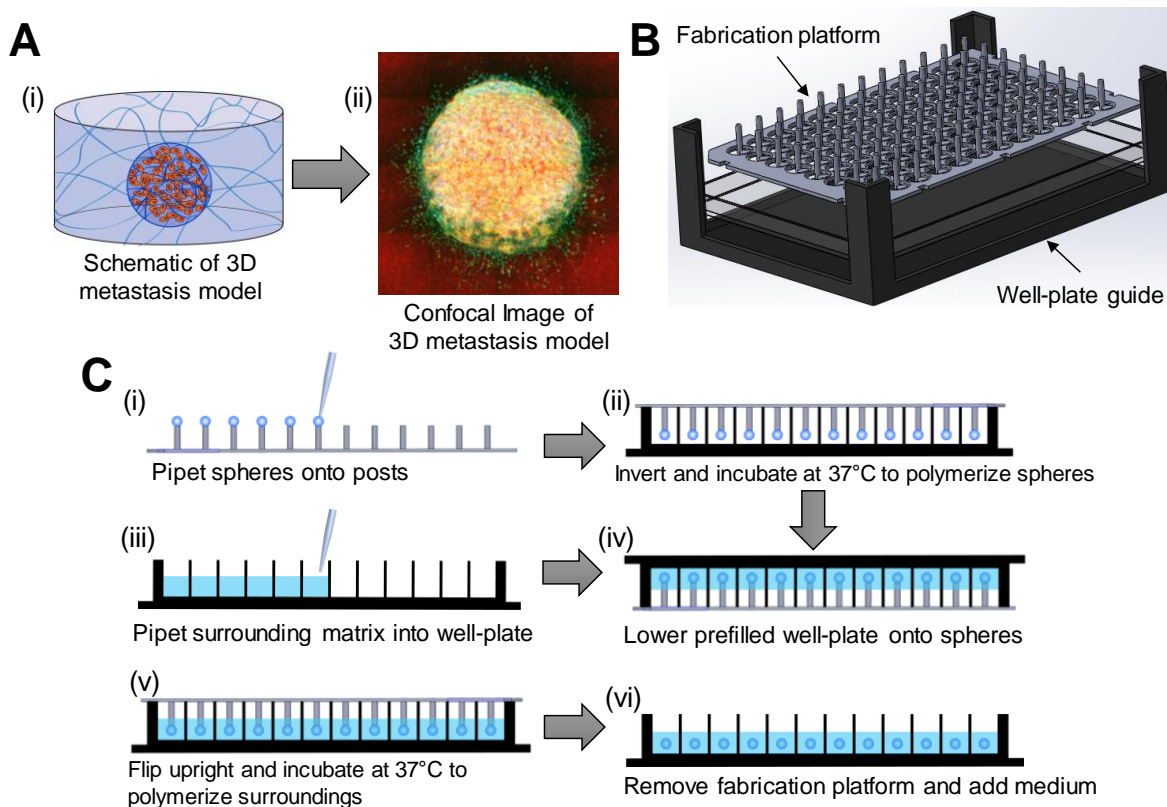
Figure 3-1 Overview of fabrication platform and 3D HT-HC metastasis model.
(A) (i) Schematic of 3D metastasis model and (ii) a representative image of tumor cells invading from the sphere into the surrounding matrix. Image represents 16 fields of view, each of which is a maximum projection of a 400 μm z-stack (20 μm step; 21 slices) of a tumor sphere (Panc-1) after 5 days of culture; green = actin (phalloidin), blue = nuclei (Hoechst 33342) and red = fibrillar collagen (confocal reflectance). (B) CAD drawing of custom-designed fabrication platform and associated well-plate guide which are used to rapidly and reproducibly create the 3D metastasis model. (C) Process diagram of experimental set up using fabrication platform. (i) Spheres are pipetted onto the posts of the fabrication platform using a multi-channel pipet. (ii) Posts are covered with a 96-well plate and incubated at 37 °C to allow for Oligomer self-assembly (polymerization). (iii) The wells of another 96-well plate are filled with Oligomer solution which will serve as the surrounding matrix. (iv) After sphere polymerization, the prefilled well plate is inverted and lowered onto the spheres (v) The plate is then flipped upright and incubated again to polymerize surroundings. (vi) Fabrication platform is removed, and culture medium is added. Note: Well plate guide is not shown in (C) but is used to aid in the placement of well-plates on-top of the fabrication platform.

3.2 Materials and Methods

3.2.1 Model development, optimization and validation

3.2.1.1 Cell culture

Established PDAC cell lines, BxPC-3 and Panc-1, were obtained from American Type Culture Collection (Manassas, VA) and were grown in RPMI-1640 (Life Technologies, Grand Island, NY) and high glucose DMEM (Hyclone, Logan, UT), respectively. Low-passage patient-

derived PDAC cells, 10.05 and Pa03C, as well as the CAFs were grown in high glucose DMEM without sodium pyruvate (Life Technologies). All medium was supplemented with 10% heat inactivated fetal bovine serum (HI FBS; Life Technologies), and BxPC-3 and Panc-1 medium was also supplemented with 100 U/mL penicillin and 100 µg/mL streptomycin (Sigma Aldrich, St. Louis, MO). Cells were maintained in a humidified environment of 5% CO_2 in air at 37°C. All cells were passed when they reached 70-90% confluency; established PDAC lines and CAFs were used below passage 20 and patient-derived PDAC cells were used below passage 10.

3.2.1.2   Creation of 3D HT-HC metastasis model

Type I collagen Oligomer was derived from the dermis of market-weight pigs as previously described [18]. Oligomer was dissolved in 0.01 N hydrochloric acid (HCl) and standardized based on molecular composition and polymerization capacity according to ASTM International Standard F3089-14 [103]. Polymerization capacity is defined as the relationship between shear storage modulus (G', Pa) of the self-assembled (polymerized) matrix and Oligomer concentration. To achieve matrices of defined fibril density and matrix stiffness, Oligomer was diluted with 0.01 N HCl to desired concentration and neutralized with a proprietary 10X Self-Assembly Reagent. In this study, Oligomer matrices were prepared at stiffness values of 200 and 500 Pa, which correspond to concentrations of approximately 1.5 and 2.3 mg/mL, respectively. Validation that the high cell density used for tumor-sphere formation did not significantly alter Oligomer self-assembly capacity was performed with 1.5 mg/ml matrices (data not shown).

The model fabrication platform was designed in Solid works (Dassault Systemes Solidworks Corp., Waltham, MA) and 3D printed on a Fortus 400mc 3D Production System (Stratasys, Eden Prairie, MN) using acrylonitrile butadiene styrene (ABS). Overall dimensions and post spacing were optimized to accommodate glass-bottom 96-well plates (Cellvis, Mountain View, CA). A well-plate guide was created to aid in uniform and controlled placement of the spheres within all wells (Figure 3-1). The platform and well-plate guide were rendered aseptic by spraying with 80% ethanol and ultraviolet light exposure. Model setup using the fabrication platform is summarized in Figure 3-1C. First, to create tumor spheres, cells were suspended in neutralized Oligomer at 1x107 cells/mL, and 5 µL drops were pipetted onto posts with a multi-channel pipette. For co-culture experiments, CAFs were added to the Oligomer-cell

suspension at a tumor cell to CAF ratio of 1:1 while maintaining an overall cell concentration of 1×10^7 cells/mL. Once spheres were pipetted onto the posts, the platform was covered with a 96-well plate, inverted and incubated at 37°C for 8-10 min to allow Oligomer self-assembly. During this incubation time, the wells of another 96-well plate were filled with 100 μL of Oligomer, and once spheres were polymerized, this prefilled well plate was lowered onto the platform using the well-plate guide to position the posts in the center of each well and embed spheres within Oligomer. This well plate was then flipped upright and incubated again at 37°C for 15 min to allow full polymerization of the surrounding matrix. Subsequently, the fabrication platform was removed from the well plate and the appropriate medium added. Experiments comparing Panc-1 and BxPC-3 were cultured for 5 days while drug dosing experiments and those with patient-derived lines were 4 days.

3.2.1.3   Analysis of metastatic phenotype: invasion and EMT

For invasion analysis, tissue constructs were fixed with 3% paraformaldehyde (Mallinckrodt, Derbyshire, UK), permeabilized using 0.1% Triton X-100 (Sigma Aldrich), and stained to visualize actin (Alex Flour 488 or 546 phalloidin; Life Technologies) and nuclei (Draq5 or Hoechst 33342; Life Technologies). Images were collected using laser scanning confocal microscopy with 10x objectives on either an Olympus IX81 inverted microscope with an Olympus Fluoview FV1000 system (Olympus, Tokyo, Japan) or a Zeiss LSM 880 (Zeiss, Oberkochen, Germany). Images were acquired such that the edge of the sphere was along one edge of the image and took up approximately one quarter of the total imaging volume (850×850×150 μm). To quantify tumor cell invasion, image analysis was performed on 3D renderings of confocal image stacks using the "Cell" analysis package in Imaris (Bitplane, Concord, MA). Briefly, the sphere boundary was defined by thresholding the phalloidin channel to create an object of approximately 2 mm diameter. Nuclei of invading cells were identified by creating 10 μm diameter spots (approximate diameter of average nucleus) using the Draq 5/Hoechst 33342 channel. The distance between the sphere boundary and every nucleus was then calculated and any values less than zero were excluded. Batch processing was used to analyze all images from a given experiment, followed by manual inspection and adjustment to ensure that intensity thresholds appeared appropriate for each image. Data was used to calculate total number of invading cells, average invasion distance, and maximum invasion distance. Two-

factor ANOVA with Tukey-corrected pairwise comparisons (GraphPad Prism, GraphPad Software Inc., San Diego, CA) were used to determine statistical differences (p< 0.05).

To analyze EMT protein expression constructs were also processed for immunostaining. After fixation with 3% paraformaldehyde (Mallinckrodt), constructs were soaked in 30% sucrose solution for 3 days, embedded in Optimum Cutting Temperature (OCT) compound (Fisher Healthcare, Houston, TX), and frozen overnight at -80°C. Frozen constructs were sliced with a Thermo Cyrotome FE (Thermo Fisher, Kalamazoo, MI) to create 60 µm cryosections that were placed on Superfrost Plus glass slides (Thermo Scientific). Sections were blocked with 1% bovine serum albumin (Jackson ImmunoResearch, West Grove, PA) followed by overnight incubation at 4 °C with primary antibodies and 1 hour incubation at room temperature with secondary antibodies. Slides were then rinsed and mounted using Fluro-Gel (Electron Microscopy Sciences, Hatfield, PA). Primary antibodies included mouse anti-vimentin (V6389. Sigma Aldrich) and rabbit anti-E-cadherin (24E10, Cell Signaling Technologies, Danvers, MA). Alexa Fluor 405, 488, and 633 secondary antibodies (Life Technologies) of matched species were used to visualize via immunofluorescence. Slides were counterstained with Hoechst 3342 (Life Technologies) for visualization of nuclei. Images were collected using laser scanning confocal microscopy with 10x or 20x objectives on either an Olympus IX81 inverted microscope with an Olympus Fluoview FV1000 system (Olympus, Tokyo, Japan) or a Zeiss LSM 880 (Zeiss, Oberkochen, Germany).

3.2.2 Proof of concept HT-HC screening

3.2.2.1 Drug dosing and high-content assay

For proof of concept HT-HC drug screening, medium containing drugs was added 24 hours after model setup, and refreshed every 24 hours thereafter for a total treatment time of 72 hours (3 days). Gemcitabine (Alfa Aesar, Tewksbury, MA) was applied as a standard 10-point drug dilution with a starting concentration of 200 µM and a 1:5 dilution. Staurosporine (Alfa Aesar ;20 µM) and DMSO (Sigma Aldrich; 1%) were used as kill and vehicle controls, respectively. For the high-content assay, Click-iT Edu Alexa Flour 488 (ThermoFisher) and MitoTracker Red CMXRos (ThermoFisher) were used to measure proliferation and metabolic activity, respectively. Twenty-four hours prior to fixation, 10 µM 5-ethynyl-2'-deoxyuridine (Edu) and 500 nM Mitotracker were added in serum-free medium along with the final drug

treatment. After fixation with 3% paraformaldehyde (Mallinckrodt), constructs were rinsed with 1% BSA (in 1X PBS), permeabilized with 0.1% Triton X-100 (Sigma Aldrich), and incubated overnight at 4°C with Click-iT reaction cocktail prepared according to manufacturer's instructions. Finally, constructs were counterstained with Hoescht 33342 (Life Technologies).

3.2.2.2   HT-HC imaging and analysis

Automated confocal imaging was performed using an Opera Phenix High-content Screening System (Perkin Elmer, Waltham, MA). Imaging parameters, including exposure time, laser power, and imaging depth were determined based on vehicle control wells and applied to the entire well-plate. To capture the full diameter of the tumor sphere in addition to the surrounding matrix, six fields of view from a 10X objective were obtained, with each field representing a 500 μm confocal z-stack (25 μm per step size; 21 slices) which started at the bottom of the sphere. Subsequent image analysis was performed in Harmony Software (Perkin Elmer) using maximum intensity projections of tiled images to evaluate cell proliferation, metabolic activity, and invasion (Supplemental Figure S 1). The first step of the analysis process was detection and quantification of all cell nuclei. For invasion analysis, an image region was created by blurring the Mitotracker channel with a gaussian filter, followed by thresholding to create a "sphere region" approximately the same diameter as the whole sphere. The number of invading cells was determined by subtracting the number of nuclei within the "sphere region" from the total number of cells. Proliferative capacity was calculated by counting all Edu-labeled nuclei and normalizing this number to the total number of nuclei in each image. To calculate relative metabolic activity, the raw Mitotacker channel was thresholded to define a "metabolic region," and the fluorescent intensity of the Mitotracker channel was summed within this region.

The proliferative capacity, relative metabolic activity, and number of invading cells for each well were then normalized to the kill and vehicle controls using the following equation: $\% \, Responsse = (A_n - A_{STS})/(A_{DMSO} - A_{STS}) \times 100\%$. A_n represents the value of the *nth* dilution. *A_{STS}* and *A_{DMSO}* represent values from kill control and vehicle control, respectively. This data was used to fit three-parameter logistic curves in GraphPad Prism (GraphPad Software Inc.), from which IC50 and E_{max} values were calculated. These values were obtained from three independent experiments (N=3) and compared using a one-factor ANOVA with Tukey-corrected pairwise comparisons. Differences were considered significant when $p < 0.05$.

3.3   Results

3.3.1   Fabrication platform supports user-friendly, rapid and reproducible model setup

3D spheroid invasion models suffer from a number of shortcomings including i) multiple day setup, ii) lack of spheroid and ECM standardization and user control, and iii) inability to accommodate automated HT-HC imaging [36,106,111]. Since a lack of standardized and reproducible setup are at the foundation of these limitations, our goal was to design a platform which facilitated rapid and reproducible creation of tumor spheres with precision embedment within a surrounding type I collagen-fibril matrix. As shown in Figure 3-1, the platform consists of an array of posts, specifically spaced to match dimensions of a standard 96-well plate. Post tips were designed with a slight curvature to provide the necessary surface tension for sphere fabrication, adhesion, and transfer. Post length was optimized along with a well plate guide so that spheres were reproducibly and precisely positioned within the center of each well, 1 mm from the well bottom in user-friendly fashion. These design features allowed the sphere to be completely surrounded by matrix in a standardized location within the well-plate to facilitate automated confocal imaging. When used in conjunction with a multi-channel pipette, this platform supported rapid model setup within less than 30 minutes by various users in academic and industrial laboratories. Overall, this simple yet novel design provides a user-friendly interface for rapid, reproducible creation and embedment of tumor spheres, overcoming many of the shortcomings of 3D spheroid invasion models.

3.3.2   Novel 3D metastasis model supports independent customization and optimization of ECM biophysical properties of both tumor and surrounding tissue compartments

Another commonly mentioned shortcoming of 3D *in-vitro* cell culture models, in general, is the lack of standardization and tunability of matrix composition and biophysical properties [115]. Such user-control is desired for drug screening to optimize assay dynamic range, as well as mechanistic mechanobiology studies. As stated previously, Oligomer, the type I collagen formulation used in this study, is standardized based on its self-assembly capacity, with shear storage modulus of the self-assembled matrix representing a quantifiable functional parameter which has been correlated with oligomer concentration and fibril density [18,103]. Additionally, Oligomer preserves the telopeptide ends of collagen triple helices and the natural intermolecular crosslinks that exist in mature tissue collagen, leading to branched fibrillar matrices similar to
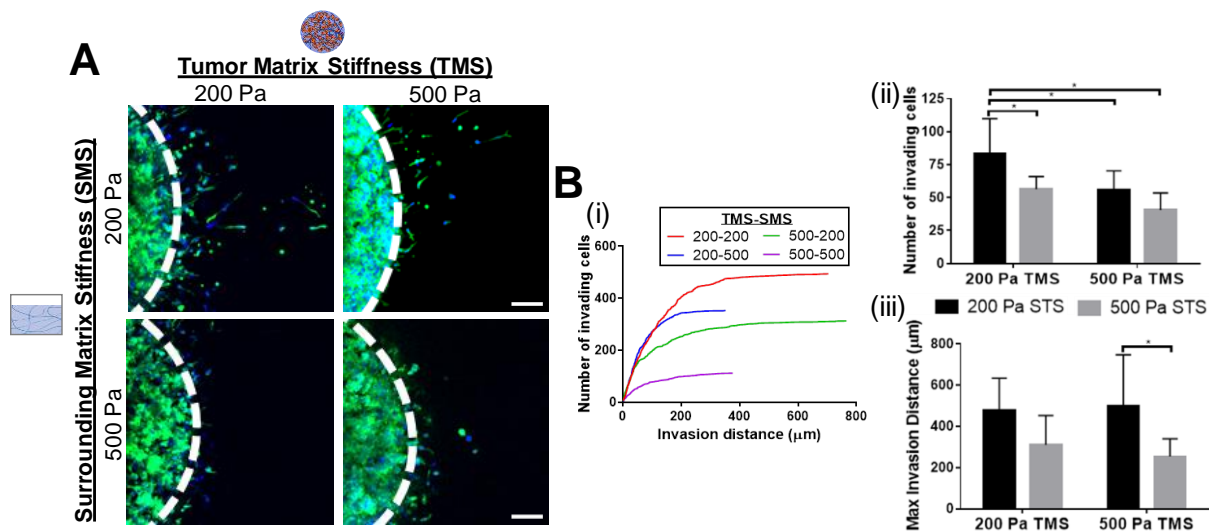
Figure 3-2 Surrounding matrix density (stiffness) determines tumor cell invasiveness.
(A) Tumor spheres prepared with 200 and 500 Pa oligomeric collagen were seeded with 1×10^7 cells/mL (Panc-1) and embedded within surrounding oligomeric matrices of 200 and 500 Pa and cultured for 5 days. Images represent maximum projections of 150 μm confocal z-stacks; green = actin, blue = nuclei, scale bar = 100 μm. (B) 3D tumor cell invasion from confocal images was quantified to create (i) a representative cumulative distribution plot and calculate (ii) average number of invading and (iii) cells maximum invasion distance. (bars represent mean ± std. dev., N=3, n=8-9; asterisks denote statistically different groups $p<0.05$)

those found *in vivo* and providing a much greater range of tunable matrix stiffness compared to monomeric type I collagen formulations [18,56]. Because of its type I collagen composition, Oligomer also serves as an accurate representation of the interstitial matrix laid down during desmoplasia and compared to Matrigel, has been shown to upregulate EMT of PDAC cells and increase invasiveness of glioblastoma spheroids [55,116].

In the present work, tumor-sphere and surrounding matrix fibril density were varied independently to optimize the matrix biophysical properties which yield the most invasion of PDAC cells in 5 days. For this optimization, Panc-1 cells were selected since they showed the greatest invasive potential compared to other PDAC lines in preliminary experiments (data not shown). The two different fibril densities applied in the present study correlated to matrix stiffness values of 200 and 500 Pa. As shown in Figure 3-2, increasing the fibril density (stiffness) of the surrounding tissue compartment from 200Pa to 500Pa drastically inhibited tumor cell invasiveness. However, increasing the fibril density (stiffness) of the tumor sphere only caused a slight decrease. More specifically, a cumulative distribution plot of invading cells, suggested that increasing the surrounding collagen fibril density decreased both the number of cells invading and the distance which they invade, while increasing the collagen fibril density of

the tumor sphere only decreased the number of cells invading (Figure 3-2Bi). Further quantification and statistical analysis revealed that the number of invading cells was indeed highest when both the surroundings and sphere were of low fibril density (200 Pa; Figure 3-2Bii). Interestingly, for maximum invasion distance, the only difference that was statistically significant was for increasing the surrounding fibril density of the denser (500 Pa) spheres (Figure 3-2Biii). Altogether based on these results, it was established that low density (200 Pa) Oligomer for both the sphere and the surroundings supported the greatest dynamic range of invasion within the given experimental time span (5 days) and that these conditions would be used for subsequent drug screening experiments.

3.3.3 3D metastasis model can support and distinguish various modes of tumor invasion which are dependent on initial cell phenotype

Tumor invasion *in-vivo* is a dynamic and plastic process in which cells use a variety of invasion strategies which depend on their genotype and phenotype, as well as the microenvironment in which they are invading [112,117]. While mechanisms that regulate these different modes of invasion are not fully understood, they are thought to rely on cellular characteristics such as cellular contractility, integrin expression, matrix metalloproteinase (MMP) expression, and EMT phenotype, as well as microenvironmental features including ECM composition and microstructure, soluble factor signaling, and stromal cell interactions [118,119]. Interestingly, most human pathology studies have indicated that collective invasion of tumor buds or strands is the most common form of invasion, but both *in-vivo* and *in-vitro* tumor models have observed single-cell migration modes, including mesenchymal and amoeboid invasion, in addition to collective invasion [120,121]. Because of these intricacies, it is important for *in-vitro* models to be able to distinguish various tumor invasion modes known to occur *in vivo*.

To verify that this 3D HT-HC metastasis model supports different invasive phenotypes, two PDAC cell lines, Panc-1 and BxPC-3, were chosen since based on published literature they have different invasive and phenotypic profiles. Panc-1 was derived from a poorly differentiated tumor with known metastases and is traditionally classified as mesenchymal, while BxPC-3 was derived from a moderately differentiated tumor with no observed metastases and is classified as epithelial [122]. Based on other published work, Panc-1 is also more contractile and mechanosensitive *in vitro* and is more metastatic *in vivo* compared to BxPC-3 [123,124]. Consistent with expectations based on these established cells, Panc-1 exclusively invaded as
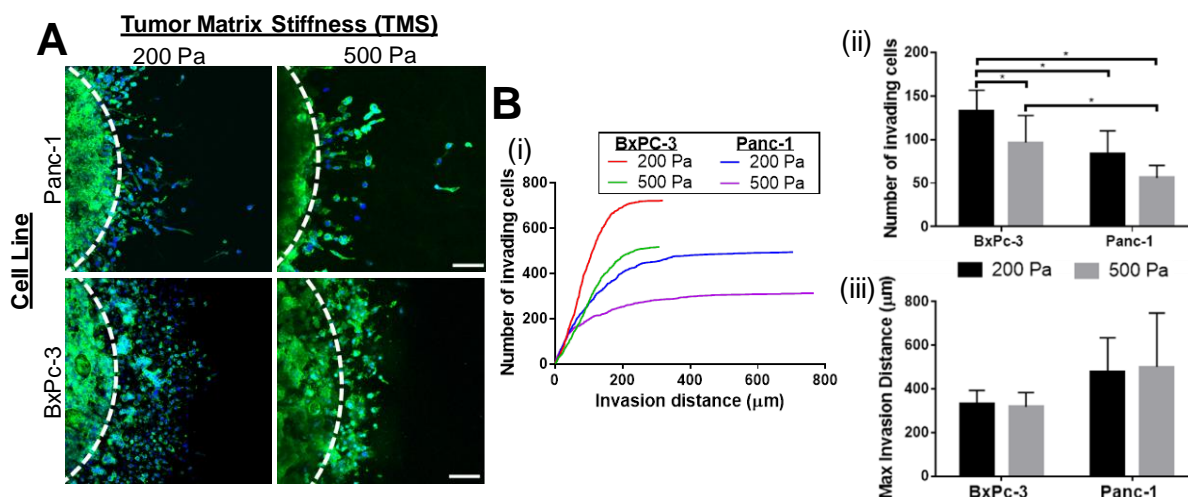
Figure 3-3 Both extent and mode of 3D invasion depend on initial cell phenotype.
Tumor spheres prepared with 200 and 500 Pa oligomeric collagen were seeded with 1×10^7 cells/mL (Panc-1 and BxPC-3) and embedded within surrounding oligomeric matrices of 200 Pa oligomeric collagen and cultured for 5 days. (A) Actin (green) and nuclear (blue) staining was performed to visualize and quantify invasion. Scale bars = 100 μm (B) Quantified 3D tumor cell invasion represented with (i) a representative cumulative distribution plot, (ii) average number of invading cells, and (iii) maximum invasion distance. (bars represent mean ± std. dev., N=3, n=8-9; asterisks denote statistically different groups p<0.05)

single cells, while BxPC-3 demonstrated collective-cell invasion in addition to some single-cell invasion (Figure 3-3A). Further, the morphology of invading Panc-1 cells were more spindle-shaped typical of mesenchymal invasion and those cells of BxPC-3 which were single cells appeared more rounded, indicating an amoeboid-like invasion. Upon quantification it was clear that significantly more BxPC-3 cells invaded than Panc-1, and although there was a slight difference in max invasion distance between the cell types, it was not statistically significant (Figure 3-3B). Interestingly, increased tumor matrix stiffness significantly hindered BxPC-3 invasive capacity but did not decrease Panc-1 invasiveness. This decrease in BxPC-3 invasiveness with increased fibril density is consistent with the modes of invasion observed, namely that dense ECM poses a more difficult barrier for collective invasion and amoeboid invasion (MMP-independent mode of invasion). Further, the mesenchymal invasion observed in Panc-1 has been observed in a genetically engineered mouse model with the same genetic mutations (p53 and KRAS) [125], whereas the collective invasion of BxPC-3 is reminiscent of human PDAC histopathology [120].

To further assess these different modes of invasion, immunostaining was performed on samples from the low stiffness condition. For Panc-1, the more mesenchymal line, there

appeared to be regions of E-cadherin staining in the center of sphere while vimentin was expressed throughout. Invading Panc-1 cells showed prominent vimentin with very distinct spindle-shaped morphology, again indicating mesenchymal cell invasion (Figure 3-4A). On the other hand, the majority of BxPC-3 cells, even some of those invading, expressed E-cadherin (Figure 3-4B). Minor vimentin expression was observed in the center of BxPC-3 spheres, but was more prominently expressed in those cells which were invading. Interestingly, most invading BxPC-3 cells expressed both E-cadherin and vimentin, especially those invading as single cells or the cells on the periphery of groups of invading cells. Further the collective invasion of BxPC-3 can be more clearly seen in these images, as budding protrusions of E-cadherin-positive cells are being led by vimentin-expressing "leader cells." Overall, these results verify and validate that our 3D metastasis model can distinguish pathophysiologically relevant modes of tumor cell invasion [120,125].
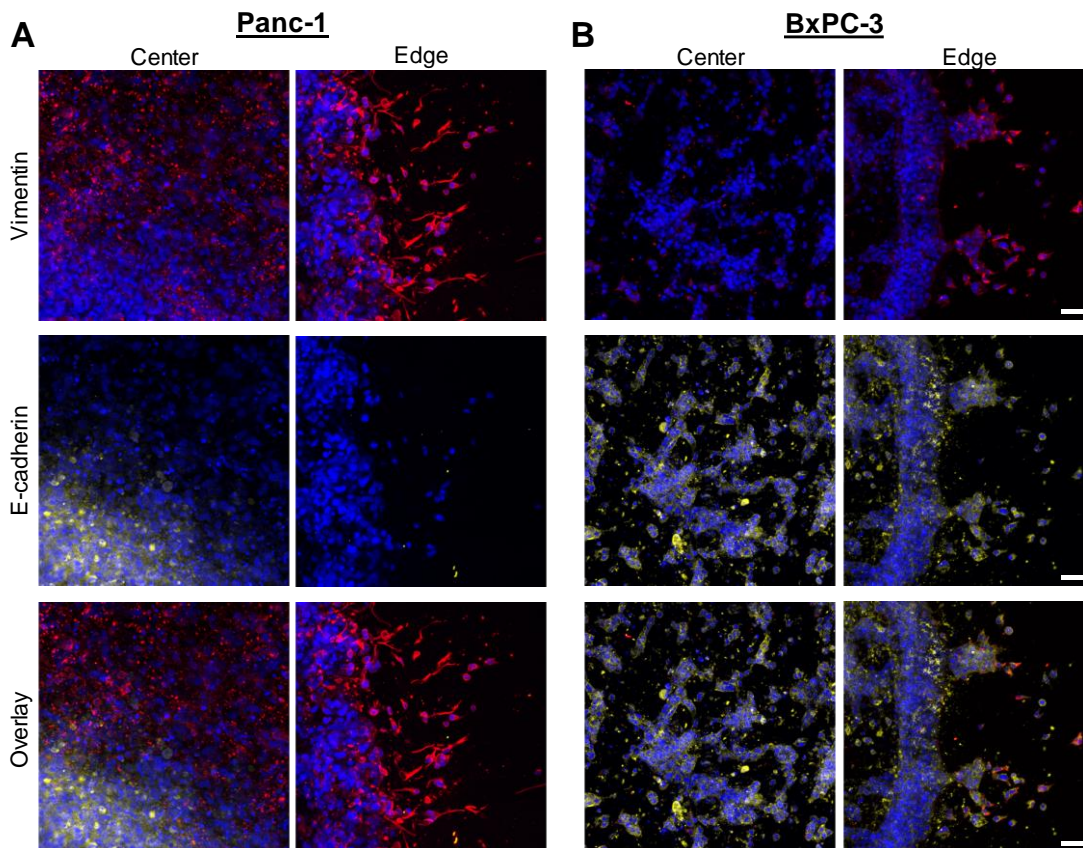
Figure 3-4 EMT status of invading cells depends on initial cell phenotype.
Tumor spheres prepared with 200 Pa oligomeric collagen were seeded with 1×10^7 cells/mL and embedded within surrounding oligomeric matrices of 200 Pa oligomeric collagen and cultured for 5 days. After fixation, constructs containing (A) Panc-1 and (B) BxPC-3 were frozen, cyrosectioned and stained for vimentin (red) and E-cadherin (yellow); nuclei were counterstained with Hoechst 33342 (blue). Images represent maximum projections of 20 μm confocal z-stacks; scale bar = 50 μm

3.3.4 PDAC heterogeneity and desmoplasia can be more accurately recreated with low-passage patient PDAC cells and CAFs

While immortalized cell lines serve as an important tool in cancer research and drug development, it is thought that translating to non-immortalized, low-passage patient derived lines better recreates tumor heterogeneity and preserves *in-vivo* phenotypes [22]. Additionally, CAFs represent an important component of tumor heterogeneity and desmoplasia and have been shown guide tumor invasion and modulate ECM remodeling that promotes metastasis [38,126,127]. To verify that our 3D HT-HC metastasis model is compatible with these cell populations, two low-passage patient-derived PDAC cell lines and a CAF line were incorporated into embedded tumor spheres. One of the PDAC lines was derived from a primary tumor (10.05) and the other from a metastatic lesion (Pa03C), and neither of these lines have been immortalized to better preserve their *in-vivo* phenotype [128]. Interesting, compared to the immortalized cells used above (Panc-1 and BxPC-3) these patient-derived cells do not appear very invasive by themselves but grow as tight clusters within the sphere, though Pa03C does some minor single cell invasion (Figure 3-5A). When CAFs were added to the sphere, however, the CAFs invade into the surroundings and significantly increase the invasiveness of the tumor cells (Figure 3-5B). Further, it appears
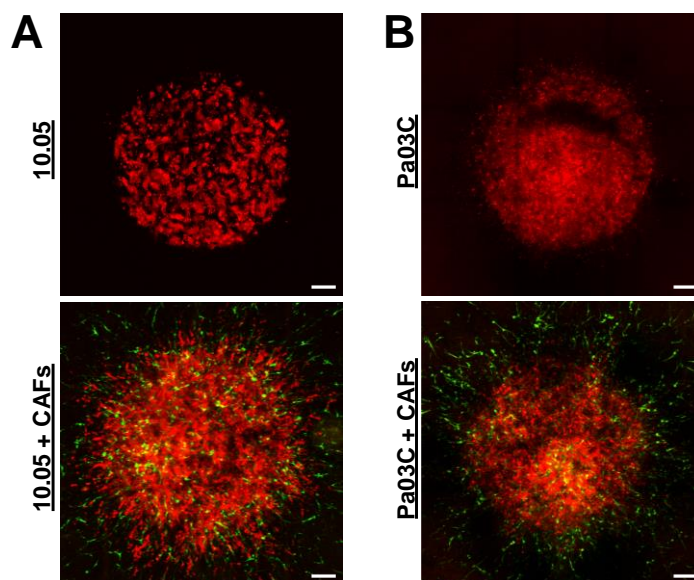
Figure 3-5 CAFs increase invasiveness of patient-derived tumor cells.
Tumor spheres prepared with 200 Pa oligomeric collagen were seeded with 1×10^7 cells/mL, embedded within 200 Pa oligomeric collagen, and cultured for 4 days. Spheres contained (A) 10.05 or (B) Pa03C cells without and with CAFs (1:1 tumor:CAF ratio). Images represent nine fields of view, each of which is a maximum projection of a 400 μm confocal z-stack. Red = tumor cells (TdTomato Red) and green = CAFs (Green Fluorescent Protein). Scale bars = 200 μm

that the CAFs more drastically effect 10.05 cells compared to Pa03C, which is consistent to the behavior of these cells in xenograft models (data not shown).

To more clearly define how these stromal cells guide tumor invasion and define the EMT status of tumor cells, immunostaining of *in-vitro* tissue sections was performed. As expected, tumor cells within the sphere have prominent E-cadherin and the CAFs stain strongly for vimentin (Figure 3-6). Very little overlap was seen between the TdTomato Red channel and the vimentin stain, indicating that vimentin expression was not prominent in cancer cells, even in those invading. Interesting it also appears that CAFs are physically guiding tumor cell invasion as groups of tumor cells can be seen in close proximity to CAFs as they invade into the surroundings. It is also notable that this interaction appears to be independent of EMT-status since tumor cells still appear to be expressing E-cadherin as they invade. Overall, these results confirm the compatibility of our model with more relevant cell populations and validate that CAFs play an important role in PDAC tumor invasion in our model, as is thought to be the case *in vivo* [127] .
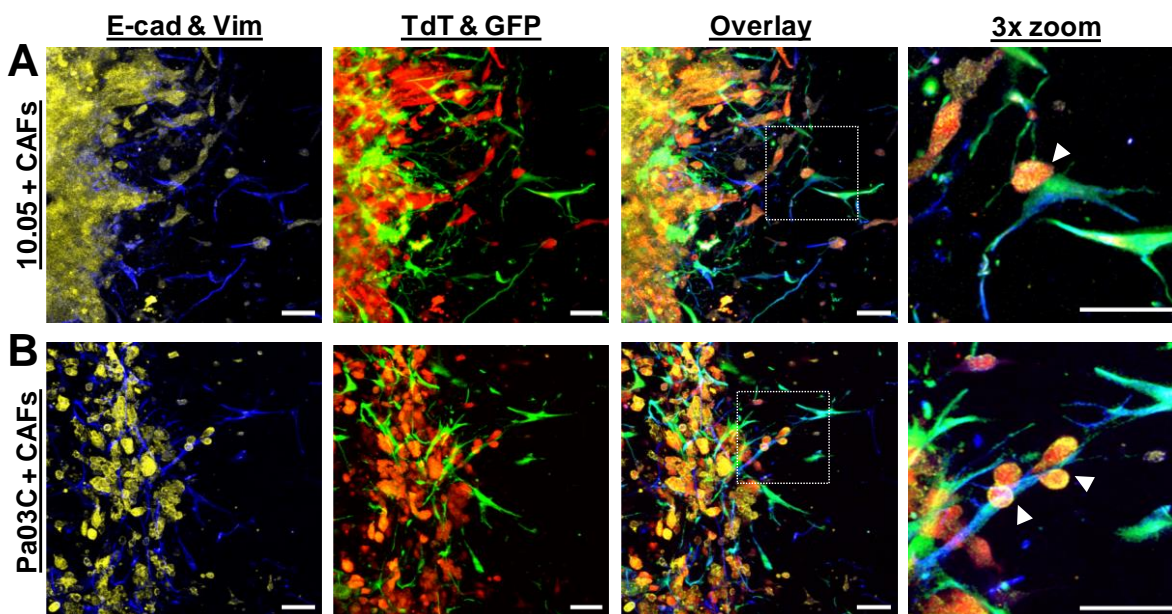
Figure 3-6 CAFs physically guide tumor cell invasion independent of EMT status.
Tumor spheres prepared with 200 Pa oligomeric collagen were seeded with 1×10^7 cells/mL, embedded within 200 Pa oligomeric collagen, and cultured for 4 days. Spheres contained (A) 10.05+CAFs or (B) Pa03C+CAFs (1:1 tumor:CAF ratio). Images represent cryosectioned samples which were stained for E-cadherin and vimentin. Each image is a maximum projection of a 20 μm confocal z-stack. Final panel represents a 3x zoom of the boxed region in the overlay panel. Arrowheads denote direct interaction between tumor cells and CAFs. Yellow = E-cadherin, Blue = vimentin, Red = tumor cells (TdTomato Red) and green = CAFs (Green Fluorescent Protein); Scale bars = 50 μm.

3.3.5   PDAC metastasis model is amenable to HT-HC drug screening

Designing 3D *in-vitro* models which balance the need for pathophysiologic relevance with the ability to scale-up to high-throughput systems, is one of the many challenges in developing translatable preclinical models [23]. Further, very few, if any, 3D *in-vitro* models apply multiplex, optical assays which can be visualized with automated imaging platforms. Therefore, to showcase the potential of this model as a tool for HT-HC drug screening, a proof of concept drug screen was performed to verify model reproducibly and to validate the ability to image this model using a high-throughput, automated microscope. Panc-1 and BxPC-3 cells were treated with a 10-point dilution of gemcitabine with STS and DMSO serving as positive and negative controls, respectively. Additionally, a multiplex assay was developed which used Hoechst 33342 to measure total cell numbers and invasion, Click-iT EdU to stain cells undergoing DNA synthesis (proliferation), and MitoTracker Red to evaluate metabolic activity. Automated confocal imaging was performed using an Opera Phenix High-Content Screening System; representative images of a single row of a well plate are shown in Figure 3-7A. These images demonstrate the reproducibility of model creation, showcasing its potential for high-throughput imaging and high-content analysis. Additionally, they reveal a sharp drop-off in cells' proliferative capacity when exposed to increasing doses of gemcitabine but only a gradual decrease in metabolic activity. Subsequent image analysis using Perkin Elmer's Harmony software enabled quantification of measurable outcomes for proliferation, metabolic activity, and invasion from which we generated dose response curves (Figure 3-7B) and associated IC50 and E_{max} values (Figure 3-7C). For both Panc-1 and BxPc-3, the IC50 for metabolic activity was significantly higher than the IC50 for proliferative capacity and invasion. Additionally, the metabolic activity IC50 value was significantly higher for BxPC-3 compared to that of Panc-1. For E_{max}, the value for proliferative capacity was lowest for both cell lines; for Panc-1, it was significantly lower than the E_{max} of metabolic activity while for BxPC-3 it was significantly lower than the E_{max} of invasion. In summary, these results validate the ability of this model to translate to HT-HC screening and demonstrate the rich datasets that can be created using multiplex assays such as the one used here.
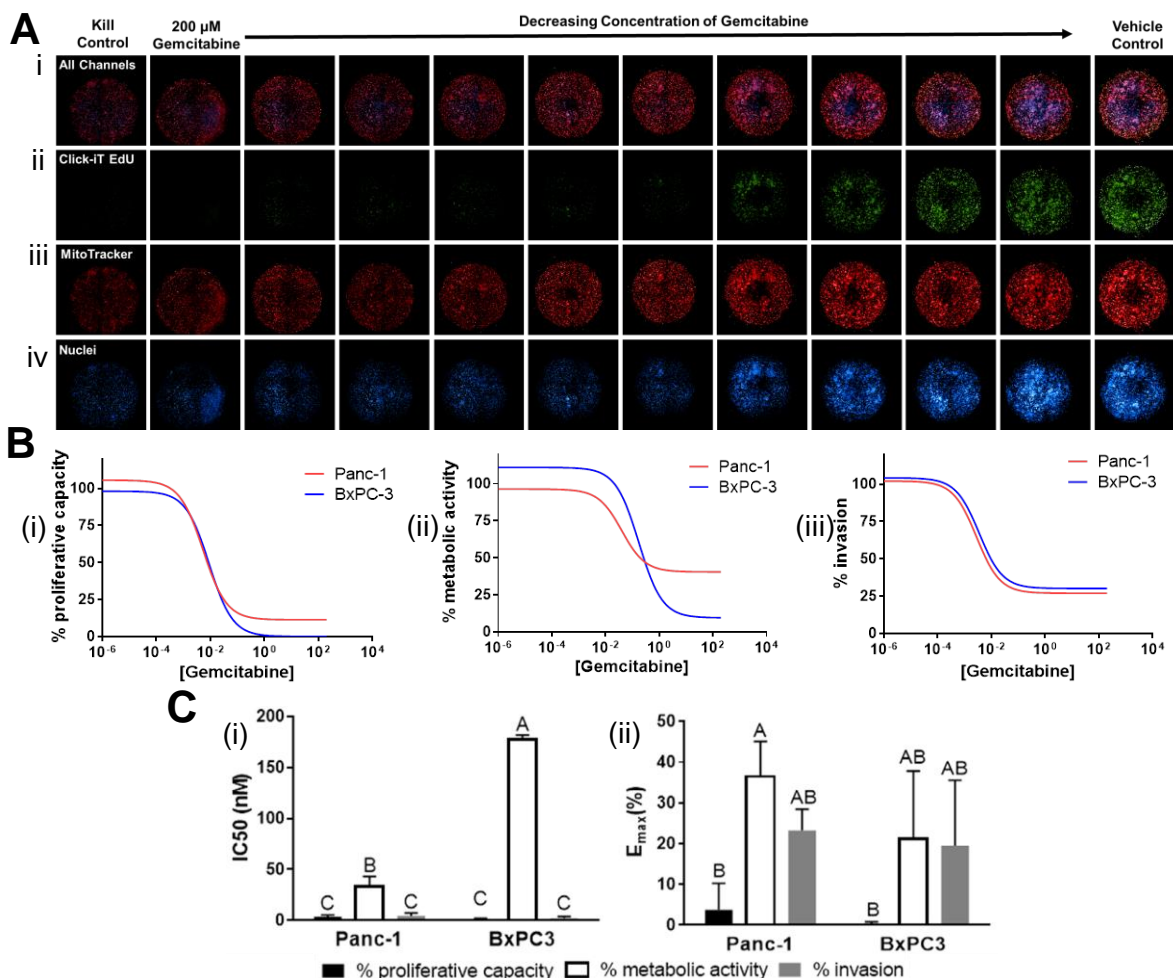
Figure 3-7 Proof of concept drug screen validates translation potential of HT-HC metastasis model
(A) Tumor spheres prepared with 200 Pa oligomeric collagen seeded with 1×10^7 cells/mL (Panc-1) were embedded within surrounding matrices of oligomeric collagen (200 Pa) and treated with serial dilutions of gemcitabine, 20 μM STS (kill control), and 1% DMSO (vehicle control) for four days. Images were obtained using an Opera Phenix and represent a maximum projection of a 500 μm z-stack. (i) overlay of all channels (ii) Click-it Edu 488 staining proliferating cells, (iii) Mitotracker Red staining active mitochondria, and (iv) Hoechst 33342 staining nuclei. (B) Representative dose response curves for (i) proliferative capacity, (ii) metabolic activity, and (iii) invasion for both Panc-1 and BxPc-3. (C) (i) IC50 and (ii) E_{max} values were calculated from dose response curves from independent experiments (N=3) and compared Tukey-adjusted multiple comparisons. Letters over bars (mean ± SD) denote statistically different groups (p<0.05).

3.4   Discussion
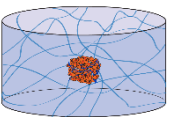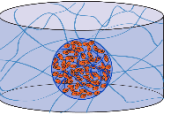
Since the efficiency of molecular target-based screening—the current industry standard for drug development—has recently come into question, phenotypic screening approaches are now being explored with renewed interest in order to improve the efficiency of drug development and reduce clinical trial attrition rates [7,9]. Because of this, the need for models

which more accurately recreate specific disease phenotypes is more prevalent than ever [10,22]. Metastatic phenotypes are especially in need of more predictive preclinical models since the metastatic process is a complex series of steps with incompletely understood mechanisms, making target-based screening especially difficult [25,129]. Additionally, there a few models which are able to balance complexity and accurate recreation of metastatic phenotypes with high-throughput capacity [23]. Table 3-1 compares a few of the most common tumor invasion models with specific regard to criteria developed from several review articles about pathophysiologic relevance and practical considerations [10,22–24].

Scratch or exclusion zone assays and transwell invasion models both involve seeding tumor cells on a planar surface and measuring the migration or invasion of cells in constrained non-physiologically relevant geometries. Although these models are amenable to more high-throughput analysis and are fairly reproducible, they do not accurately recreate the tumor interstitium and they offer very little user control to enable customization and standardization [29,108]. Further, while ECM coatings of Matrigel, type I collagen or fibronectin can be applied to these surfaces, these thin layers of ECM proteins do not recreate the complex 3D fibril matrix through which cells invade *in vivo* [99,112]. 3D spheroid invasion assays are often considered to be a more relevant tumor invasion model since the 3D architecture of spheroids themselves as well as their embedment within 3D matrices is thought to more accurately recreate the tumor microenvironment [108]. Unfortunately, however spheroid-based models do not meet several of important practical considerations (Table 3-1). Since spheroids rely on the self-aggregation of cells they are difficult to customize and standardize, their creation is time-consuming, and they are often cited as having reproducibility issues [21]. While some work has been done to develop more reproducible spheroids or larger tumor spheres [130–132], there remains solution to reproducibly embed spheroids or spheres within the wells of standard well plates.

Thus, the goal of this work was to develop and validate a novel HT-HC metastasis model that was pathophysiologically relevant as well as practical to implement and feasible to translate to HT-HC drug screening. This model builds on previous work using type I collagen Oligomer to create cell-dense tissue spheres embedded within a 3D collagen-fibril matrix to create adjacent and independently tunable tissue compartments [114]. The use of Oligomer which is a standardized ECM material with a broad range of tunability [18], along with this unique model design provide a high level of user. This user control provides the ability to customize and

Table 3-1 Comparison of common *in-vitro* metastasis models

Criteria for relevant and translatable in vitro models		Scratch or exclusion zone	Transwell invasion	3D spheroid invasion	3D metastasis model
	model geometry				
		2D	Semi-3D	Embedded 3D	Embedded 3D
Relevance of disease model	ECM microstructure	None usually present	Thin layer of Matrigel or fibril collagen	Collagen fibril matrix	Collagen fibril matrix
	Can incorporate stromal cell populations?	No	Yes	Yes	Yes
relevance of stimuli and phenotype	relevant metastatic phenotypes?	No	No	Yes	Yes
	Is stimuli natural or artificial?	Artificial	Artificial	Natural	Natural
Relation between assay and clinical outcomes	Metastasis	Poor: 2D migration/wound closure	Poor: Migration through artificial confined pores	Good: Invasion through 3D fibril matrix	Good: Invasion through 3D fibril matrix
	Tumor growth and progression	None	None	None	Good: Direct measures of proliferation and metabolic activity
Fast, simple, reproducible model creation	Model creation takes < 1 hr	+	+	-	+
	uses minimal specialized equipment	+	+	-	+
	reproducible creation of model	+	+	-	+
amenable to scale-up for high throughput screening	Uses standard well-plates	+	+	-	+
	Able to image with automated systems	+	-	-	+
	quantify relevant phenotypic outcomes?	-	-	-	+
Ability for customization and standardization	User control of tumor properties	Minor	Minor	Minor	High
	User control of surroundings	none	Minor	Moderate	High

Pathophysiologic Relevance (rows: Relevance of disease model; relevance of stimuli and phenotype; Relation between assay and clinical outcomes)

Translational Considerations (rows: Fast, simple, reproducible model creation; amenable to scale-up for high throughput screening; Ability for customization and standardization)

optimize both cellular and ECM properties to apply this model to other cancer types and diseases, and enables standardization of model setup to translate it as screening platform. Further, the development and use of a custom fabrication platform to facilitate model creation, provides rapid model setup and reproducible sphere creation and embedment—two necessary characteristics for high-throughput use. Finally, the present work has validated that this model can distinguish various phenotype-dependent modes of invasion and is able to translate to HT-HC imaging and analysis.

 To our knowledge, there are few published examples of tumor invasion models which achieve a balance between relevance and practicality, as the HT-HC metastasis model does. One such model with similar goals to ours did not use standard well plates but involved microfabrication of a custom device to create and subsequently embed spheroids [133]. Since this model still relied on the self-aggregation of cells to form spheroids, model creation appeared to be a complicated, time-consuming process (3-4 days) which would not be amenable to automation and it does not appear that their custom device would interface with standard automated imaging systems. Another model followed a similar approach to the present work, but instead of embedding preformed spheres within a 3D matrix, it involved creating cell-dense collagen spheres in hemispherical pits in the bottom of the wells of a customized 96-well plate followed by overlaying the spheres with collagen [134]. While this strategy did allow them to create a cell-dense sphere in the center of each well, since it was in contact with the bottom of the well and they did not validate that cells were invading into the overlaying 3D matrix, it is likely that most of the "invasion" that they observed was really migration on the bottom surface of the well plate since cells will preferentially migrate along paths of least resistance [135]. Additionally, because they were using a monomeric collagen formulation and were not fully embedding their spheres, they had to exogenously crosslink the matrix with dialdehyde dextran to prevent sphere contraction. Based on this, we believe that our custom fabrication platform is the first of its kind that allows for the rapid, reproducible creation of tumor spheres and their subsequent, full 3D embedment in the wells of a standard 96-well plate.

 The HT-HC metastasis model developed in this work not only provides a solution for some of the practical considerations in Table 1 but it also provides a pathophysiologically relevant microenvironment which can distinguish various modes of tumor invasion based on cell phenotype. The branched fibril architecture of the Oligomer matrices used here accurately

recreates the interstitial tissue laid down in desmoplasia, creating a relevant barrier to PDAC cell invasion [32]. The trend of decreased invasiveness with increased surrounding stiffness correlates with other 3D embedment models and genetically engineered mouse models, but is opposite of durotaxis, the preferential migration of cells in 2D from soft to stiff substrates [53,54,78,79,136]. As with other phenotypic behaviors, 3D fibril matrices, *in vitro* and *in vivo,* provide different geometric and spatial constraints to cell invasion and migration than 2D culture, and therefore often lead to different trends [53,99]. Further, in the present work, the more mesenchymal PDAC cells, Panc-1, exclusively invaded as elongated, spindle-shaped single cells with prominent vimentin expression, all indicating a mesenchymal mode of invasion. Notably, this mode of invasion has been observed with intravital imaging of a genetically engineered mouse model of PDAC with the same mutations as Panc-1 (KRAS and p53) [125]. On the other hand, the epithelial line, BxPC-3, demonstrated both single-cell, amoeboid-like invasion and collective invasion with some partial EMT in subpopulations of invading cells. These observations are reminiscent of clinical human tumor samples, in which only subpopulations of cells are noted as having undergone EMT and collective invasion and tumor budding have been noted to be more prominent that single cell invasion [104,120]. Overall, these results confirm this model's capacity to support and distinguish relevant invasive phenotypes by accurately recreating the 3D fibril architecture through which cells invade *in vivo*.

       To both increase and further demonstrate the pathophysiologic relevance of this metastasis model, low-passage patient derived lines and CAFs were incorporated in the embedded tumor spheres. From this, CAFs were found to significantly enhance, and even be necessary for invasion of these PDAC cells in our model. These results align with how invasion is thought to occur in PDAC in vivo, with CAFs playing a prominent role [137,127]. Specifically, others have shown, both *in vivo* and *in vitro*, that in addition to soluble factor signaling, CAFs physically interact with tumor cells too guide their invasion. [137,138]. Though this phenomenon was not explored more fully in the present work, it appeared that CAFs and tumor cells are indeed physically interacting as they invade (Figure 3-6). Further work would be needed to fully explore these interactions and different modes of invasion, but these results validate this model's ability to support relevant phenotype-dependent modes of invasion and demonstrate the potential of this model for systematic studies to further elucidate the mechanism at play in the various tumor invasion strategies.

Finally, and most importantly, we validated this model's amenability to HT-HC screening by performing a proof of concept drug screen with an automated imaging system and multiparametric analysis. The ability to image this model using an automated system such as the Opera Phenix High Content Screening System (Perkin Elmer) verifies our design's ability to reproducibly create and embed tumor spheres within the well of a standard well plate. While others have created microfabricated platforms and custom-well plates for similar purposes [133,134,139], our design interfaces with standard well plates making it easy to scale-up and translate to other labs. Further, unlike traditional cytotoxicity assays which only use metabolic activity to measure cell viability, quantifying multiple phenotypic parameters as we have done here, opens the door for advanced mechanistic understanding of how drugs affect tumor cells. In this proof of concept screen, gemcitabine appears to be effective at hindering proliferation but is not able to fully kill cells or stop invasion. Additionally, since proliferative capacity and invasion have similar IC50 values this may suggest that a significant portion of invasion is driven by proliferation however since they have different E_{max} values, there are some invading cells not proliferating which are unaffected by gemcitabine. These observations would need to be validated with future mechanistic studies, but these results showcase both the potential of this model to be used in high-throughput, high-content screening and the rich data that can be generated using multiplex assays such as the one used here. In the future, these *in-vitro* measures of proliferative capacity, metabolic activity, and invasion can be correlated with *in vivo* or clinical evaluations of tumor growth, metabolic tracers, and metastatic spread to validate that this model can serve as a predictive tool of *in vivo* drug response and clinical outcomes.

3.5   Conclusion

With the ever-rising demand for more pathophysiologically relevant tumor models, it is important to also consider how these advanced models will translate and integrate with existing workflows in the pharmaceutical industry. In this work, we aimed to develop a model system which accurately recreated specific features of the human disease while maintaining the ability to quantify relevant outcomes using high-throughput imaging systems. Specifically, our novel 3D HT-HC metastasis model recreates PDAC desmoplasia and is able to quantify true 3D invasion and distinguish various invasion strategies. Additionally, it allows for user customization and standardization, model creation is simple, rapid and reproducible, and finally, it is amenable to

automated imaging and analysis to enable high-throughput, high content screening. Further validation of this model that remains to be completed is screening with compounds of various mechanisms of action to validate our multiplex assay and validation of the model's predictive power by comparison to *in vivo* models. Once complete, we believe that this 3D metastasis model has great potential to serve as powerful tool for preclinical drug development to identify new therapies for PDAC and decrease the high attrition rates of cancer clinical trials.

In addition to this model's potential as a HT-HC drug screening platform, there many other future applications for which this model can be used. Because of its high degree of user customization over both the composition and biophysical properties of both tissue compartments, this metastasis model would be a powerful tool for systematic study of mechanobiology-related mechanisms which are thought to be highly important in tumor invasion and metastasis [35,140]. Further, because of the size and robust nature of the embedded spheres, this model could also fill a gap by being used as an *in-vitro* platform to test radiation or ablative therapies since traditional spheroids are not large enough to do this [23]. Finally, this phenotypic model of metastasis could be used as a high-content "culture and sensitivity" screen for personalized medicine. Using this model to perform medium throughput screening of potential therapies on tumor cells derived from a patient biopsy could provide phenotypic outcomes (e.g. invasion, metabolic activity, and proliferation) to compliment the genotyping, already performed on these samples. In this way, physicians would be able to integrate genotypic and phenotypic information to decide on the best course of therapy for a given patient. In summary, the model developed in this work has great potential for HT-HC drug development, as well as mechanobiology and personalized medicine.
.

4. FURTHER MODEL VALIDATION, FUTURE WORK AND CONCLUSIONS

4.1 Introduction

The medical device development process has served as the framework for the model development work performed in this thesis. This process involves the following steps: understanding user needs, defining design inputs, iterative design and testing, design verification, and finally design validation. Within this context, Chapter 1 introduced some of the shortcomings in the anti-cancer drug development process and defined important user needs and design criteria for preclinical phenotypic screening models. Chapter 2 more specifically defined important 3D in vitro model design parameters, namely 3D collagen fibril architecture and model geometry, and established oligomeric type I collagen as a powerful tool for model development. Finally, Chapter 3 described the development of a novel 3D high-throughput, high content (HT-HC) metastasis model which accurately recreates PDAC desmoplasia and is able to scale-up for HT-HC drug development. Additionally, several aspects of design verification and validation were performed in Chapter 3. Design verification included demonstrating this model's capacity for rapid, reproducible experimental set-up, its ability to quantify 3D invasion, and its potential for customization and standardization. Validation in Chapter 3 included confirming this model's ability to distinguish various metastatic phenotypes, its compatibility with relevant cell populations to recreate PDAC heterogeneity and desmoplasia, and its ability to translate to HT-HC drug screening. To more fully validate this model, the following sections outline some proposed next steps and present preliminary data for the proposed validation work. Finally, the future potential of this work and overall conclusions from this thesis are discussed.

4.2 Proposed Next Steps of Model Validation

Since we have verified several aspects of our design and validated that our 3D metastasis model is capable of translating to HT-HC drug discovery (Chapter 3), the next steps of development includes validation of pathophysiologic relevance and predictive power. It is often assumed that 3D *in-vitro* models are more pathophysiologically relevant and more predictive of *in-vivo* behavior than traditional 2D culture, however these assumptions are rarely validated [22–

24]. To fill this gap, proposed model validation includes the following two key steps. First, to validate that the 3D HT-HC metastasis model accurately recreates important aspects of human PDAC, histological and immunohistological comparisons to xenograft and human tumor samples will be performed. Second, comparative drug treatment studies with gemcitabine and a novel drug target will be performed to validate if outcomes from this *in-vitro* model align with outcomes from an *in-vivo* model.

This validation work will be performed collaboratively with the labs of Melissa Fishel and Mark Kelley at Indiana University School of Medicine. The Fishel lab is focused on identification and preclinical validation of novel anti-cancer therapies using both *in-vivo* and 3D *in-vitro* tumor models, while Kelley is focused on translating novel therapies to the clinic. This collaborative effort has already begun as they provided the low-passage patient derived lines and CAFs used in Chapter 3. For the validation of our model we will also be focusing on one of the novel drug targets in their lab—reduction-oxidation factor-1 (Ref-1). Ref-1 is an important redox regulator of specific transcription factors known to be important in tumor progression and metastasis, namely STAT3, HIF-1α, and NF-κB [141]. Additionally, they have shown that this protein is highly upregulated in human PDAC tumors (unpublished data) and has great potential as a clinical drug target. In fact, one of their potential therapies that targets Ref-1, APX3330, has been approved by the FDA as an Investigation New Drug (IND) and will be starting in clinical trials in early 2018. This protein (Ref-1) and novel therapy (APX3330) will serve as a specific application for our final model validation. The following preliminary work has already begun and is briefly described below: i) initial attempts at histological evaluation of our in vitro model, ii) immunostaining to validate relevant protein expression patterns, and iii) a pilot drug screen.

4.2.1   Histological evaluation

Unlike many 3D *in-vitro* models such as those based on spheroids and Matrigel which are difficult to post-process after fixation, the HT-HC metastasis model supports *in-situ* crysectioning, as demonstrated with immunostaining results from Chapter 3. To provide a clinically translatable and comparable outcome, initial work has been performed with traditional hematoxylin and eosin (H&E) staining. However, since the collagen density in this model is low compared to *in-vivo* tissue, eosin was not well retained (data not shown). To provide better staining of the cyrosectioned samples, another common histological stain, Sirius Red, was used;

this dye stains type I collagen fibers and is commonly used to evaluate collagen networks in tissues [142]. Briefly, after fixation, freezing and crysoectioning (60 μm sections), slides were stained with Sirius Red (70 mM in 1% acetic acid) and Ricca Triple Strength hematoxylin. Slides were rinsed with increasing concentrations of ethanol, fully dehydrated with xylene, and mounted with Paramount.

Preliminary images of Sirius Red and hematoxylin stained samples are summarized in Figure 4-1. These images show that without CAFs present, 10.05 cells grew as tightly grouped structures reminiscent of neoplastic ducts while Pa03C tended to remain more as single cells with only some clustering. For both cell types, there was essentially no invasion into the surrounding tissue when CAFs are not present. However, when CAFs were added to the sphere, they appear to guide invasion of the tumor cells into the surrounding environment. Additionally, they appear to drastically increase proliferation of tumor cells since the center of these sphere appear so dense that it becomes difficult to distinguish individual cells or cell clusters. These two outcomes correlate with the role that CAFs are said to play *in vivo*, where they increase tumor proliferation and metastasis [127,143]. Additionally, these images represent the potential of our model to be histologically analyzed, though further optimization of the sectioning and staining
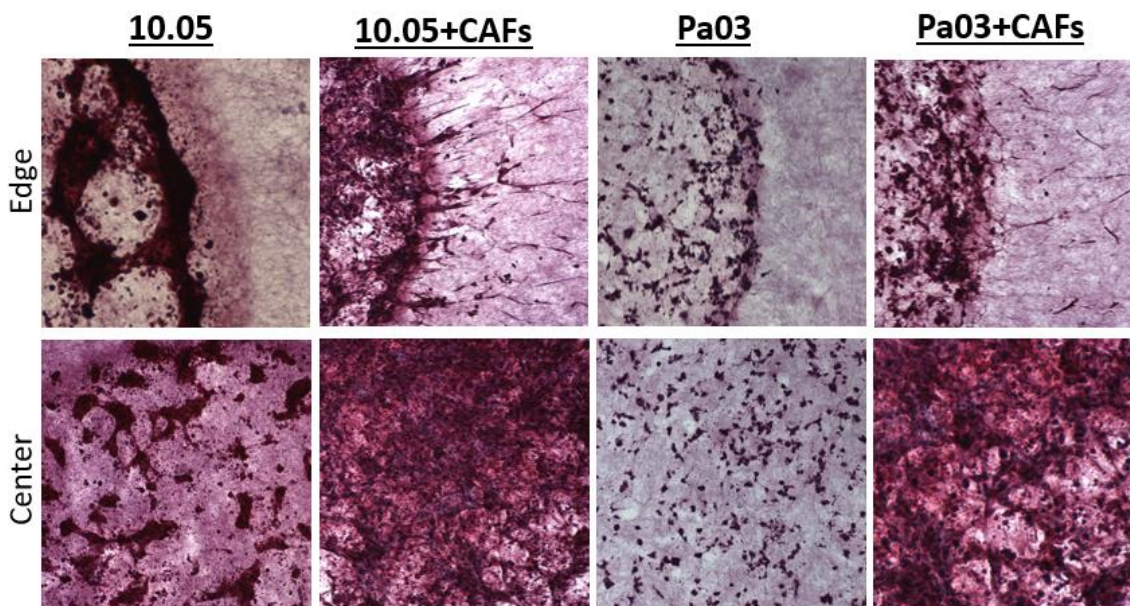

Figure 4-1 Preliminary images of *in-vitro* metastasis model histology.
Tumor spheres (200 Pa Oligomer) composed of patient derived cell lines with or without CAFs were embedded within 200 Pa Oligomer and cultured for 4 days. Constructs were fixed, frozen, and crysectioned followed by staining with Sirius and hematoxylin. Images were taken in the center and at the edge of each sphere.

technique is still needed to obtain higher quality images for comparison to *in-vivo* samples. Paraffin embedment and sectioning will be also explored to achieve better resolution and more comparable images to those of *in-vivo* tissue sections. Once complete, the comparison of the HT-HC metastasis model to human tumor samples and xenograft tumor samples will validate that this model accurately recreates PDAC histoarchitecture.

4.2.2   Proposed immunofluorescent comparisons

Another step of model validation is confirming the protein expression and distribution within this *in-vitro* model correlates with what is known about PDAC tumors *in vivo*. The two key proteins that have been evaluated to date are Ref-1 and Ki-67. As mentioned above Ref-1 is an important regulator of transcription factor activity and is upregulated in human PDAC [141]. Ki-67 is a commonly-used clinical biomarker of cell proliferation as it is expressed in all cells which are actively cycling but not expressed in quiescent cells [144]. Additionally, increased Ki-67 staining in clinical samples has been correlated with poor prognosis in PDAC [145]. By staining and visualizing the distribution of these two proteins, comparisons to published literature about human PDAC tumors can be made. Immunostaining was performed as described previously (Chapter 3). Cryosectioned samples were permeabilized with 0.1% Triton X-100 and blocked with 1% bovine serum albumin before overnight incubation at 4 °C with primary rabbit antibodies for Ref-1 and Ki-67. Anti-rabbit Alexa Fluor 633 secondary antibody was then applied followed by nuclear counterstaining with Hoechst 33342.

Preliminary images from spheres composed of 10.05 cells without CAFs are shown in Figure 4-2. From these images, it appears that Ref-1 is expressed in almost all tumor cells throughout the tumor sphere, regardless of location. This is consistent with findings from the Fishel lab that Ref-1 is prominent throughout human PDAC tumors (unpublished data). Ki-67, on the other hand, appears to be more prominent in cells around the edges of the sphere than in the center which correlates to the different biological zones that are thought to exist in tumors *in vivo*, namely a proliferative rim and a quiescent or necrotic core [110]. To further validate and extend these conclusions, immunostaining of both low-passage patient derived PDAC cells (10.05 and Pa03C) with and without CAFs will be performed. Additionally, comparison to immunohistochemistry of human tumors samples will be performed to validate
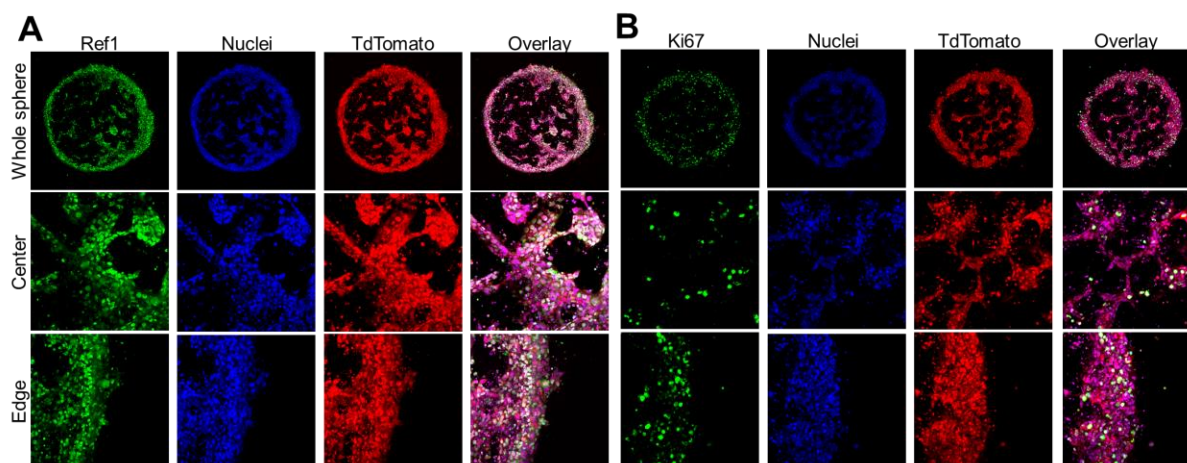
Figure 4-2 Preliminary immunostaining images.
Tumor spheres (200 Pa Oligomer) composed of 10.05 patient derived cell lines were embedded within 200 Pa Oligomer and cultured for 4 days. Constructs were fixed, frozen, and crysectioned followed by immunostaining for (A) Ref-1 and (B) Ki-67. Images represent maximum projections of 20 μm confocal z-stacks. Whole sphere images represent 16 fields of view stitched together. (Green = (A) Ref-1, (B) Ki-67; Blue = nuclei; Red = TdTomato Red)

pathophysiologically relevant expression profiles. Other protein biomarkers of interest that may be included in these comparisons include markers for ECM proteins (e.g. hyaluronic acid, fibronectin), hypoxia (e.g. carbonic anhydrase-9), and cancer stem cells (e.g. CD24, CD44) [76,128,146]. By performing this proposed analysis and comparison of protein expression patterns, the pathophysiologic relevance of our 3D HT-HC metastasis model will be validated.

4.2.3 Pilot drug screen for comparative drug treatment studies

Finally, validation of this model's predictive power should be performed to highlight its potential to replace or reduce the use of animal models in preclinical drug development. To accomplish this, it is proposed that *in-vitro* to *in-vivo* comparative drug treatment studies with gemcitabine and APX3330 be performed. Toward this end, a pilot drug screen comparing gemcitabine and APX3330 has been performed with the low-passage patient cells and CAFs. Briefly, tumor spheres with 10.05 +CAFs and Pa03C+CAFs were created and emdedded using the fabrication platform, as described previously (Chapter 3). After 24 hours and every 24 hours thereafter, drug treatments of both drugs were applied as a standard 10-point dilution starting with a starting concentration of 200 μM. Experiments were fixed after 4 days (96 hour total experiment time), imaged on the Opera Phenix High-Content Screening System, and analyzed using the accompanying Harmony software. Since the low passage-patient derived lines and

CAFs stably express TdTomato Red and green fluorescent protein, respectively, no further staining was performed for this proof of concept screen and the fluorescent intensity of these two markers were used to assess viability [128]. To quantify the fluorescent intensity of each channel, first, a region of interest was created by thresholding each respective channel to exclude background, followed by summing the intensity within the created region. The value for each well was then normalized using the following equation: $Relative\ Fluorescence = (I_n - I_{STS})/(I_{DMSO} - I_{STS})$. I_n represents the value of the *nth* dilution. I_{STS} and I_{DMSO} represent values from kill control and vehicle control, respectively.

Figure 4-3 summarizes the data obtained from this pilot drug screen. Based on the images, there appears to be little discernable change across the dilution off either drug except for the highest concentration of APX3330 which appears to inhibit invasion and to have slightly lower signal intensity. Clearly none of the drug dilutions are achieving the same level of kill as the STS control, in which there is only slight fluorescence remaining from the tumor cells (TdTomato red). Quantification of these images provides further insight to the cellular response to these two drugs (Figure 4-3B,C). Notably, for each set of conditions there is a slight downward trend as drug concentration increases (right to left), though only the high concentration of APX3330 on Pa03C+CAFs reached a similar fluorescent intensity level to the STS kill control (relative fluorescence of 0). Otherwise, relative fluorescence of tumor cells remained above approximately 0.2 or 20% of the DMSO control. For CAFs, the relative fluorescence remained above 0.3, with most values being above 0.5, indicating that the drugs did not significantly kill the CAFs. While it is difficult to make more significant conclusions from this preliminary data we hypothesize that since this model accurately recreates PDAC desmoplasia and heterogeneity, we will also recapitulate this cancer's resistance to gemcitabine treatment [147]. From this initial data it does appear to be the case since even when exposed to 200 μM gemcitabine, the relative fluorescence of Pa03C and 10.05 cells remains quite high (0.23 and 0.45, respectively). While this remains to be validated with further experiments, this conclusions would be significant since a recent review claimed that no in vitro PDAC models to date have truly recreated PDAC's clinical resistance to therapy [24].

Future work for this aspect of model validation includes further refinement of imaging and analysis techniques, as well as *in-vitro* to *in-vivo* comparison studies. While including two distinct cell populations (tumor cells and CAFs) does increase the relevance of this model, it also

makes quantitative analysis more challenging. The use of fluorescently-labeled cells, as done here aids in this somewhat, but limits the analysis to measures simply based on the fluorescent intensity of these cells. To enable more high-content analysis, further refinement of imaging and image analysis techniques will be explored, to at the very least include measures of viability and invasion. Additionally, results from *in-vitro* drug dosing studies will be compared to analogous
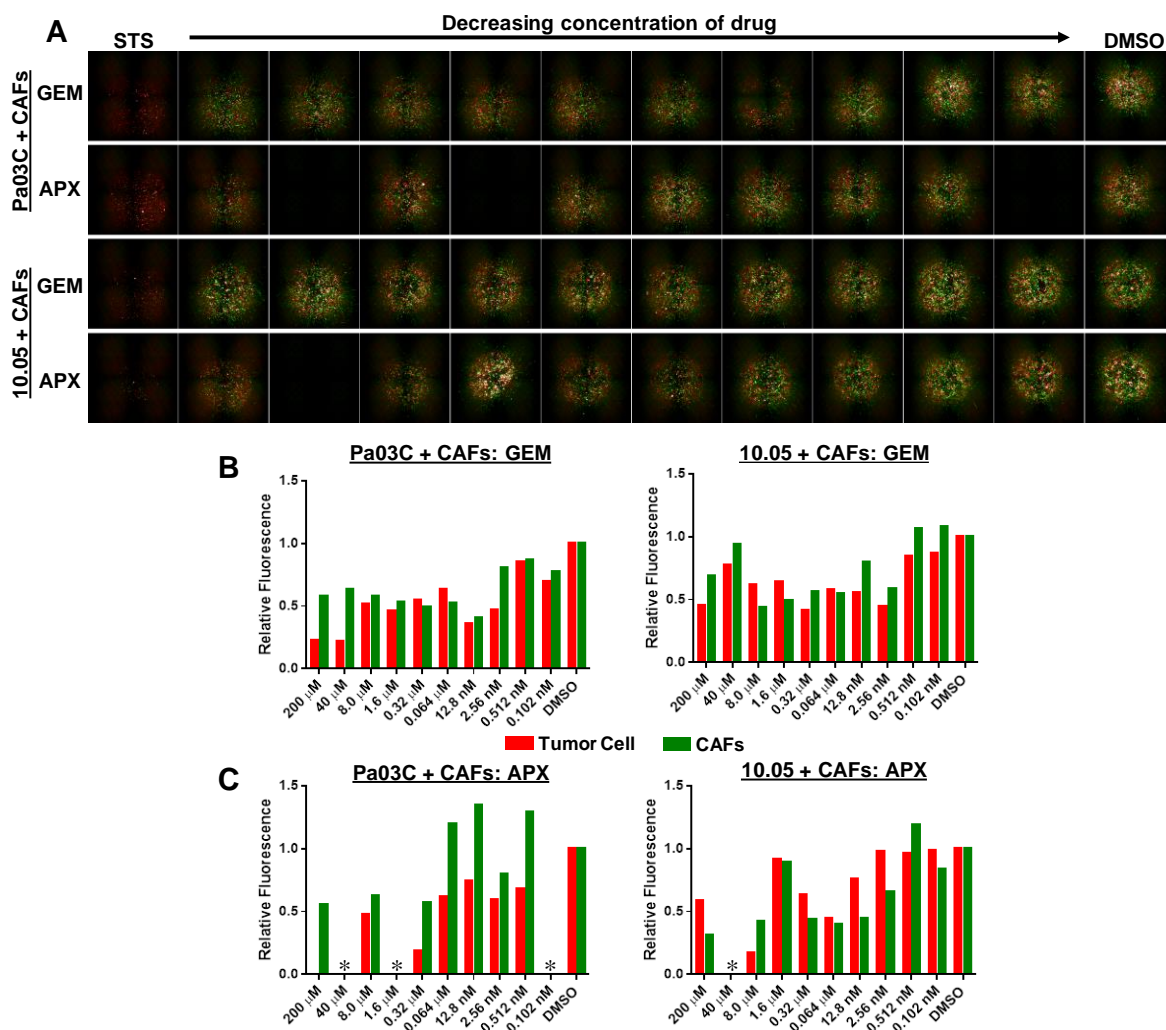
Figure 4-3 Pilot drug screen with APX3330 and gemcitabine.
Tumor spheres (200 Pa Oligomer) composed of patient derived cell lines with or without CAFs were embedded within 200 Pa Oligomer and cultured for 4 days. Drugs dilutions (gemcitabine=GEM, APX3330=APX), as well as 10 μM STS and 1% DMSO controls, were applied every day. (A) Images were obtained using Opera Phenix High-Content Screening System and represent 4 fields of view, each of which is a maximum projection of a 500 μm z-stack; tumor cells = red (TdTomato Red), CAFs= green (Green Fluorescent Protein). For both (B) gemcitabine and (C) APX3330 dosing, quantitative image analysis was performed to calculate the relative fluorescent intensity of both tumor cells (red bars) and CAFs (green bars). (Note: In (A), black images in the 3rd, 5th, and 11th column represent wells in which 3D constructs were accidently aspirated during post-processing. In (C) the missing data for these columns are noted with asterisks (*))

in-vivo drug treatment experiments with xenograft mouse models using the same cells. By performing these comparisons with the same cell populations, parallels will be drawn based on cellular phenotype and the influence of CAFs in the two models, in addition to the potency and efficacy of the two drugs tested. Specifically, *in-vivo* tumor growth and metastatic spread will be compared to measures of viability and invasiveness *in vitro.* In summary, this proposed work has potential to validate that the 3D HT-HC metastasis model developed in this work provides similar outcomes to an *in-vivo* model, and therefore may be more predictive of clinical outcomes.

4.3   Future Work

In addition to the model validation described above, the model developed in this work has potential for many future applications and studies. A few of these include automation of experimental setup to enable truly high-throughput screening, mechanistic study of metastasis mechanobiology, and translational for personalized medicine. These different applications are briefly described in the following sections.

4.3.1   Automation and HT screening validation

To truly translate this HT-HC metastasis model as a drug screening platform, collaborative efforts with drug discovery groups in academia or industry would be needed to automate the experimental setup. Since the fabrication platform developed in this thesis is already user friendly and was designed to interface with standard 96-well plates, it should be straightforward to customize commercial liquid handling robots to facilitate automated model setup. One of the major hurdles of this would be temperature regulation since the oligomeric collagen would need to be kept cool (4 °C) before pipetting and then subsequently heated (37°C) to polymerize. However, once this increase in throughput of model setup is achieve it would in turn enable truly high-throughput screening in order to validate the high-content assay outcomes by testing drugs of various mechanisms of action. Specifically, drugs that are known to inhibit proliferation, metabolic activity and invasion could be tested to validate that each of the outcomes of the high-content assay can be independently modulated. Additionally, positive and negative reference compounds, (i.e. those which have gained FDA approval and those which have failed in clinical trials due to lack of efficacy, respectively) could be used to further validate the predictive power of this HT-HC metastasis model.

4.3.2 Mechanistic studies

Mechanobiology is very important in metastasis since cells experience a diverse range of physical properties as they invade through surrounding tissue, intravasate into the circulation, and disseminate to distance sites in the body [35,105]. Even though the initial metastatic events of EMT and invasion are widely studied, the mechanobiology underlying these processes is still not fully elucidated. However, it is known that ECM microstructure and topography, as well as the biophysical force balance between the cytoskeleton and the ECM are important in guiding invasion [148]. Examples of this include the creation of "highways" for cancer invasion either as microtracks in matrices *in vitro* and *in vivo* or the alignment of collagen fibers perpendicular to the tumor boundary [38,135]. To more fully understand these processes, the high level of user control offered by the HT-HC metastasis could be used to explore how changes in ECM composition and microstructure influence tumor invasion. Specifically, the collagen concentration and the ratio of collagen oligomers to monomers could be varied independently to define how fibril density and interfibril branching influence invasion [57,58]. Additionally, since the mechanobiology associated with when and why cells employ different modes of invasion is also not fully understood, this customizable model could provide the opportunity to define relationships between tumor invasion mode and ECM biophysical properties. More detailed genomic and proteomic analysis could also be performed to elucidate mechanisms underlying various invasive phenotypes within different matrix conditions. Altogether, because of the high level of user control that this model offers it has great potential to serve as a useful tool for mechanistic mechanobiology.

4.3.3 Personalized medicine

Finally, this HT-HC metastasis model also has potential for use in precision medicine— the concept of tailoring treatment strategies to fit individual patient needs. Since cancer is one of the main focuses of the National Institutes of Health Precision Medicine Initiative the National Institute of Cancer (NCI) has developed several focused programs, one of which is to develop novel laboratory models which can be used to further characterize patient tumors and provide patient-specific predictions of treatment response [149]. Since the compatibility with patient derived cells has already been validated, the HT-HC metastasis model developed in this thesis could be used to characterize the phenotype and metastatic potential of patient tumor samples, as

well as perform screening on potential therapies to further inform physicians on choosing the best treatment approach for each individual patient. Next steps in this would be to obtain patient samples either through clinical collaborations or the NCI's Patient Derived Model Repository and evaluate the metastatic potential, genotype, histopathology, and treatment response *in vitro*. These *in-vitro* results could then be compared to the known clinical history, genetic profile and histopathology report to establish correlations. Others have performed these types of comparisons and predictions using *ex-vivo* cultured tumor tissue section and machine learning algorithms, however these models did not recreate the 3D microenvironment of human tumors and metastatic potential was not assessed [150]. Therefore, the HT-HC metastasis model could fill a gap in precision medicine by providing a pathophysiologically relevant platform on which treatment response and metastatic potential could simultaneously be evaluated to compliment genotypic analysis in order to choose the best treatment strategy for cancer patients.

4.4   Conclusions

Overall this work represents the initial stages of model development for a novel 3D HT-HC metastasis model with potential for phenotypic drug screening, mechanistic study, and personalized medicine. Further, once the above described validation is complete, the 3D metastasis model developed in this thesis will have overcome several key translational hurdles and be one step closer to translation to preclinical use. Additionally, this work showcases some important considerations when developing translatable in vitro models and hopefully will serve as a catalyst for future model development. Results from this work have made it clear that ECM composition and fibril microstructure are important factors to consider when developing 3D *in-vitro* models. While this may seem like an already established conclusion with prevalence of 3D culture and mechanobiology work, the field's reliance on Matrigel- and PEG-based tumor models suggests that the importance of these factors is not fully realized by many. Additionally, this work has highlighted the potential of standardized ECM materials such as Oligomer, that are not only standardized to improve reproducibility but also accurately recreate natural fibril architecture and are customizable over a wide range of biophysical properties. Using this unique biomaterial, a novel 3D metastasis model was developed that overcame several shortcomings of other commonly used models. Key verification and validation of this model included 1) demonstrating its ability for customization and standardization, 2) its compatibility with relevant

cell populations to recreate PDAC heterogeneity and desmoplasia, 3) its capacity to support relevant invasive phenotypes, and 4) its ability to translate as a high-throughput, high-content screening tool. While much work remains to further validate this model, development and application of this 3D HT-HC metastasis model has great potential to improve the efficiency of the development of anti-cancer therapies. Ultimately, by utilizing models which more faithfully recreating human tumors such as the one developed in this thesis, the success rate of anti-cancer clinical trials will be improved, leading to more effective therapies and better patient outcomes for highly metastatic cancers like PDAC.

APPENDIX

Chapter 3 Supplemental Information

Table S 1 – Comparison of gemcitabine IC50 values for PDAC lines in 2D

IC50 (nM)			Experimental Conditions				Reference
BxPC-3	Panc-1	MiaPaCa-2	Cell Density (10^3 cells/well)	Culture Medium	Duration (hr)	Assay	
830	95	494	4	RPMI for all	72	WST-1	[151]
13.6	137	7.73	2	RPMI for BxPC-3; DMEM for Panc-1 & MiaPaCa-2	96	Cell Titer Glo	[152]
5,910	58,200	11,430	5	RPMI for all but MiaPaCa-2	72	MTT	[153]
17.9	27	51	20	DMEM for all	72	PI intensity	[154]
25,300	30,700	25,900	1-5	RPMI for BxPC-3; DMEM for Panc-1 & MiaPaCa-2	72	MTT	[155]
80	225	733	4	RPMI for all but Panc-1	48	PI intensity	[156]
12.6	28.2	1.9	4	RPMI for BxPC-3; DMEM for Panc-1 & MiaPaCa-2	72	Alamar Blue	Present study

Note: Grayed rows represent studies with experimental conditions and results most similar to the present study (also grayed)

Chapter 4 Supplemental Information
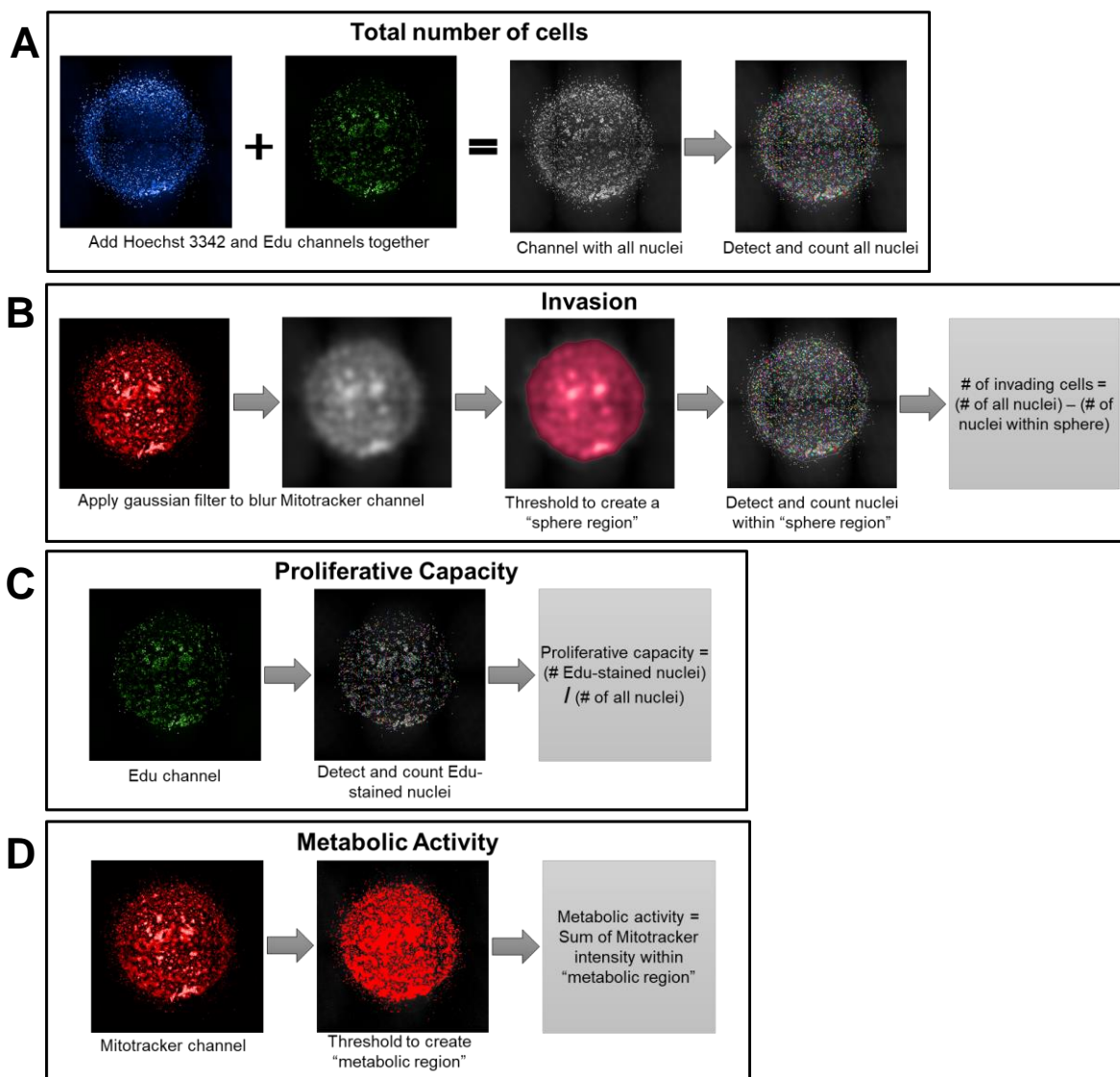
Figure S 1 Analysis in Harmony software of high-content assay
(A) The first step in the analysis was to count the total number of cells in the image. This was done by adding the two channels which represented stained nuclei together (Hoechst 33342 and Edu) and detected all of the nuclei (B) The invasion analysis involved creating a "sphere region" by blurring and thresholding the Mitotracker channel, counting the nuclei within this region, and subtracting the number of cells within the sphere from the total number of cells to quantify the number of invading cells. (B) Proliferative capacity was quantified by simply counting all of the Edu-stained nuclei and dividing by the total number of nuclei. (D) Metabolic activity was quantified by thresholding the raw Mitotracker channel to obtain a "metabolic region" and summing the intensity of the Mitotracker signal within that region.

REFERENCES

1. National Cancer Institute. Cancer Statistics [Internet]. NCI website. 2017. Available from: https://www.cancer.gov/about-cancer/understanding/statistics

2. Mariotto AB, Yabroff KR, Shao Y, Feuer EJ, Brown ML. Projections of the cost of cancer care in the United States: 2010-2020. J Natl Cancer Inst. 2011 Jan 19;103(2):117–28.

3. Adams CP, Brantner VV. Spending on New Drug Development. Health Econ. 2010;19(February 2009):130–41.

4. DiMasi J a, Reichert JM, Feldman L, Malins a. Clinical approval success rates for investigational cancer drugs. Clin Pharmacol Ther. 2013 Sep;94(3):329–35.

5. Kola I, Landis J. Can the pharmaceutical industry reduce attrition rates? Nat Rev Drug Discov. 2004 Aug;3(8):711–5.

6. Scannell JW, Blanckley A, Boldon H, Warrington B. Diagnosing the decline in pharmaceutical R&D efficiency. 2012;11(March):191–200.

7. Swinney DC, Anthony J. How were new medicines discovered? Nat Rev Drug Discov. 2011;10(7):507–19.

8. Baker A-M, Bird D, Welti JC, Gourlaouen M, Lang G, Murray GI, et al. Lysyl oxidase plays a critical role in endothelial cell stimulation to drive tumor angiogenesis. Cancer Res. 2013 Jan 15;73(2):583–94.

9. Zheng W, Thorne N, McKew JC. Phenotypic screens as a renewed approach for drug discovery. Drug Discov Today. 2013;18(21–22):1067–73.

10. Vincent F, Loria P, Pregel M, Stanton R, Nocka K, Doyonnas R, et al. Developing predictive assays : The phenotypic screening "rule of 3." Sci Transl Med. 2015;7(293):1–6.

11. Breslin S, O'Driscoll L. Three-dimensional cell culture: the missing link in drug discovery. Drug Discov Today. 2013 Mar;18(5–6):240–9.

12. Kimlin LC, Casagrande G, Virador VM. In vitro three-dimensional (3D) models in cancer research: an update. Mol Carcinog. 2013 Mar;52(3):167–82.

13. Yamada KM, Cukierman E. Modeling tissue morphogenesis and cancer in 3D. Cell. 2007 Aug 24;130(4):601–10.

14. Sharpless NE, Depinho R a. The mighty mouse: genetically engineered mouse models in cancer drug development. Nat Rev Drug Discov. 2006 Sep;5(9):741–54.

15. Ghajar CM, Bissell MJ. Tumor engineering: the other face of tissue engineering. Tissue Eng Part A. 2010;16(7):2153–6.

16. Das V, Bruzzese F, Konečný P, Iannelli F, Budillon A, Hajdúch M. Pathophysiologically relevant in vitro tumor models for drug screening. Drug Discov Today. 2015;20(7):848–55.

17. Young EWK. Cells, tissues, and organs on chips: challenges and opportunities for the cancer tumor microenvironment. Integr Biol (Camb). 2013 Sep;5(9):1096–109.

18. Kreger ST, Bell BJ, Bailey J, Stites E, Kuske J, Waisner B, et al. Polymerization and matrix physical properties as important design considerations for soluble collagen formulations. Biopolymers. 2010 Aug;93(8):690–707.

19. Benton G, Arnaoutova I, George J, Kleinman HK, Koblinski J. Matrigel: From discovery and ECM mimicry to assays and models for cancer research. Adv Drug Deliv Rev. 2014 Jul 2;79–80:3–8.

20. Vinci M, Gowan S, Boxall F, Patterson L, Zimmermann M, Court W, et al. Advances in establishment and analysis of three-dimensional tumor spheroid-based functional assays for target validation and drug evaluation. BMC Biol. 2012 Jan;10(1):29.

21. Zanoni M, Piccinini F, Arienti C, Zamagni A, Santi S, Polico R, et al. 3D tumor spheroid models for in vitro therapeutic screening: a systematic approach to enhance the biological relevance of data obtained. Sci Rep. 2016;6(August 2015):19103.

22. Santo VE, Rebelo SP, Estrada MF, Alves PM, Boghaert E, Brito C. Drug screening in 3D in vitro tumor models : overcoming current pitfalls of efficacy read-outs. Biotechnol J. 2017;12:1–18.

23. Cox MC, Reese LM, Bickford LR, Verbridge SS. Toward the Broad Adoption of 3D Tumor Models in the Cancer Drug Pipeline. ACS Biomater Sci Eng. 2015;1(10):877–94.

24. Astashkina A, Grainger DW. Critical analysis of 3-D organoid in vitro cell culture models for high-throughput drug candidate toxicity assessments. Adv Drug Deliv Rev. 2014;69–70:1–18.

25. Fidler IJ, Kripke ML. The challenge of targeting metastasis. Cancer Metastasis Rev. 2015;34(4):635–41.

26.   Quail DF, Joyce JA. Microenvironmental regulation of tumor progression and metastasis. Nat Med. 2013;19(11):1423–37.

27.   Xie D, Xie K. Pancreatic cancer stromal biology and therapy. Genes Dis. 2015;2(2):133–43.

28.   Oettle H. Progress in the knowledge and treatment of advanced pancreatic cancer: From benchside to bedside. Cancer Treat Rev. 2014;40(9):1039–47.

29.   Decaestecker C, Debeir O, Van Ham P, Kiss R. Can anti-migratory drugs be screened in vitro? A review of 2D and 3D assays for the quantitative analysis of cell migration. Med Res Rev. 2007 Mar;27(2):149–76.

30.   National Cancer Institute. Cancer Stat Facts: Pancreas Cancer [Internet]. NCI website. 2017. Available from: https://seer.cancer.gov/statfacts/html/pancreas.html

31.   National Cancer Institute. Scientific Framework for Pancreatic Ductal Adenocarcinoma (PDAC). 2014.

32.   Shields MA, Dangi-Garimella S, Redig AJ, Munshi HG. Biochemical role of the collagen-rich tumour microenvironment in pancreatic cancer progression. Biochem J. 2012 Jan 15;441(2):541–52.

33.   Armstrong T, Packham G, Murphy LB, Bateman AC, Conti JA, Fine DR, et al. Type I Collagen Promotes the Malignant Phenotype of Pancreatic Ductal Adenocarcinoma. Clin Cancer Res. 2004;10:7427–37.

34.   Tod J, Jenei V, Thomas G, Fine D. Tumor-stromal interactions in pancreatic cancer. Pancreatology. 2012;13(1):1–7.

35.   Spill F, Reynolds DS, Kamm RD, Zaman MH. Impact of the physical microenvironment on tumor progression and metastasis. Curr Opin Biotechnol. 2016;40:41–8.

36.   Martinez NJ, Titus SA, Wagner AK, Simeonov A. High throughput fluoresecent imaging approaches for drug discovery using in vitro and in vivo three-dimensional models. Expert Opin Drug Discov. 2015;10(12):1347–61.

37.   National Cancer Institute. Scientific Framework for Pancreatic Ductal Adenocarcinoma (PDAC). 2014.

38.   Malik R, Lelkes PI, Cukierman E. Biomechanical and biochemical remodeling of stromal extracellular matrix in cancer. Trends Biotechnol. 2015;33(4):230–6.

39. Pickup MW, Mouw JK, Weaver VM. The extracellular matrix modulates the hallmarks of cancer. EMBO Rep. 2014;15(12):1243–53.

40. Gore J, Korc M. Pancreatic cancer stroma: friend or foe? Cancer Cell. 2014 Jun 16;25(6):711–2.

41. Whatcott CJ, Posner RG, Von Hoff DD, Han H. Desmoplasia and chemoresistance in pancreatic cancer. In: Grippo PJ, Munshi HG, editors. Pancreatic Cancer and Tumor Microenvironment. India: Transworld Research Network; 2012.

42. Erler JT, Weaver VM. Three-dimensional context regulation of metastasis. Clin Exp Metastasis. 2009;26(1):35–49.

43. Zeisberg M, Neilson EG. Biomarkers for epithelial-mesenchymal transitions. J Clin Invest. 2009;119(6):1429–37.

44. Kalluri R, Weinberg RA. The basics of epithelial-mesenchymal transition. J Clin Invest. 2009;119(6):1420–8.

45. Klemm F, Joyce JA. Microenvironmental regulation of therapeutic response in cancer. Trends Cell Biol. 2015;25(4):198–213.

46. Acloque H, Adams MS, Fishwick K, Bronner-Fraser M, Nieto MA. Epithelial-mesenchymal transitions: The importance of changing cell state in development and disease. J Clin Invest. 2009;119(6):1438–49.

47. O'Connor JW, Gomez EW. Biomechanics of TGFβ-induced epithelial-mesenchymal transition: implications for fibrosis and cancer. Clin Transl Med. 2014;3(23).

48. Wei SC, Fattet L, Yang J. The forces behind EMT and tumor metastasis. Cell Cycle. 2015;14(15):2387–8.

49. Craene B De, Berx G. Regulatory networks defining EMT during cancer initiation and progression. Nat Rev Cancer. 2013;13(2):97–110.

50. Lamouille S, Xu J, Derynck R. Molecular mechanisms of epithelial-mesenchymal transition. Nat Rev Mol Cell Biol. 2014 Mar;15(3):178–96.

51. Wei SC, Fattet L, Tsai JH, Guo Y, Pai VH, Majeski HE, et al. Matrix stiffness drives epithelial–mesenchymal transition and tumour metastasis through a TWIST1–G3BP2 mechanotransduction pathway. Nat Cell Biol. 2015;17(5):678–688.

52. Paszek MJ, Zahir N, Johnson KR, Lakins JN, Rozenberg GI, Gefen A, et al. Tensional homeostasis and the malignant phenotype. Cancer Cell. 2005 Sep;8(3):241–54.

53. Guzman A, Ziperstein MJ, Kaufman LJ. The effect of fibrillar matrix architecture on tumor cell invasion of physically challenging environments. Biomaterials. 2014;35(25):6954–63.

54. Lam RCI, Wong HK, Nai S, Chua CK, Tan NS, Tan LP. A 3D Biomimetic Model of Tissue Sti ff ness Interface for Cancer Drug Testing. Mol Pharm. 2014;11:2016–21.

55. Herrera-Perez M, Voytik-Harbin S, Rickus JL. Extracellular matrix properties regulate the migratory response of glioblastoma stem cells in 3D culture. Tissue Eng Part A. 2015;21:2572–82.

56. Blum KM, Novak T, Watkins L, Neu CP, Wallace JM, Bart ZR, et al. Acellular and cellular high-density, collagen-fibril constructs with suprafibrillar organization. Biomater Sci. 2016;4(4):711–23.

57. Bailey JL, Critser PJ, Whittington C, Kuske JL, Yoder MC, Voytik-Harbin SL. Collagen oligomers modulate physical and biological properties of three-dimensional self-assembled matrices. Biopolymers. 2011 Feb;95(2):77–93.

58. Whittington CF, Yoder MC, Voytik-Harbin SL. Collagen-polymer guidance of vessel network formation and stabilization by endothelial colony forming cells in vitro. Macromol Biosci. 2013 Jul 5;1–15.

59. Monteleon CL, Sedgwick A, Hartsell A, Dai M, Whittington C, Voytik-Harbin S, et al. Establishing epithelial glandular polarity: interlinked roles for ARF6, Rac1, and the matrix microenvironment. Mol Biol Cell. 2012 Dec;23(23):4495–505.

60. Johnson KR, Leight JL, Weaver VM. Demystifying the Effects of a Three-Dimensional Microenvironment in Tissue Morphogenesis. Methods Cell Biol. 2007;83:547–83.

61. Teixidó C, Marés R, Aracil M, Ramón y Cajal S, Hernández-Losa J. Epithelial-mesenchymal transition markers and HER3 expression are predictors of elisidepsin treatment response in breast and pancreatic cancer cell lines. PLoS One. 2013 Jan;8(1):e53645.

62. Arumugam T, Ramachandran V, Fournier KF, Wang H, Marquis L, Abbruzzese JL, et al. Epithelial to mesenchymal transition contributes to drug resistance in pancreatic cancer. Cancer Res. 2009 Jul 15;69(14):5820–8.

63. Menke A, Philippi C, Vogelmann R, Seidel B, Lutz MP, Adler G, et al. Down-Regulation of E-Cadherin Gene Expression by Collagen Type I and Type III in Pancreatic Cancer Cell Lines 1. Cancer Res. 2001;61:3508–17.

64. Medici D, Nawshad A. Type I collagen promotes epithelial-mesenchymal transition through ILK-dependent activation of NF-kappaB and LEF-1. Matrix Biol. 2009;29(3):161–5.

65. Walsh LA, Nawshad A, Medici D. Discoidin domain receptor 2 is a critical regulator of epithelial-mesenchymal transition. Matrix Biol. 2011;30(4):243–7.

66. Koenig A, Mueller C, Hasel C, Adler G, Menke A. Collagen type I induces disruption of E-cadherin-mediated cell-cell contacts and promotes proliferation of pancreatic carcinoma cells. Cancer Res. 2006;66(9):4662–71.

67. Sapudom J, Rubner S, Martin S, Kurth T, Riedel S, Mierke CT, et al. The phenotype of cancer cell invasion controlled by fibril diameter and pore size of 3D collagen networks. Biomaterials. 2015;52:367–75.

68. Taubenberger A V., Bray LJ, Haller B, Shaposhnykov A, Binner M, Freudenberg U, et al. 3D extracellular matrix interactions modulate tumour cell growth, invasion and angiogenesis in engineered tumour microenvironments. Acta Biomater. 2016;36:73–85.

69. Lee DW, Choi Y, Seo YJ, Lee M, Jeon SY, Ku B. High-Throughput Screening (HTS) of Anticancer Drug Efficacy on a Micropillar/Microwell Chip Platform. Anal Chem. 2014;86:535–42.

70. Seguin L, Desgrosellier JS, Weis SM, Cheresh DA. Integrins and cancer: regulators of cancer stemness, metastasis, and drug resistance. Trends Cell Biol. 2015;25(4):234–40.

71. Multhaupt HAB, Leitinger B, Gullberg D, Couchman JR. Extracellular matrix component signaling in cancer. Adv Drug Deliv Rev. 2016;97:28–40.

72. Feig C, Gopinathan A, Neesse A, Chan DS, Cook N, Tuveson DA. The pancreas cancer microenvironment. Clin Cancer Res. 2012;18(16):4266–76.

73. Tang D, Wang D, Yuan Z, Xue X, Zhang Y, An Y, et al. Persistent activation of pancreatic stellate cells creates a microenvironment favorable for the malignant behavior of pancreatic ductal adenocarcinoma. Int J Cancer. 2013;132(5):993–1003.

74. Whittington C, Brandner E. Oligomers Modulate Interfibril Branching and Mass Transport Properties of Collagen Matrices. Microsc …. 2013;19(5):1323–33.

75. Hamed SS, Straubinger RM, Jusko WJ. Pharmacodynamic modeling of cell cycle and apoptotic effects of gemcitabine on pancreatic adenocarcinoma cells. Cancer Chemother Pharmacol. 2013;72(3):553–63.

76. Whatcott CJ, Diep CH, Jiang P, Watanabe A, Lobello J, Sima C, et al. Desmoplasia in primary tumors and metastatic lesions of pancreatic cancer. Clin Cancer Res. 2015;21(15):3561–8.

77. Han B, Qu C, Park K, Konieczny SF, Korc M. Recapitulation of complex transport and action of drugs at the tumor microenvironment using tumor-microenvironment-on-chip. Cancer Lett. 2016;380:319–29.

78. Rhim AD, Oberstein PE, Thomas DH, Mirek ET, Palermo CF, Sastra SA, et al. Stromal Elements Act to Restrain, Rather Than Support, Pancreatic Ductal Adenocarcinoma. Cancer Cell. 2014;25(6):735–47.

79. Ozdemir BC, Pentcheva-Hoang T, Carstens JL, Zheng X, Wu CC, Simpson TR, et al. Depletion of carcinoma-associated fibroblasts and fibrosis induces immunosuppression and accelerates pancreas cancer with reduced survival. Cancer Cell. 2014;25(6):719–34.

80. Rowe RG, Weiss SJ. Breaching the basement membrane: who, when and how? Trends Cell Biol. 2008;18(11):560–74.

81. Rowe RG, Weiss SJ. Navigating ECM barriers at the invasive front: the cancer cell-stroma interface. Annu Rev Cell Dev Biol. 2009;25:567–95.

82. Birk DE, Bruckner P. Collagens, Suprastructures, and Collagen Fibril Assembly. In: Mecham RP, editor. The Extracellular Matrix: an Overview. Berlin, Heidelberg: Springer-Verlag; 2011. p. 77–115.

83. Eyre DR, Wu J-J. Collagen Cross-Links. Brinckman J, Notbohm H, Muller PK, editors. Top Curr Chem. 2005;247:207–29.

84. Van Der Zee JA, Van Eijck CH, Hop WC, Biermann K, Dicheva BM, Seynhaeve AL, et al. Tumour basement membrane laminin expression predicts outcome following curative resection of pancreatic head cancer. Br J Cancer. 2012;107(7):1153–8.

85. Benton G, Kleinman HK, George J, Arnaoutova I. Multiple uses of basement membrane-like matrix (BME/Matrigel) in vitro and in vivo with cancer cells. Int J Cancer. 2011;128(8):1751–7.

86. Brookes S, Voytik-harbin S, Zhang H, Halum S. 3-Dimensional (3D) Tissue-Engineered Skeletal Muscle for Laryngeal Reconstruction. Laryngoscope. 2017;

87. Cukierman E, Pankov R, Yamada KM. Cell interactions with three-dimensional matrices. Curr Opin Cell Biol. 2002;14(5):633–9.

88. Mandal M, Ghosh B, Anura A, Mitra P, Pathak T, Chatterjee J. Modeling continuum of epithelial mesenchymal transition plasticity. Integr Biol. 2016;8:167–76.

89. Benton G, Crooke E, George J. Laminin-1 induces E-cadherin expression in 3-dimensional cultured breast cancer cells by inhibiting DNA methyltransferase 1 and reversing promoter methylation status. FASEB J. 2009;23(11):3884–95.

90. Nguyen-Ngoc K-V, Cheung KJ, Brenot A, Shamir ER, Gray RS, Hines WC, et al. ECM microenvironment regulates collective migration and local dissemination in normal and malignant mammary epithelium. Proc Natl Acad Sci. 2012;109(39):E2595–604.

91. Carey SP, Martin KE, Reinhart-king CA. Three-dimensional collagen matrix induces a mechanosensitive invasive epithelial phenotype. Sci Rep. 2017;7(42088).

92. Ki CS, Lin T-Y, Korc M, Lin C-C. Thiol-ene hydrogels as desmoplasia-mimetic matrices for modeling pancreatic cancer cell growth, invasion, and drug resistance. Biomaterials. 2014 Dec;35(36):9668–77.

93. Bidarra SJ, Oliveira P, Rocha S, Saraiva DP, Oliveira C, Barrias CC. A 3D in vitro model to explore the inter-conversion between epithelial and mesenchymal states during EMT and its reversion. Sci Rep. 2016;6(February):27072.

94. Markowski MC, Brown AC, Barker TH. Directing epithelial to mesenchymal transition through engineered microenvironments displaying orthogonal adhesive and mechanical cues. J Biomed Mater Res - Part A. 2012;100 A(8):2119–27.

95. Cassereau L, Miroshnikova YA, Ou G, Lakins J, Weaver VM. A 3D tension bioreactor platform to study the interplay between ECM stiffness and tumor phenotype. J Biotechnol. 2015;193:66–9.

96. Benton G, DeGray G, Kleinman HK, George J, Arnaoutova I. In Vitro Microtumors Provide a Physiologically Predictive Tool for Breast Cancer Therapeutic Screening. PLoS One. 2015;10:e0123312.

97. Klymkowsky MW, Savagner P. Epithelial-Mesenchymal Transition: A Cancer Researcher's Conceptual Friend and Foe. Am J Pathol. 2009;174(5):1588–93.

98.   Tilghman RW, Cowan CR, Mih JD, Koryakina Y, Gioeli D, Slack-Davis JK, et al. Matrix rigidity regulates cancer cell growth and cellular phenotype. PLoS One. 2010;5(9):1–13.

99.   Harunaga JS, Yamada KM. Cell-matrix adhesions in 3D. Matrix Biol. 2011;30(7–8):363–8.

100. Pathak A, Kumar S. Biophysical regulation of tumor cell invasion: moving beyond matrix stiffness. Integr Biol. 2011;3:267–78.

101. Levental KR, Yu H, Kass L, Lakins JN, Egeblad M, Erler JT, et al. Matrix crosslinking forces tumor progression by enhancing integrin signaling. Cell. 2009 Nov 25;139(5):891–906.

102. Egeblad M, Rasch MG, Weaver VM. Dynamic interplay between the collagen scaffold and tumor evolution. Curr Opin Cell Biol. 2010;22(5):697–706.

103. ASTM International. ASTM Standard F3089: Standard Guide for Characterization and Standardization of Polymerizable Collagen-based Products and Associated Collagen-cell Interactions. West Conshohocken, PA; 2014.

104. Creighton CJ, Gibbons DL, Kurie JM. The role of epithelial-mesenchymal transition programming in invasion and metastasis: A clinical perspective. Cancer Manag Res. 2013;5(1):187–95.

105. Makale M. Cellular mechanobiology and cancer metastasis. Birth Defects Res Part C. 2007;81(4):329–43.

106. Wang C, Tang Z, Zhao Y, Yao R, Li L. Three-dimensional in vitro cancer models : a short review. Biofabrication. 2014;6.

107. Zanella F, Lorens JB, Link W. High content screening: Seeing is believing. Trends Biotechnol. 2010;28(5):237–45.

108. Kramer N, Walzl A, Unger C, Rosner M, Krupitza G, Hengstschla M. In vitro cell migration and invasion assays. Mutaion Res. 2013;752:10–24.

109. Katt ME, Placone AL, Wong AD, Xu ZS, Searson PC. In Vitro Tumor Models: Advantages, Disadvantages, Variables, and Selecting the Right Platform. Front Bioeng Biotechnol. 2016;4(February):12.

110. Nath S, Devi GR. Three-dimensional culture systems in cancer research : Focus on tumor spheroid model. Pharmacol Ther. 2016;163:94–108.

111. Veelken C, Bakker G, Drell D, Friedl P. Single cell-based automated quantification of therapy responses of invasive cancer spheroids in organotypic 3D culture. Methods. 2017;128:139–49.

112. Willis AL, Sabeh F, Li XY, Weiss SJ. Extracellular matrix determinants and the regulation of cancer cell invasion stratagems. J Microsc. 2013;251(3):250–60.

113. Sodek KL, Brown TJ, Ringuette MJ. Collagen I but not Matrigel matrices provide an MMP-dependent barrier to ovarian cancer cell penetration. BMC Cancer. 2008;8(1):223.

114. Buno KP, Chen X, Weibel JA, Thiede SN, Garimella S V, Yoder MC, et al. In Vitro Multitissue Interface Model Supports Rapid Vasculogenesis and Mechanistic Study of Vascularization across Tissue Compartments. Appl Mater Interfaces. 2016;In Press.

115. Peela N, Truong D, Saini H, Chu H, Mashaghi S, Ham SL, et al. Advanced Biomaterials and Microengineering Technologies to Recapitulate the Stepwise Process of Cancer Metastasis. Biomaterials. 2017;133.

116. Puls TJ, Tan X, Whittington CF, Voytik-Harbin SL. 3D Collagen Fibrillar Microstructure Guides Pancreatic Cancer Cell Phenotype and Serves as a Critical Design Parameter for Phenotypic Models of EMT. PloS O2ne. 2017;In Press.

117. Friedl P, Alexander S. Cancer invasion and the microenvironment: plasticity and reciprocity. Cell. 2011 Nov 23;147(5):992–1009.

118. Friedl P, Wolf K. Tumour-cell invasion and migration: diversity and escape mechanisms. Nat Rev Cancer. 2003;3(5):362–74.

119. Alexander S, Weigelin B, Winkler F, Friedl P. Preclinical intravital microscopy of the tumour-stroma interface: Invasion, metastasis, and therapy response. Curr Opin Cell Biol. 2013;25(5):659–71.

120. Bronsert P, Enderle-Ammour K, Bader M, Timme S, Kuehs M, Csanadi A, et al. Cancer cell invasion and EMT marker expression: a three-dimensional study of the human cancer-host interface. J Pathol. 2014;234(3):410–22.

121. Clark AG, Vignjevic DM. Modes of cancer cell invasion and the role of the microenvironment. Curr Opin Cell Biol. 2015;36:13–22.

122. Deer EL, Gonzalez-Hernandez J, Coursen JD, Shea JE, Ngatia J, Scaife CL, et al. Phenotype and Genotype of Pancreatic Cancer Cell Lines. Pancreas. 2010;39(4):425–35.

123. Haage A, Schneider IC. Cellular contractility and extracellular matrix stiffness regulate matrix metalloproteinase activity in pancreatic cancer cells. FASEB J. 2014;28(8):3589–99.

124. Daudigeos-Dubus E, LE Dret L, Rouffiac V, Bawa O, Leguerney I, Opolon P, et al. Establishment and Characterization of New Orthotopic and Metastatic Neuroblastoma Models. In Vivo. 2014;28(4):425–34.

125. Beerling E, Oosterom I, Voest E, Lolkema M, Rheenen J Van. Intravital characterization of tumor cell migration in pancreatic cancer. IntraVital. 2016;5(3):1–8.

126. Whatcott CJ, Han H, Posner RG, Von Hoff DD. Tumor-stromal interactions in pancreatic cancer. Crit Rev Oncog. 2013;18:135–51.

127. von Ahrens D, Bhagat TD, Nagrath D, Maitra A, Verma A. The role of stromal cancer-associated fibroblasts in pancreatic cancer. J Hematol Oncol. 2017;10(1):76.

128. Logsdon DP, Grimard M, Luo M, Shahda S, Jiang Y, Tong Y, et al. Regulation of HIF1α under Hypoxia by APE1/Ref-1 Impacts CA9 Expression: Dual-Targeting in Patient-Derived 3D Pancreatic Cancer Models.

129. Perret GY, Crepin M. New pharmacological strategies against metastatic spread. Fundam Clin Pharmacol. 2008;22:465–92.

130. Pradhan S, Clary JM, Seliktar D, Lipke EA. A three-dimensional spheroidal cancer model based on PEG-fibrinogen hydrogel microspheres. Biomaterials. 2017;115:141–54.

131. Jang M, Koh I, Lee SJ, Cheong J-H, Kim P. Droplet-based microtumor model to assess cell-ECM interactions and drug resistance of gastric cancer cells. Sci Rep. 2017;7(December 2016):41541.

132. Ware MJ, Colbert K, Keshishian V, Ho JC-S, Corr SJ, Curley S, et al. Generation of homogenous 3D pancreatic cancer cell spheroids using an improved hanging drop technique. Tissue Eng Part C Methods. 2016;(August):1–36.

133. Ma J, Zhang X, Liu Y, Yu H, Liu L, Shi Y, et al. Patterning hypoxic multicellular spheroids in a 3D matrix - a promising method for anti-tumor drug screening. Biotechnol J. 2016;11(1):127–34.

134. Evensen NA, Li J, Yang J, Yu X, Sampson NS, Zucker S, et al. Development of a high-throughput three-dimensional invasion assay for anti-cancer drug discovery. PLoS One. 2013;8(12):1–11.

135. Carey SP, Rahman A, Kraning-Rush CM, Romero B, Somasegar S, Torre OM, et al. Comparative mechanisms of cancer cell migration through 3D matrix and physiological microtracks. AJP Cell Physiol. 2014;308(6):C436-47.

136. Bordeleau F, Tang LN, Reinhart-King CA. Topographical guidance of 3D tumor cell migration at an interface of collagen densities. Phys Biol. 2013;10(6):65004.

137. Suetsugu A, Snyder CS, Moriwaki H, Saji S, Bouvet M, Hoffman RM. Imaging the interaction of pancreatic cancer and stellate cells in the tumor microenvironment during metastasis. Anticancer Res. 2015;35(5):2545–52.

138. Labernadie A, Kato T, Brugués A, Serra-Picamal X, Derzsi S, Arwert E, et al. A mechanically active heterotypic E-cadherin/N-cadherin adhesion enables fibroblasts to drive cancer cell invasion. Nat Cell Biol. 2017;19(3):224–37.

139. Hao R, Wei Y, Li C, Chen F, Chen D, Zhao X, et al. A Microfabricated 96-Well 3D Assay Enabling High-Throughput Quantification of Cellular Invasion Capabilities. Sci Rep. 2017;7(November 2016):43390.

140. Carey SP, D'Alfonso TM, Shin SJ, Reinhart-King CA. Mechanobiology of tumor invasion: Engineering meets oncology. Crit Rev Oncol Hematol. 2012;83(2):170–83.

141. Shah F, Logsdon D, Messmann RA, Fehrenbacher JC, Fishel ML, Kelley MR. Exploiting the Ref-1-APE1 node in cancer signaling and other diseases : from bench to clinic. npj Precis Oncol. 2017;(March):1–18.

142. Lattouf R, Younes R, Lutomski D, Naaman N, Godeau G, Senni K, et al. Picrosirius Red Staining : A Useful Tool to Appraise Collagen Networks in Normal and Pathological Tissues. J Histochem Cytochem. 2014;62(10):751–8.

143. Nielsen MFB, Mortensen MB, Detlefsen S. Key players in pancreatic cancer-stroma interaction: Cancer-associated fibroblasts, endothelial and inflammatory cells. World J Gastroenterol. 2016;22(9):2678–700.

144. Scholzen T, Gerdes J. The Ki-67 Protein : From the Known and the Unknown. J Cell Physiol. 2000;182:311–22.

145. Ammendola M, Sacco R, Marech I, Sammarco G, Zuccalà V, Luposella M, et al. Microvascular density and endothelial area correlate with Ki-67 proliferative index in surgically-treated pancreatic ductal adenocarcinoma patients. Oncol Lett. 2015;10:967–71.

146. Brabletz T. To differentiate or not — routes towards metastasis. Nat Rev Cancer. 2012;12(6):425–36.

147. Schober M, Jesenofsky R, Faissner R, Weidenauer C, Hagmann W, Michl P, et al. Desmoplasia and chemoresistance in pancreatic cancer. Cancers (Basel). 2014;6(4):2137–54.

148. Bordeleau F, Alcoser T a., Reinhart-King C a. Physical biology in cancer. 5. The rocky road of metastasis: the role of cytoskeletal mechanics in cell migratory response to 3D matrix topography. Am J Physiol Cell Physiol. 2014;306(2):C110-20.

149. National Cancer Institute. NCI and the Precision Medicine Initiative [Internet]. cancer.gov. 2016. Available from: http://www.cancer.gov/research/key-initiatives/precision-medicine

150. Majumder B, Baraneedharan U, Thiyagarajan S, Radhakrishnan P, Narasimhan H, Dhandapani M, et al. Predicting clinical response to anticancer drugs using an ex vivo platform that captures tumour heterogeneity. Nat Commun. 2015;6:6169.

151. Awasthi N, Zhang C, Schwarz AM, Hinz S, Wang C, Williams NS, et al. Comparative benefits of nab-paclitaxel over gemcitabine or polysorbate-based docetaxel in experimental pancreatic cancer. Carcinogenesis. 2013;34(10):2361–9.

152. Hu G, Li F, Ouyang K, Xie F, Tang X, Wang K, et al. Intrinsic gemcitabine resistance in a novel pancreatic cancer cell line is associated with cancer stem cell-like phenotype. Int J Oncol. 2012;40(3):798–806.

153. Huanwen W, Zhiyong L, Xiaohua S, Xinyu R, Kai W, Tonghua L. Intrinsic chemoresistance to gemcitabine is associated with constitutive and laminin-induced phosphorylation of FAK in pancreatic cancer cell lines. Mol Cancer. 2009;8(125).

154. Kurata N, Fujita H, Ohuchida K, Mizumoto K, Mahawithitwong P, Sakai H, et al. Predicting the chemosensitivity of pancreatic cancer cells by quantifying the expression levels of genes associated with the metabolism of gemcitabine and 5-fluorouracil. Int J Oncol. 2011;39(2):473–82.

155. Mori-Iwamoto S, Kuramitsu Y, Ryozawa S, Taba K, Fujimoto M, Okita K, et al. A proteomic profiling of gemcitabine resistance in pancreatic cancer cell lines. Mol Med Rep. 2008;1(3):429–34.

156. Rathos MJ, Joshi K, Khanwalkar H, Manohar SM, Joshi KS. Molecular evidence for increased antitumor activity of gemcitabine in combination with a cyclin-dependent kinase inhibitor, P276-00 in pancreatic cancers. J Transl Med. 2012;10(1):161.

PUBLICATIONS

1. Puls, T., Tan, X., Whittington, C.F., and Voytik-Harbin, S.L. 3D collagen fibrillar microstructure guides pancreatic cancer cell phenotype and serves as critical design parameter for phenotypic models of EMT. PLOS ONE *In Press*

2. Puls, T., Tan, X., Husain, M. Whittington, C.F., Fishel, M.L., and Voytik-Harbin, S.L Development of a Novel High-throughput, High-content phenotypic screening model for Metastasis. *In preparation*

3. Puls, T., Whittington, C.F., Buno, K., and Voytik-Harbin, S.L. "High-throughput Phenotypic Screening Models of Tumor Metastasis," U.S. Provisional Patent Application No. 62455247, filed February 6, 2017.